Title
Ion Temperature Measurements of Two Flux Ropes in a Laboratory Plasma Experiment

Author
Tang, Shawn Wenjie

Publication Date
2022

Peer reviewed|Thesis/dissertation

UNIVERSITY OF CALIFORNIA

Los Angeles

Ion Temperature Measurements of Two Flux Ropes in a Laboratory Plasma Experiment

A dissertation submitted in partial satisfaction

of the requirements for the degree of

Doctor of Philosophy in Physics

by

Shawn Wenjie Tang

2022

ABSTRACT OF THE DISSERTATION

Ion Temperature Measurements of Two Flux Ropes in a Laboratory Plasma Experiment

by

Shawn Wenjie Tang

Doctor of Philosophy in Physics

University of California, Los Angeles, 2022

Professor Walter N. Gekelman, Chair

The energization of ions in a dynamic system containing two colliding magnetic flux ropes is investigated in an experimental study presented in this dissertation. Two kink-unstable flux ropes on the Large Plasma Device (LAPD) are made to collide in order to trigger magnetic reconnection, a process in which magnetic energy stored in the fields is dissipated into thermal and kinetic energy that is picked up by surrounding ions. The local energy distribution of the ions is measured by a four-grid ion retarding field energy analyzer that was constructed specifically for this study. The average energy $\langle 2E \rangle$, a quantity equivalent to the Maxwellian temperature for non-Maxwellian distribution functions, was plotted as a function of time for two different flux rope conditions. In both cases, $\langle 2E \rangle$ spikes indicated the presence of an ion beam with a sub-Alfvénic drift velocity of 9 to 15 eV. The beam does not appear to be heated and the ion temperature of the ropes is

estimated to be between 4 to 6 eV. This is found to be consistent with a spectrometer's line-of-sight, volume-averaged measurement involving Doppler broadening of the 320.3 nm He II spectral line. Using polar plots as a visualization tool for the two-dimensional ion distribution function, the beam appears to travel primarily in the $+z$ direction along the magnetic field and out of the reconnection plane. The presence of the beam is also correlated with magnetic reconnection events that were identified by plotting line contour planes of the magnetic vector potential A_z. This means that the ions are likely to be accelerated by $-dA_z/dt$, the inductive electric fields created during magnetic reconnection. Furthermore, the energy density produced by the induced electric fields (0.5 J/m^3) is comparable to the energy per unit volume required to heat the ions from 6 to 10 eV (0.3 J/m^3) after accounting for a less than 50% efficiency of energy transferred to the ions. Overall, the evidence presented in this study strongly suggests that the ions in the beam are produced by magnetic reconnection. To the author's knowledge, this is the first experimental observation of a field-aligned ion beam generated in a reconnection experiment.

The dissertation of Shawn Wenjie Tang is approved.

Troy A. Carter

George J. Morales

Christoph Niemann

Walter N. Gekelman, Committee Chair

University of California, Los Angeles

2022

This work is dedicated to my family, especially my parents.

Contents

List of Figures

List of Tables

ACKNOWLEDGMENTS

First and foremost, I thank my advisor Professor Walter Gekelman for the invaluable guidance and support he had provided throughout my entire graduate career. Walter motivated various reasons for pursuing a Ph.D. in plasma physics at UCLA when I attended a guided tour of the LAPD as an undergrad exchange student in 2013. Since then, applying to UCLA and then working on experimental plasma physics has been a decision which I have never regretted. I would not have expected to work so closely with Walter on a regular basis or to be given the opportunity to run LAPD experiments on my own with minimal supervision. I am grateful for the numerous opportunities he has given me to develop professionally, as well as his direction on becoming a better physicist and advice on general things in life.

Secondly, I'd like to thank Professor Troy Carter, Professor George Morales and Professor Christoph Niemann for dedicating their time and expertise in reviewing this dissertation and for serving as members of my doctoral committee. In particular, I appreciate Professor Morales for his thorough inspection of the work.

In addition, I would like to acknowledge Professor Richard Sydora from the University of Alberta with whom I have collaborated, and for insightful discussions on spiky electric potential structures which was originally the proposed topic of my dissertation.

Overall, the work presented in this dissertation would not have been possible without the funding of the United States Department of Energy and the National Science Foundation, as well as the support and assistance of the scientists and staff at the Basic Plasma Science Facility. On conducting research on the LAPD, I would like to thank Dr. Patrick Pribyl for his valuable expertise on electrical engineering, especially in designing circuits and operating specific electronics which I frequently consulted about; Dr. Stephen Vincena for maintaining the backend systems of the LAPD and showing me how to operate the data acquisition system; Dr. Shreekrishna Tripathi for

discussions on flux ropes and the ion energy analyzer while inspiring a meticulous approach to conducting research and analyzing data; as well as Dr. Bart Van Compernolle and Dr. Byonghoon Seo for general discussions about research and the LAPD.

For supporting the work done at the LAPD, I would like to thank Dr. Zoltan Lucky for his expertise and resourcefulness in solving many of the logistic issues that I had; Marvin Drandell and Tai Ly for teaching me how to use various machine shop tools and machining the more complicated parts needed for probes and support structures; Avdit Kohli for constructing, diagnosing and repairing B-dot probes and various electronics; and Meg Murphy for handling much of the administrative work such as product orders and reimbursements. A special mention to the P&A IT Support Team for keeping the `ethanol` and `midas` servers well-maintained and professionally responding to all my queries whenever I needed troubleshooting assistance.

Next, I want to thank my peers, fellow graduate students and the undergrads in the 180E Lab whom I had the pleasure of working with and engaging in various intellectual discussions. Timothy DeHaas was a mentor of sorts and taught me a great deal about flux ropes, the LAPD and life in graduate school. I enjoy having casual conversations with him as much as intellectual ones, and do thank him for being patient with me when I first started out while he was writing his dissertation. His work on flux ropes has left a legacy that I am proud to inherit as something I find myself constantly looking up to and looking up.

In addition, I would also like to thank Jeffery Bonde and Michael Martin for their help when I first joined the BaPSF research group; Peter Heuer for his advice and assistance in the 180E Lab when I was preparing for my ATC; Jia Han for various discussions and helping out with the 180E Lab when I was running an experiment on the LAPD; Yuchen Qian for helping with the coding and debugging of the spectrometer data acquisition system; Suying Jin for building the Mach probe I used in one of the experiments; as well as Gurleen Bal for the occasional meet-up and giving me numerous opportunities to hone my teaching and communication skills. A special shoutout to Paokuan (Paul) Chin for his support and encouragement as a really great friend and

with Kevin Chen and Kevin Hayakawa for frequent game nights and light-hearted conversations about physics, life and graduate school. Perhaps one day they would be interested in doing some plasma physics too.

To my family back in Singapore who have been incredibly supportive and encouraging of my journey as a graduate student, I dedicate this work to them. I am forever indebted to my parents for their love and enormous sacrifices over the years, and for their concern of my well-being while studying at a place far away from home. My grandparents, especially my late grandfather, would be and would have been proud of this milestone that I have accomplished. My younger brother Darryl, whose rationality has helped me through a challenging phase in life, continues to be my source of encouragement. May my family continue to be safe, well and happy.

Additionally, I would like to acknowledge my little friends Zugu and Woomy for being a great source of comfort and for their companionship here in Los Angeles, especially during the pandemic.

Finally, I would like to extend my gratitude to the late Professor Maha Ashour-Abdalla for her kindness and the inspiration to pursue plasma physics in graduate school. My first formal exposure to plasma physics was an introductory undergraduate course taught by her, and it was during one of the classes where she arranged for a lab tour of the LAPD that I met Walter and began my journey as a graduate student at UCLA.

VITA

2013 – 2015	Undergraduate Student Researcher Center for Superconducting and Magnetic Materials National University of Singapore
2015	B.Sc. (Hons) Physics National University of Singapore
2015 – 2019	Graduate Teaching Assistant Department of Physics and Astronomy University of California, Los Angeles
2016	M.S. Physics University of California, Los Angeles
2016 – 2021	Graduate Student Researcher Department of Physics and Astronomy University of California, Los Angeles
2022	Student Researcher Department of Physics and Astronomy University of California, Los Angeles

PUBLICATIONS

Tang, S. W., Gekelman, W., and Pribyl, P. (in prep.). "Ion Temperature Measurements of Two Flux Ropes in a Laboratory Plasma Experiment".

Gekelman, W., Pribyl, P., Lucky, Z., **Tang, S. W.**, Han, J., and Qian, Y. (2020b). "Design, construction and utilization of a university plasma laboratory". In: *J. Plasma Phys.* **86** (3), p. 925860301. ISSN: 1469-7807. DOI: 10.1017/S002237782000063X.

Gekelman, W., Pribyl, P., Vincena, S., **Tang, S. W.**, and Papadopoulos, K. (2019). "Ferrite based antennae for launching Alfvén waves". In: *Rev. Sci. Instrum.* **90** (8), p. 083505. DOI: 10.1063/1.5103171.

Gekelman, W., **Tang, S. W.**, DeHaas, T., Vincena, S., Pribyl, P., and Sydora, R. (2018b). "Spiky electric and magnetic field structures in flux rope experiments". In: *Proc. Natl. Acad. Sci.* **116** (37), pp. 18239–18244. ISSN: 0027-8424. DOI: 10.1073/pnas.1721343115.

Wu, Z., Sun, W.-Q., Feng, T., **Tang, S. W.**, Li, G., Jiang, K.-L., Xu, S.-Y., and Ong, C. K. (2015). "Imaging of soft material with carbon nanotube tip using near-field scanning microwave microscopy". In: *Ultramicroscopy* **148**, pp. 75–80. DOI: 10.1016/j.ultramic.2014.09.008.

Chapter 1

Introduction

1.1 Background

A flux rope is a bundle of twisted magnetic field lines which encloses a constant magnetic flux. They are created when a current passes through a plasma along the direction of an existing magnetic field, which results in a set of helical field lines that is the superposition of the current's azimuthal magnetic field with the background's guide field. A simplified, illustrative example of a flux rope is shown in Fig. 1.1. The pitch of the magnetic field lines varies radially from the center of the rope, and the bundle of field lines are collectively considered to be the flux rope.

In this dissertation, the energization of ions during the collision and reconnection of two magnetic flux ropes is explored. Two flux ropes in the Large Plasma Device (LAPD) are driven kink-unstable so that they collide with each other and trigger magnetic reconnection of the field lines. In this process, the magnetic field lines rearrange themselves to a lower energy state and release the excess energy stored in the magnetic fields. The results in particles such as ions and electrons being heated and accelerated away from the reconnection site using the released energy.

A retarding field energy analyzer that measures the local ion energy distribution function is built specifically for the purpose of studying ion acceleration and heating from magnetic recon-

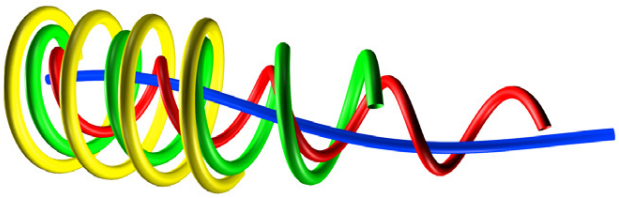

Figure 1.1: A simplified illustration of a flux rope showing a bundle of helical magnetic field lines that radially vary in pitch. Reproduced from Figure 3 of Gekelman et al. (2010).

nection of the two flux ropes. This is a new diagnostic developed for deployment on the LAPD that can locally measure ions with energies below 20 eV. The details are presented and described in this dissertation.

Overall, there is a vast discourse on the subject of flux ropes and magnetic reconnection, and it would not be feasible to present a full review of the topics here. As a result, only a brief review of relevant observations and experiments motivating the study is presented. The first half of the review will focus on flux ropes which is the experimental basis of this study. The second half will focus on ion heating and acceleration specifically in magnetic reconnection. The theme of this study is to bridge these two areas and understand how ions may be energized during magnetic reconnection in the context of two magnetic flux ropes.

1.2 Flux Ropes

1.2.1 Space Observations

Flux ropes are ubiquitous in space and are frequently observed by satellites during space missions or in extreme ultraviolet (EUV) and X-ray imaging of the solar atmosphere. The first use of the term 'flux rope' was by Babcock (1961) who described loop-like structures that were observed on the surface of the Sun. These structures, which are eventually known as coronal loops, would emerge from the chromosphere and create regions on the solar surface with bipolar magnetic fields. These aptly named 'bipolar magnetic regions' could later develop into sunspots and give

rise to sunspot-related activity.

The term 'flux ropes' are now used to describe smaller filamentary structures that appear on the surface of the Sun. Despite their relatively smaller size compared to coronal loops, flux ropes are capable of dissipating large amounts of magnetic energy. For example, the excessive twisting of flux ropes which rise up from the solar surface can rapidly dissipate magnetic energy in the form of intense X-ray emissions (Parker 1975; Priest et al. 1994). These are known as X-ray bright points and are postulated to be a trigger for large interplanetary-scale flux ropes known as magnetic clouds that stretches to a distance between the Earth and the Sun (Mandrini et al. 2005). As an aside, interplanetary-scale flux ropes are also typically associated with coronal mass ejections (CMEs) (Marubashi et al. 2015). However, their formation is a subject of debate (Wang et al. 2018) and not all interplanetary-scale flux ropes appear to be associated with CMEs (Moldwin et al. 1995; Cartwright and Moldwin 2010).

Flux ropes also occur beyond the solar atmosphere. For example, terrestrial flux ropes have been observed in the Earth's magnetotail by space probes such as the International Sun-Earth Explorer (ISEE) (Sibeck et al. 1984; Elphic et al. 1986), Geotail (Lepping et al. 1995; Slavin et al. 2003) and Cluster (Borg et al. 2012). Flux ropes have also been observed in the Earth's magnetopause by the THEMIS spacecraft, where the ions in the core were observed to be heated by about 100 eV when compared to its outer regions (Øieroset et al. 2011).

In early space missions involving other celestial bodies, flux ropes have been observed on unmagnetized bodies that do not have intrinsic magnetospheres such as Venus (Russell and Elphic 1979), Titan (Kivelson and Russell 1983) and Mars (Cloutier et al. 1999; Vignes et al. 2004). The magnetic fields required for these ropes to form are induced by temporary magnetospheres that form when plasma from the solar wind flows around these bodies. Later observations included planetary systems that had magnetospheres similar to Earth. For example, reconnecting flux ropes were observed in flux transfer events in the dayside magnetopause of both Mercury (Slavin et al. 2009; Slavin et al. 2010) and Saturn (Jasinski et al. 2016). These flux transfer events create

short-lived jets of high energy plasma that move towards the Earth. In addition, recent missions to space have continued to discover flux ropes. For example, ion inertial-scale flux ropes have been observed by the Juno spacecraft mission in Jupiter's magnetotail (Sarkango et al. 2021).

All in all, flux ropes are ubiquitous in space. There is a vast body of research written on this topic and some of these reviews include Russell et al. (1990), Khabarova et al. (2021), and Pezzi et al. (2021).

1.2.2 Experimental Studies

The study of flux ropes in a laboratory environment is complementary to space observations and numerical simulations as experiments can be reproduced in an environment where the initial and boundary conditions are controlled (Bellan 2020). Processes that occur in astrophysical flux ropes can be studied in laboratory experiments as magnetohydrodynamic (MHD) plasmas have no intrinsic scale and are identical if they have the same initial conditions and plasma beta (Ryutov et al. 2000). Thus, experiments allow processes such as magnetic reconnection to be studied with geometry that is realistic and physics that is scalable.

One of the earliest experiments with flux ropes involved the simulation of the current and field configurations of a solar prominence using arched magnetic flux ropes created from horseshoe magnets (Bostick 1956). Plasma sources embedded within these magnets would discharge a current that followed the curved magnetic field lines, creating a flux rope shaped as a coronal loop. This experimental configuration was eventually developed to allow the creation of solar prominences with increasing complexity and varying geometries, which are featured in solar corona experiments at Caltech (Bellan and Hansen 1998; Bellan 2020), on the Small Plasma Device at UCLA (Tripathi and Gekelman 2010; Tripathi and Gekelman 2013) and on the Magnetic Reconnection Experiment (MRX) at the Princeton Plasma Physics Laboratory (Myers et al. 2016).

Flux ropes are also produced in linear devices such as on the Large Plasma Device (LAPD) at

UCLA, which is the setup for this study. Another example is the Reconnection Scaling Experiment (RSX) at Los Alamos National Laboratory (Furno et al. 2003), where flux ropes are created by plasma guns that injected parallel current along the magnetic field. This creates two gyrating helices that rotate due to the kink instability and are mutually attracted each other (Intrator et al. 2009). At locations where the ropes collide, they could bounce off each other or behave stochastically instead of coalescing. This depended on the balance between the attractive forces between the ropes and the repulsive forces that bend the magnetic field lines and elastically compress the plasma (Sun et al. 2010).

1.3 Previous Studies on the Large Plasma Device (LAPD)

The first flux rope experiments performed on the LAPD involved the interaction of two parallel current channels were created in a high beta plasma (Pfister 1991). The ropes were created in an earlier version of the LAPD which was 10 m long (Gekelman et al. 1991) and were made to relax into a Taylor state where $\boldsymbol{J} \times \boldsymbol{B} = 0$ (Taylor 1974). This was done by drawing a net current through the ropes. As the rope currents twist and merge, the rate of change of helicity (i.e. the amount of twisting in the magnetic field lines) was measured and found to agree with theoretical MHD models (Gekelman et al. 1992).

Studies of flux ropes resumed in 2009 after the upgrade of the LAPD in 2001 to its current 20 m long version (Gekelman et al. 2016b). The first study involved the first experimental identification of a quasi-sepratrix layer (QSL), a three-dimensional (3D) generalization of a magnetic sepratrix which is used to indicate regions of discontinuous magnetic topology (Lawrence and Gekelman 2009) and identify regions of 3D magnetic reconnection where null points do not exist (Priest and Démoulin 1995). This was later used to identify magnetic reconnection in a two flux rope experiment, an Alfvén wave laser-produced plasma (Gekelman et al. 2010), and then to an experiment with three flux ropes (Gekelman et al. 2012; Van Compernolle and Gekelman 2012).

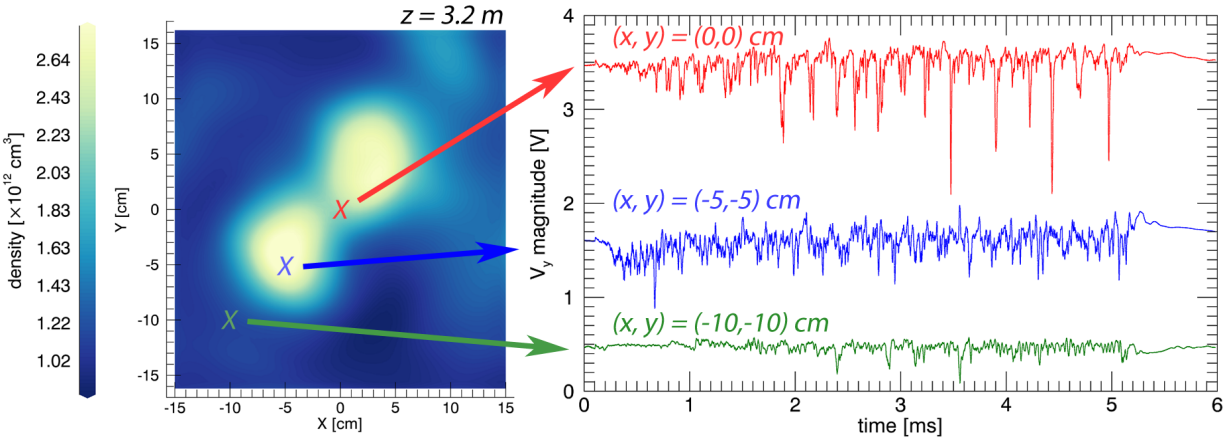

Figure 1.2: (Left) A 2D cross-section of the plasma density indicating the positions of the flux ropes at $z = 3.2$ m. The three color-coded X's mark the points in which the electric potential was measured. (Right) The corresponding electric potential measurements in the y-direction.

Subsequent LAPD flux rope experiments involved characterizing various aspects of the two flux ropes during magnetic reconnection. For example, the two ropes were shown to exhibit behaviors of deterministic chaos based on a complexity-entropy mapping of its time-based magnetic field signals (Gekelman et al. 2014). Chaotic behavior was also observed in a single flux rope during a parametric study of various discharge conditions which exhibited an exponential frequency spectrum (DeHaas et al. 2015). In addition, the nonlinear reconnection rate based on the parallel electric fields (Gekelman et al. 2016a) and the transformation and conservation of magnetic helicity of the two ropes (DeHaas and Gekelman 2017) were quantified. This eventually led to a full-scale quantization of the two flux ropes with all the measurable terms in Ohm's law to determine the resistivity of the plasma (Gekelman et al. 2018a). Ohm's law was then found to be non-local which required the use of the AC Kubo resistivity (Kubo 1966).

1.3.1 Motivation

In recent flux rope experiments, spiky structures have been observed in electric potential measurements of the two flux ropes at positions such as the region between the two ropes where magnetic reconnection occurs and at the edge of each rope (Gekelman et al. 2018b). An example

of these structures are shown on the right of Fig. 1.2 for $(x, y) = (0, 0)$ cm. These structures of remniscent of Time Domain Structures (TDS), a term used to collectively describe various narrow, intense spikes that appear in the time-based electric field measurements of satellite observations and laboratory experiments (Mozer et al. 2015). TDS appear to play an important role in magnetic reconnection as the large parallel electric fields that are present in them can be used to accelerate and energize particles (Drake et al. 2003). However, statistical analysis of the spiky structures in the flux ropes suggests that they are not associated with known classes of TDS such as electron phase space holes or double layers, and appear to be driven by dynamics on the scale of the ions. For example, the spikes move on the order of the ion thermal velocity and their sizes are much larger than the Debye length of the plasma (i.e. on the order of cm instead of μm).

Nevertheless, the presence of these spiky structures raises questions as to how they are produced and what their roles are in relation to the flux ropes. Since these structures appear to emanate from the region between the ropes where reconnection is known to occur, they may be the end result of turbulent processes that occur during magnetic reconnection. This is usually accompanied by ion heating and acceleration. In addition, even though previous studies on the LAPD have quantified most of the measurable parameters of the two ropes and determined the reconnection topology using the QSL (Gekelman et al. 2018a; Gekelman et al. 2020a), the ion dynamics of the ropes during reconnection remain largely unexplored. It is generally known that magnetic reconnection can accelerate and heat ions, and magnetic reconnection is frequently observed in the two flux rope system. Thus, an investigation of the ion dynamics that occurs during the reconnection of the two ropes would help fill this gap and elucidate the origins of spiky structures such as those observed in Fig. 1.2.

1.4 Ion Dynamics in Magnetic Reconnection

1.4.1 Models of Magnetic Reconnection

In two dimensions, magnetic reconnection can be described by qualitative models such as the one established by Sweet (1958) and Parker (1957). The Sweet–Parker model was originally used to describe solar flares and explain the phenomenon in which a build up of energy in the magnetic fields was suddenly released in the form of kinetic and thermal energy in the plasma. In this resistive MHD model, reconnection occurs when two topologically distinct plasmas with magnetic field lines directed opposite to each other are brought together by an inflow speed v_{in}. This causes the magnetic field lines to merge, annhilate and reform within a thin boundary layer known as the diffusion region or reconnection layer, which is characterized by dimensions of length L and thickness δ.

Since the plasma is assumed to be incompressible, flux conservation requires the outflow speed of the plasma v_{out} to be

$$v_{\text{out}} = \frac{L}{\delta} v_{\text{in}} \ , \tag{1.4.1}$$

which is shown to depend on the aspect ratio δ/L of the diffusion region. In addition, v_{out} has to satisfy the pressure balance at the center of the diffusion region

$$p_0 + \frac{B_0^2}{2\mu_0} = p_0 + \frac{1}{2}\rho v_{\text{out}}^2 = \text{const.} \ , \tag{1.4.2}$$

where p_0 is the pressure outside the diffusion region, B_0 is the magnetic field along the inflowing regions, μ_0 is the vacuum permittivity and ρ is the density of the plasma. This means that

$$v_{\text{out}} = \frac{B_0}{\sqrt{\mu_0 \rho}} \equiv v_A \ , \tag{1.4.3}$$

and therefore particles are expected to be jetted out from the reconnection site at the Alfvén speed v_A.

Furthermore, assuming the plasma is resistive and obeys Ohm's law

$$\boldsymbol{E} + \boldsymbol{v} \times \boldsymbol{B} = \eta \boldsymbol{J} \tag{1.4.4}$$

where η is the Spitzer resistivity (Spitzer Jr. and Härm 1953), this allows Lundquist number S to be defined as

$$S \equiv \frac{\mu_0 L v_A}{\eta} \ , \tag{1.4.5}$$

where S is also the ratio of resistive diffusion time τ_R (time it takes for the magnetic field lines to diffuse across the region) to the Alfvén transit time τ_A (time it takes for an Alfvén wave to travel across the system). These are given by

$$\tau_R = \frac{\mu_0 L^2}{\eta} \qquad \text{and} \qquad \tau_A = \frac{L}{v_A} \ .$$

In the Sweet–Parker model, the normalized reconnection rate R_r is related to S by

$$R_r \sim \frac{1}{\sqrt{S}} = \sqrt{\frac{\eta}{\mu_0 L v_A}} \ . \tag{1.4.6}$$

This results in an extremely slow rate of reconnection which is unlikely for most laboratory and astrophysical settings as S is usually very large (i.e. $S \gg 1$) (Priest and Forbes 2007). However, because other aspects of the Sweet–Parker model have been proven to be valid by numerical simulations (Biskamp 1986) and experiments such as those on MRX[1] (Ji et al. 1998), the Sweet–Parker model is generally considered an appropriate approximation for magnetic reconnection.

[1] with modifications to the Sweet–Parker model

Many different models then complement the Sweet–Parker model with other properties to explain the faster reconnection rate. These include the model of slow shocks by Petschek (1964), anomalous resistivity (Chen et al. 1984; Ugai 1984) and Hall reconnection (Drake et al. 2008). Consequently, a wide variety of discussions on 2D magnetic reconnection models can be found in review papers such as Zweibel and Yamada (2009), Yamada et al. (2010), and Treumann and Baumjohann (2013).

For the flux ropes on the LAPD, three-dimensional magnetic reconnection models are used. These differ from two-dimensional magnetic reconnection in a number ways. For example, reconnection can occur in the absence of neutral points known as quasi-sepratrix layers (QSLs), which are characterized by steep gradients of magnetic field lines (Priest and Démoulin 1995). They also have continuous field lines and these field lines tend to continuously reconnect at multiple points when they are within the diffusion region (Priest et al. 2003). In addition, pairs of flux tubes do not break and recombine to form two new pairs as half the flux tube would rejoin a different half of the flux tube instead. This difference in behavior and the additional dimension increases the complexity of 3D reconnection. Furthermore, the inclusion of a guide field in 3D reconnection results in a wider class of instabilities that can produce structures in the out-of-plane dimension (Pritchett and Coroniti 2004). Some of these include the Buneman (1959), drift kink (Zhu and Winglee 1996) and ion kink instabilities (Daughton 1999).

In practice, 3D reconnection models help to identify regions where magnetic reconnection is likely to occur (Pontin 2011). These are frequently used in the study of astrophysical plasmas such as in solar flares (Janvier 2017; Li et al. 2021). In the LAPD, the QSL was used to identify regions of magnetic reconnection for the two flux rope experiment (Lawrence and Gekelman 2009). It was later discovered that the topological winding number, a mathematical quantity which measures the entanglement of field line pairs, can also be used to determine regions of magnetic reconnection (Gekelman et al. 2020a).

1.4.2 Reconnection Experiments with Ion Heating and Acceleration

There are a number of laboratory studies exploring ion energization in systems involving magnetic reconnection. However, experimental studies of ion energization in flux ropes are very rare. Thus, most examples of ion energization experiments in literature usually have plasmas in configurations other than flux ropes.

The most common source of reconnecting plasmas is from the merging of two spherical or toroidal plasma sources. One example is the TS-3 merging device which involves the merging of two counterhelicity toroidal plasmas (Ono et al. 1996). Ions were heated up to 200 eV and were accelerated to Alfvén speeds, which was attributed to tension forces in the reconnected magnetic field lines. These observations agree with three-dimensional MHD simulation of two merging flux tubes with counterhelicity magnetic fields. It was also estimated that 78% of the dissipated magnetic field energy was imparted to the ions.

Another example is the Magnetic Reconnection Experiment (MRX), which conducted an ion heating experiment by merging two flux cores with toroidal and poloidal fields under various magnetic field configurations (e.g. co-helicity and null-helicity) (Hsu et al. 2001). The local ion temperature was then measured using an optical probe via Doppler spectroscopy (Fiksel et al. 1998). The ions were found to be sub-Alfvénic and the heating of the ions was greater for the null-helicity case ($6 \rightarrow 17$ eV) as compared to co-helicity case ($3 \rightarrow 7$ eV). As the plasma parameters and the helicity of the plasma sources of the MRX experiment are similar to the LAPD flux ropes, some of the implications are discussed in Chapter 6.3. In addition, the MRX measured the energy conversion budget of magnetic energy in the reconnection layer and found that 50% of the magnetic energy is converted to particle energy, of which two-thirds goes to ions (Yamada et al. 2014).

In the Swarthmore Spheromak Experiment (SSX), two spheromaks were carefully and partially merged to study 3D magnetic reconnection. The ion flow was measured using a retarding field energy analyzer and protons with an average energy of 70 eV were observed moving within the

reconnection plane (Brown 1999). In the direction normal to the reconnection plane, super-Alfvénic ions with a 90 eV drift were observed in a background of 30 eV superthermal ions. The presence of the 90 eV ions were correlated with 3D reconnection events and were consistent with test particle simulations of the same experiment (Brown et al. 2002).

In other configurations such as the reversed-field pinch experiment at the Madison Symmetric Torus, the process of ion heating in which magnetic field energy is converted to ion thermal energy was investigated. Ions were heated in excess of hundreds of eV during impulsive reconnection events known as sawtooth crashes, and the amount of heating was found to be dependent on their mass (Fiksel et al. 2009) and their charge-to-mass ratio (Kumar et al. 2013). In addition, it was reported that 10 to 30% of the magnetic energy goes into ion heating which increases with the square root of the ion mass.

1.5 Dissertation Objectives and Outline

In this dissertation, the primary objective is to investigate the energization of ions from two flux ropes as they collide with each other and reconnect within the Large Plasma Device (LAPD). This is achieved by designing and constructing a retarding field energy analyzer that measures the localized ion energy distribution function of the plasma. The ion energy analyzer is then deployed in a well-characterized two flux rope system with detailed, volumetric measurements of quantities such as the magnetic field, density and electric potential.

The experimental goals of this study are three-fold: the first is to construct an ion energy analyzer compatible with the LAPD and to verify that it works by comparing its data with another method such as Doppler spectroscopy; the second is to determine whether ion heating and/or acceleration had occurred during the reconnection of the ropes; and the third is to determine how ion heating or acceleration could have occured if it existed. The dissertation is thus organized as follows:

Chapter 1 summarizes the background and motivation for this work. Examples of space observations and laboratory experiments of flux ropes, magnetic reconnection and ion heating are presented.

Chapter 2 describes the Large Plasma Device (LAPD), the various diagnostic capabilities and the setup of the two flux rope system.

Chapter 3 presents experimental data showing the spatial structure of the two flux ropes.

Chapter 4 describes the design and the construction process of the ion retarding field energy analyzer.

Chapter 5 presents experimental data measured by the ion energy analyzer and how the average energy $\langle 2E \rangle$, a quantity equivalent to the Maxwellian temperature, is determined. The results are compared to the ion temperature obtained from Doppler line broadening in spectroscopy.

Chapter 6 presents a construction of the two-dimensional distribution function using polar plots. The correlation between the ion beam measured by the ion energy analyzer and magnetic reconnection is discussed together with its implications.

Chapter 7 concludes the dissertation by summarizing the results of the study.

Appendix A presents a derivation of the space charge limited current for ions in a gridded energy analyzer. The resulting equation is used in Chapter 4.4.1.

Chapter 2

Experimental Setup

2.1 The Large Plasma Device

The Large Plasma Device (LAPD) is a 26-meter long experimental plasma physics device located at the University of California, Los Angeles (UCLA). It was first constructed in 1991 as a 10 meter long device used to study Alfvén waves, but was later upgraded in 2001 to a 20-meter long device with funding and support from the National Science Foundation and the United States Department of Energy (Gekelman et al. 1991; Gekelman et al. 2016b). Since then, the LAPD has been part of the Basic Plasma Science Facility, a national collaborative user facility that is dedicated to the study of fundamental plasma physics.

Fig. 2.1 are two images of the LAPD: Fig. 2.1a is a stitched photograph showing the full length of its exterior before a cathode upgrade in 2021 whereas Fig. 2.1b is a schematic drawing of the device after the upgrade showing internal components that produce the two flux ropes. These components are described in the following subsections.

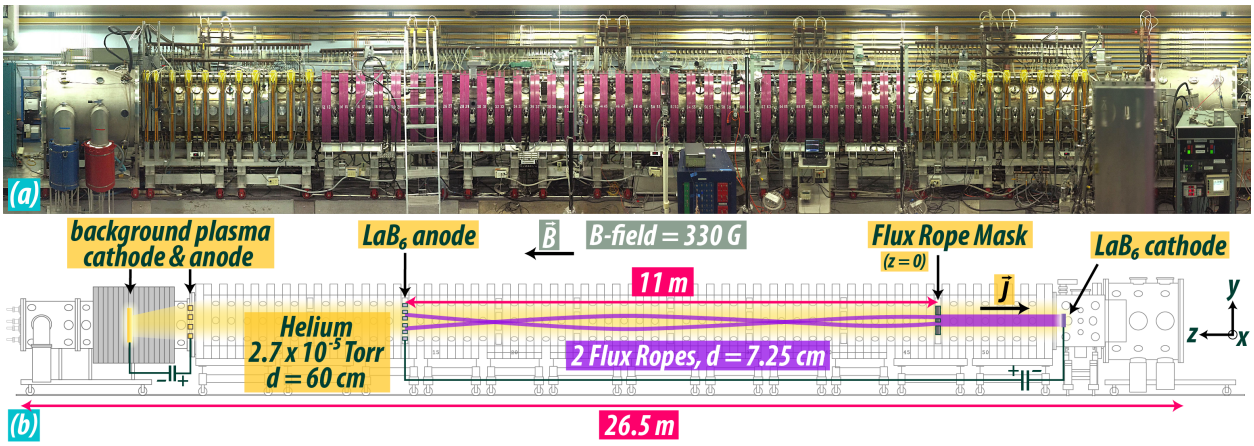

Figure 2.1: (a) A photograph showing the exterior of the Large Plasma Device (LAPD) before the cathode upgrade in 2021. Reproduced with permission from Timothy DeHaas (2012). (b) A schematic of the interior after the upgrade showing the set-up for the two flux rope experiment.

2.1.1 Vacuum Chamber

The main body of the LAPD is a cylindrical, stainless steel chamber that is 26.5 m long and 1.5 m in diameter. It contains two end chambers with magnetically levitated turbo-molecular pumps that are used to evacuate the vessel to a base pressure of 5×10^{-7} Torr[1] (Gekelman et al. 2016b). The chamber is then filled with a gas, typically helium, until the chamber pressure reaches approximately 3×10^{-5} Torr. Other gases such as hydrogen, neon or argon may also be used. The flow of gas into the vessel is precisely measured and regulated by a series of mass flow controllers.

2.1.2 Magnetic Field

The vacuum chamber of the LAPD is encapsulated by at least a hundred yellow and magenta solenoidal electromagnets that line the exterior of the device as seen in Fig. 2.1. These electromagnets are spaced approximately 40 cm apart from each other and provide a background magnetic field which magnetizes the plasma along the chamber. Each electromagnet is driven by kiloamp currents that are independently controlled by an external programmable power supply.

[1] 1 Torr ≈ 133.33 Pa

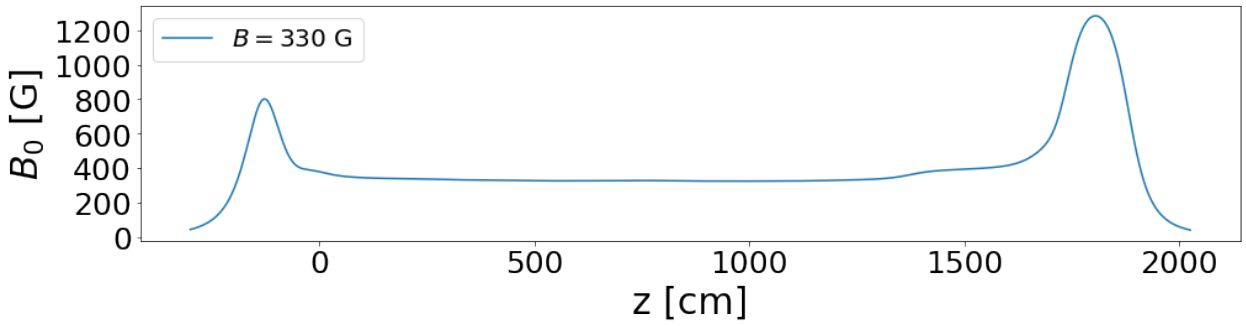

Figure 2.2: The background magnetic field profile as a function of z for the two flux rope experiment. The LaB_6 cathode is located at $z = -64$ cm, while the flux ropes are located between $z = 0$ and $z = 1100$ cm.

The current delivered to each electromagnet is capable of producing magnetic fields of up to 2 kG and can be used to create a variety of magnetic field configurations along the device.

Fig. 2.1b shows the position of the flux ropes which are located between $z = 0$ to 1100 cm. A carbon mask (Fig. 2.3b) determines $z = 0$ cm and the $+z$-direction is towards the background plasma cathode. The magnetic field configuration along LAPD is shown in Fig. 2.2, and is constant at 330 G with respect to the flux ropes. The values were determined by the LAPD housekeeper system which calculates the magnetic field at the center of the machine based on the current flowing through the solenoid magnets and were verified by previous LAPD experiments (Gekelman et al. 2016b).

2.1.3 Background Plasma Source

The data in this study was acquired from flux ropes with two different background plasma sources. Reference data acquired prior to and for this study was obtained with a barium oxide (BaO) cathode that was located on the left end of the chamber as shown in Fig. 2.1b. The cathode was a 72 cm nickel plate coated with barium oxide heated to $750°$C (Leneman et al. 2006). Electrons were thermionically emitted from the cathode and accelerated towards a molybdenum anode mesh placed 50 cm in front of the cathode. The anode was placed in close proximity to

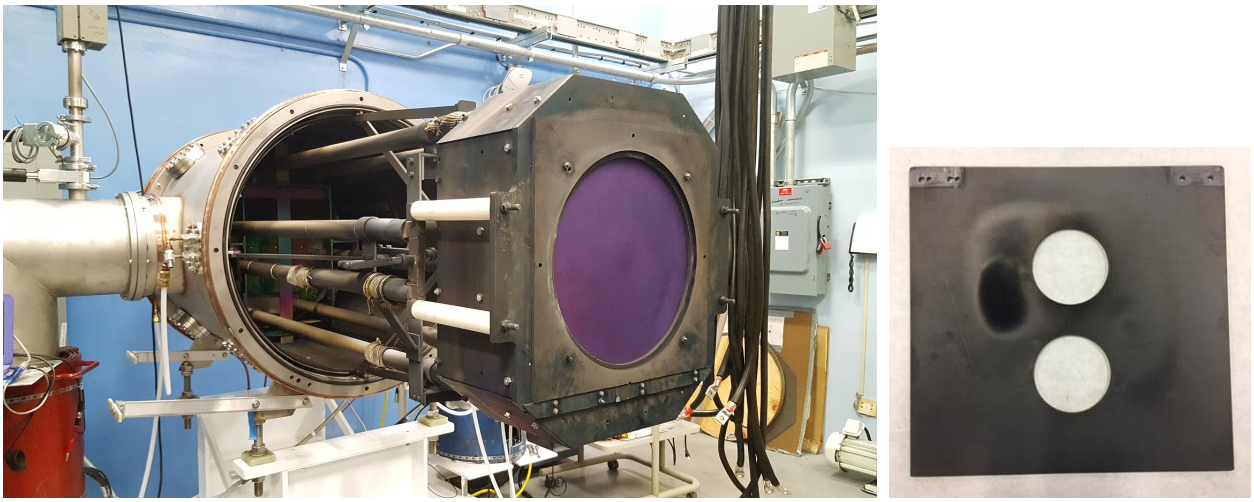

Figure 2.3: (a) The LaB_6 cathode that is used as the background plasma source after an LAPD cathode upgrade in February 2021. (b) The carbon mask used to create the two flux ropes. Each hole is 7.6 cm (3 inches) in diameter.

the cathode ensure that there was no net current in the plasma. The anode was then pulsed with a bias voltage of 25 and 70 V with respect to the cathode during each discharge. The charge was delivered by a capacitor bank that was controlled by a transistor switch, and each discharge lasted for 15 ms with a repetition rate of 1 Hz. This created a plasma column 18 m long and approximately 60 cm in diameter that depended on the magnitude of the B-field in the LAPD. The peak density of the BaO plasma was approximately 3×10^{12} cm^{-3}.

The cathode was later upgraded to a lanthanium hexaboride (LaB_6) source as shown in Fig. 2.3a. The new cathode is 15 inches (38.1 cm) in diameter and is housed in a chamber that produces strong magnetic fields (~ 3–4 kG). During operation, the cathode is heated to $1850°$C and the strong magnetic fields help to push plasma and the thermionically emitted electrons into the main chamber. The setup of the anode for the LaB_6 plasma source is identical to that of the barium oxide plasma source. A plot of the discharge current from the LaB_6 background cathode as a function of time is shown in green in Fig. 2.4. The density of the background plasma produced by the LaB_6 cathode is up to 2×10^{13} cm^{-3}.

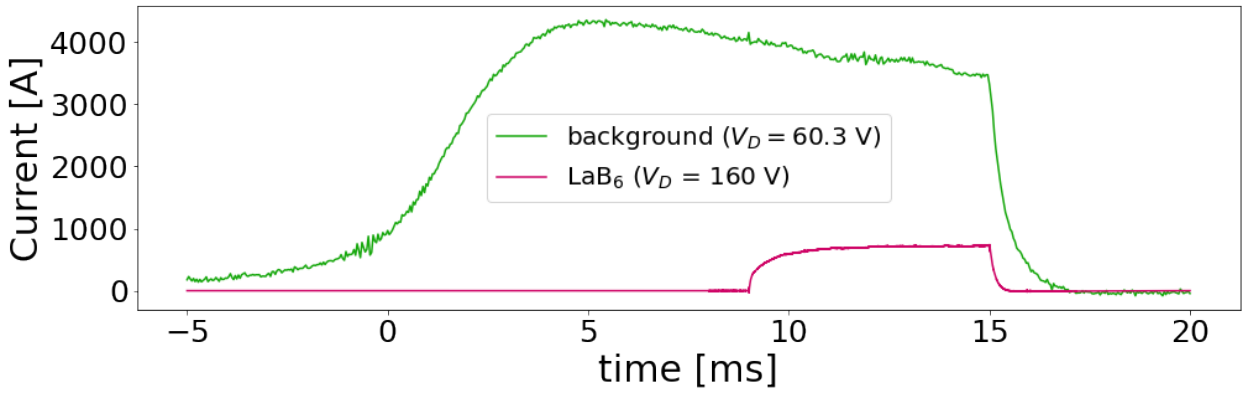

Figure 2.4: Time traces of the discharge current measured between the background and flux rope LaB_6 cathodes during a single discharge cycle of the plasma. The background plasma is turned on before $t = 0$ ms, while the flux rope plasma source is turned on when the background plasma current has roughly stabilized at $t = 9$ ms. The current between the flux rope cathode and anode is for two ropes (i.e. $2I_R$). Both cathodes shut off at $t = 15$ ms.

2.1.4 Flux Rope Plasma Source

The two flux ropes are created with secondary LaB_6 cathode placed on the other end opposite to the background plasma cathode source. This is the cathode positioned on the right of Fig. 2.1b. The cathode comprises of 4 square LaB_6 tiles with a total area of 20.3×20.3 cm^2 and is heated to $1750°$C during operation (Cooper et al. 2010). To shape the two flux ropes, an electrically floating carbon mask with two 7.6 cm (3 inch) diameter holes separated 3 cm edge-to-edge is placed 64 cm away from the LaB_6 cathode source (i.e. $z = -64$ cm). A photo of the carbon mask is shown in Fig. 2.3b.

The current of the flux ropes terminate on a square molybdenum mesh anode (30×30 cm^2) placed a distance $\Delta z = 11$ m away from the carbon mask. This determines the length of the flux ropes. The ropes are free to move and slide along the anode and are thus not line-tied (Ryutov et al. 2006).

Like the background plasma, the discharge of the flux rope cathode is controlled by a transistor switch attached to the capacitor bank of the circuit and has a repetition rate of 1 Hz. However, it only discharges within the last 6 seconds of the background plasma when it is assumed to be

Table 2.1: Plasma parameters of the LAPD.

	Parameter	Value
n	plasma density	2×10^{12} cm^{-3}
T_e	electron temperature	$7 - 10$ eV
T_i	ion temperature	$4 - 7$ eV
f_{pe}	electron plasma frequency	12.7 GHz
f_{pi}	ion plasma frequency	148.5 MHz
c/ω_{pe}	electron inertial length	0.4 cm
c/ω_{pi}	ion inertial length	32.3 cm
ν_{ee}	electron-electron collision frequency ($T_e = 7$ eV)	3.2 MHz
ν_i	ion-ion collision frequency ($T_i = 4$ eV)	30.1 kHz
λ_D	Debye length ($T_e = 7$ eV)	13.9 μm
c_s	Ion sound speed ($T_e = 7$ eV)	1.3×10^6 cm/s
v_{Ti}	Ion thermal speed ($T_i = 4$ eV)	9.8×10^5 cm/s
B	background magnetic field	330 G
f_{ce}	electron cyclotron frequency	924.4 MHz
f_{ci}	ion cyclotron frequency	125.7 kHz
ρ_e	electron gyroradius ($T_e = 7$ eV)	190.8 μm
ρ_i	ion gyroradius ($T_i = 4$ eV)	1.2 cm
β	plasma beta	0.0052
v_A	Alfvén velocity	2.5×10^7 cm/s
I_{KS}	Kruskal–Shafranov limit current ($a = 3.81$ cm, $L = 1100$ cm)	136.8 A

in steady state. A plot of the flux rope discharge current is shown in purple in Fig. 2.4. The discharge voltage of the flux rope cathode is between 80 and 160 V. Together with the background plasma, flux ropes with densities of up to 5×10^{12} cm^{-3} can be produced.

2.2 Plasma Parameters

Table 2.1 summarizes the relevant plasma parameters for the two flux rope experiment. The plasma is considered magnetized as these dimensions are at least an order larger than the electron and ion gyroradii (ρ_e, ρ_i). The scale of the system (i.e. the length of the flux ropes) is also larger than the electron inertial length c/ω_{pe} and the Debye length λ_D, but smaller than the ion inertial

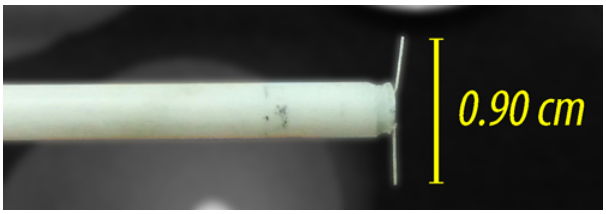

(a) Electric dipole probe

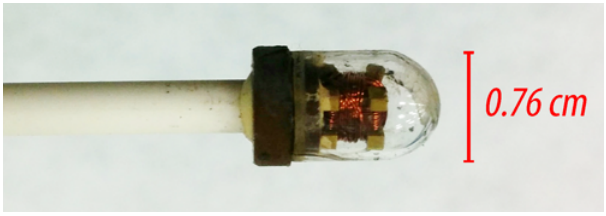

(b) B-dot probe

(c) Mach probe (also a Langmuir probe)

Figure 2.5: Photos of some fundamental diagnostic probes used in this study.

length c/ω_{pi} in the perpendicular direction.

2.3 Diagnostic Probes

Diagnostic probes are used to measure physical quantities at localized positions within the machine. The probe heads are typically less than a centimeter to avoid disturbing the plasma and they are mounted on aluminum probe shafts approximately 1.3 m long with Viton® O-rings attached to it. These O-rings prevent the breaking of vacuum as the probe shaft slides in and out of the device through a metal feedthrough connected to one of over 450 diagnostic ports uniformly spaced along the length of the machine (Gekelman et al. 2016b).

Fig. 2.5 shows some of the fundamental diagnostic probes used in this study. They are built and assembled by-hand within the facility and consist of (a) an electric dipole probe, which measures the electric potential and electric fields; (b) a B-dot probe, which measures change in the magnetic field as a function of time; and (c) a Mach probe, a variation of the Langmuir probe which measures flow velocity. As a Langmuir probe, it measures the plasma density n, plasma potential V_p and electron temperature T_e. The ion retarding field energy analyzer used in this

study and is built as a diagnostic probe and will be discussed in Chapter 4. The details of the other probes are elaborated in the following subsections.

2.3.1 Electric Dipole Probe

The electic dipole probe shown in Fig. 2.5a consists of two metal whiskers that protrude out of a cylindrical ceramic shaft. The whiskers are about 0.4 cm long each and are made of stainless steel. They were made by stripping off the insulation of a high-frequency coaxial cable at the probe tip. The insulation of the rest of the wires remain intact and are protected by a ceramic tube.

A single whisker of the electric dipole probe measures the floating potential of a localized point with respect to ground. The signals from both whiskers are differentially subtracted from each other and divided by the tip separation to obtain a signal proportional to the local electric field and along the direction parallel to the two whiskers. This signal cannot be calibrated due to sheaths that form around the probe tips.

2.3.2 B-dot Probe

Fig. 2.5b shows the head a B-dot probe which measures $\frac{\partial B}{\partial t}$, the rate of change of the localized magnetic field (Lovberg 1965; Everson et al. 2009). Although the figure shows copper wire loops wound on a Vespel™ cube and enclosed within a pill-shaped glass cap, the upgraded version of the B-dot probes used in this study feature ceramic-coated wires and a ceramic cap that can withstand the heat flux of the LaB_6 plasma.

The Vespel™ cube is 0.3 mm in length and consists of 3 sets of wire loops wound around it, one for each coordinate axis in Cartesian space. The wire loops consist of a pair of differential wound wires in which a subtraction of the signals from both wires amplifies the magnetic field signal and eliminates the common-mode signal that is present in a single wire loop. In addition,

the strength of the probe signal depends on the number of turns of wire around the Vespel™ cube. In this study, the B-dot probes used have either 10 or 50 turns of wire.

B-dot signal calibration The voltage signal obtained from the B-dot probe is proportional to the rate of change of magnetic flux Φ and is calculated using Faraday's law (i.e. $V \propto -\frac{dB}{dt}$). However, the effective area of the wire loop perpendicular to each of the three axes has to be determined from calibration.

This is performed with the help of a Helmholtz coil and a vector network analyzer which measures the phase and amplitude response of a circuit while varying the frequency of the input signal. The vector network analyzer induces the Helmholtz coil to produce a magnetic field of known strength over a range of different frequencies while measuring the response of the B-dot probe in various orientations with respect to the Helmholtz coil. The frequency response of the B-dot probe is usually linear for frequencies lower than 5 MHz.

The calibration also corrects for the angle of the wire loops due to misorientation. This is necessary for probes which are found to have significant contributions from the off-axis B-dot signals. The correction for each axis is determined by adjusting the angle of the loop until the off-axis signal is at a minimum.

Finally, the localized magnetic field strength B is calculated by numerically integrating the probe signal with respect to time,

$$B = \frac{\int V_{\text{probe}} \cdot \mathrm{d}t}{gNA} \ , \tag{2.3.1}$$

where V_{probe} is the signal from the B-dot probe, g is the gain of the amplifier used in the experiment, N is the number of turns and A is the area of the wire loop. The product NA is the effective area of the probe.

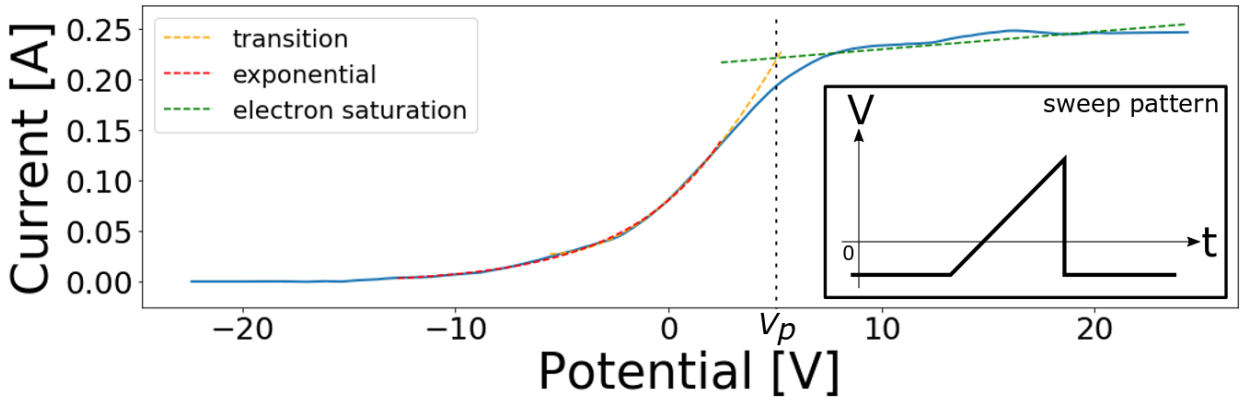

Figure 2.6: An example I-V curve showing curves fit to three different regions. The plasma parameters obtained from fitting the curve are density $n = 1.3 \times 10^{12}$ cm^{-3}, electron temperature $T_e = 4.6$ eV and plasma potential $V_p = 5.1$ V. The inset shows a typical voltage sweep pattern used to obtain the curve.

2.3.3 Langmuir Probe

The Langmuir probe (also the Mach probe in Fig. 2.5c) consists of a small metallic conductor used to estimate the density, potential and the electron temperature of a localized region within the plasma. The conductor is constantly biased with respect to chamber ground at a large negative potential as shown in the inset of Fig. 2.6. During a voltage sweep, the potential is increased linearly until it reaches a large positive bias. The current collected by the probe I as a response to the increasing bias potential is then recorded and plotted as a function of the bias potential V. The result is an I-V curve as shown in Fig. 2.6.

The density n, plasma potential V_p and electron temperature T_e of the plasma are determined from analyzing the I-V curve. The theory is well documented and a variety of methods have been proposed in literature (Hershkowitz 1989; Chen 2001; Merlino 2007). In general, the density n is obtained from the electron saturation current, the electron temperature T_e from the growth rate of the exponential region near $V = 0$ (either through curve fitting or taking the derivative), while the plasma potential V_p is estimated to be the potential at which the probe begins to be completely saturated by the electron current.

2.3.4 Mach Probe

The Mach probe (sometimes called a *Janus probe*) is a variant of the Langmuir probe in which two conductors are placed back-to-back to measure the ion saturation current simultaneously and determine the ion flow velocity v_d. The two conductors are electrically insulated from each other, but have faces whose normal are directed along the axis of the measured ion flow and are in opposite directions. The Mach number M, which is the ratio of the ion flow velocity v_d to the ion sound speed c_s, is expressed as

$$M \equiv \frac{v_d}{c_s} \ .$$

In Fig. 2.5c, the Mach probe has three pairs of oppositely directed conductors, a pair for each direction along the three Cartesian axes. The conductors are made from tantalum wire that is flattened to a paddle-like shape with a vice clamp, and then attached to opposite sides of a non-conducting Vespel™ cube. The entire probe head is then epoxied while exposing a square area that is approximately 0.25 cm in length (~ 6.25 mm^2 area) on each side of the probe head.

Experimentally, the Mach number can be obtained using the general formula

$$M = \frac{1}{K} \ln\left(\frac{I_u}{I_d}\right) \ , \tag{2.3.2}$$

where K is a constant of order unity, while I_u and I_d are the upstream and downstream ion saturation currents along the direction normal to the probe faces respectively.

A caveat of using the above equation is that the value of K depends on the magnetization of the plasma with respect to the Mach probe, which often requires a comparison of the size of the probe head d to the ion gyroradius ρ_i. In the strongly magnetized case of $d \gg \rho_i$, the value of K can be obtained from established theoretical fluid models (Stangeby 1984; Chung et al. 1989; Hutchinson 2008; Patacchini and Hutchinson 2009).

However, the value of K for weakly magnetized ($d \approx \rho_i$) or unmagnetized ($d \ll \rho_i$) plasmas is undefined. This is due to competing theories and models (Hudis and Lidsky 1970; Shikama et al. 2005) with no consensus on an appropriate model to be used in literature (Hutchinson 2002; Oksuz and Hershkowitz 2004; Chung 2006). As the ion gyroradius ($\rho_i = 12.4$ mm for $T_i = 4.0$ eV, $B = 330$ G) is typically larger than the size of the Mach probe on the LAPD ($d = 2.5$ mm), this regime is considered unmagnetized and K is usually approximated to be 1.

2.3.5 Probe to LAPD Coordinate System

The probes enter the device through one of the over 450 diagnostic ports that are located on the walls of the vacuum vessel. In each of these ports, a vacuum-compatible ball valve allows an angle of motion that is within 60° of the port opening while the probes slide in and out of the chamber without breaking vacuum (Leneman and Gekelman 2001). In addition, the probe may also be attached to a probe drive that automatically moves the probe tip to a user-specified position on the data acquisition system, allowing planar (e.g. xy, xz) or volumetric (e.g. xyz) datasets to be taken.

As the coordinate system of the probe is not aligned with the coordinate axis of the LAPD, data collected with the probe has to be corrected so that the coordinate system matches the LAPD.

Fig. 2.7 shows the coordinate system of the probe. The left of the diagram shows a three-dimensional view while the inset on the right shows the side view at the interface of an LAPD port. The unprimed coordinates are in the frame of reference of the LAPD, while the primed coordinates are with respect to the probe tip.

The LAPD defines the $+z$-direction to be in the direction of the background magnetic field which faces the south end of the machine, while the $+y$-direction is pointing upwards. Thus, when diagnostic probes are inserted into the LAPD, they tend to face the negative x-direction. Fig. 2.7 shows this but the coordinate axes are drawn in $-x$ and $-z$ directions instead to avoid

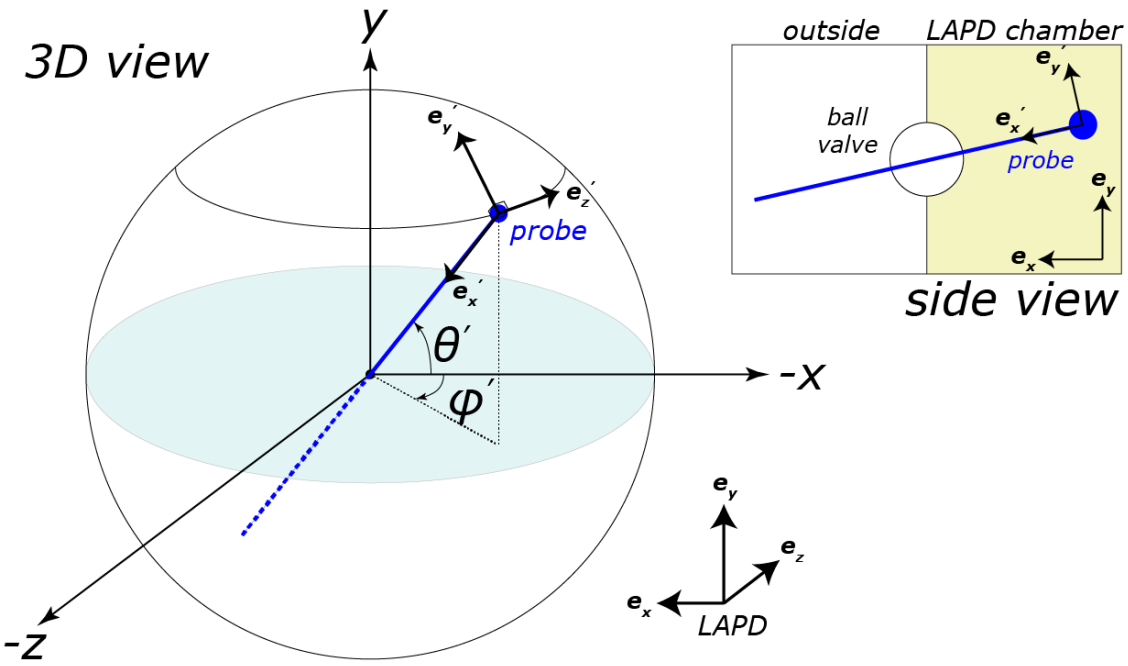

Figure 2.7: The coordinate system for a probe pivoted by a spherical ball valve on the LAPD. A three-dimensional view is shown on the left, while a side view across the xy-plane is shown on the inset on the right. The probe tip is indicated by the blue dot. Each ball valve is located at a different z position.

over-cluttering the diagram. The unit vectors of the LAPD are shown at the bottom.

Defining the angles θ' and φ' with respect to the $-x$ axis, this allows a transformation from the probe coordinates to the LAPD coordinates using the orthogonal matrix

$$\underbrace{\begin{pmatrix} \boldsymbol{e}_x \\ \boldsymbol{e}_y \\ \boldsymbol{e}_z \end{pmatrix}}_{\text{machine}} = \begin{pmatrix} \cos\theta'\cos\varphi' & \sin\theta'\cos\varphi' & -\sin\varphi' \\ -\sin\theta' & \cos\theta' & 0 \\ \cos\theta'\sin\varphi' & \sin\theta'\sin\varphi' & \cos\varphi' \end{pmatrix} \underbrace{\begin{pmatrix} \boldsymbol{e}'_x \\ \boldsymbol{e}'_y \\ \boldsymbol{e}'_z \end{pmatrix}}_{\text{probe}} . \tag{2.3.3}$$

When $\theta' = \varphi' = 0$, the axes of the probe line up with the machine coordinates. For probes that

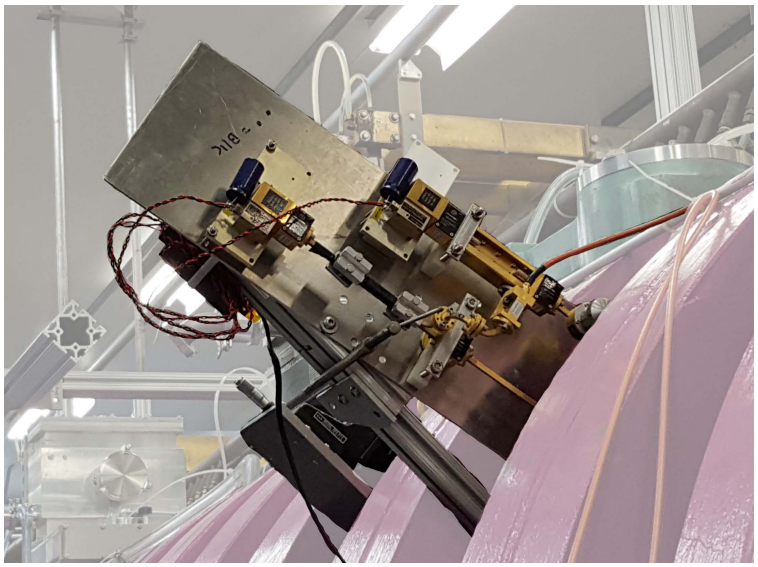

Figure 2.8: A microwave interferometer that is used to measure the line-of-sight density of the plasma in the LAPD. It is attached to a side window that is angled 45-degrees with respect to the LAPD chamber.

move only within the xy-plane, $\varphi' = 0$ and (Eq. 2.3.3) becomes

$$\begin{pmatrix} \boldsymbol{e}_x \\ \boldsymbol{e}_y \\ \boldsymbol{e}_z \end{pmatrix} = \begin{pmatrix} \cos\theta' & \sin\theta' & 0 \\ -\sin\theta' & \cos\theta' & 0 \\ 0 & 0 & 1 \end{pmatrix} \begin{pmatrix} \boldsymbol{e}'_x \\ \boldsymbol{e}'_y \\ \boldsymbol{e}'_z \end{pmatrix} . \tag{2.3.4}$$

2.4 Other Diagnostics

The two flux rope experiment also uses other diagnostics to diagnose the plasma, which includes a microwave interferometer that measures the line-of-sight plasma density and a high-speed camera that records high-frame rate videos of the two flux ropes.

2.4.1 Microwave Interferometer

The microwave interferometer measures the line-of-sight density of the plasma within the LAPD. It is used to calibrate the density measurements of a Langmuir probe. An example of a microwave interferometer is shown in Fig. 2.8. The device is angled 45-degrees into a window made of

polytetrafluoroethylene (Teflon) which is transparent to microwaves.

The interferometer produces microwaves at frequencies of 60 GHz with the help of a Gunn diode oscillator, which are split into two components using a 10 dB directional coupler. The weaker signal is used as a reference while the stronger signal is collimated with a lens and fired into the LAPD chamber. The stronger signal passes through the plasma and is then reflected from the other end of the chamber back into the interferometer where it is mixed with the weaker reference signal.

The density of the plasma is determined from the phase difference between the two signals, which is the path difference between the weaker signal traveling in vacuum and the stronger signal traveling across the plasma. Given the dispersion relation for microwaves in a plasma, i.e.

$$\omega^2 = k^2 c^2 + \omega_{pe}^2 \ , \tag{2.4.1}$$

where k is the wavenumber of the microwaves and c is the speed of light, the phase difference $\Delta\phi$ is then

$$\Delta\phi = \frac{\omega}{c} \int_0^L \mathrm{d}L \left(1 - \sqrt{1 - \frac{\omega_{pe}^2}{\omega^2}} \right) \ , \tag{2.4.2}$$

where L is the path length across the plasma. As $w \gg \omega_{pe}$ for the case for the LAPD (i.e. $f = 60$ GHz and $f_{pe} = 12.7$ GHz), (Eq. 2.4.2) can then be simplified by expanding the square root and rearranging the equation to obtain an expression for the line-of-sight density

$$n = \frac{2\omega\Delta\phi}{L} \left(\frac{c\varepsilon_0 m_e}{e^2} \right) \ . \tag{2.4.3}$$

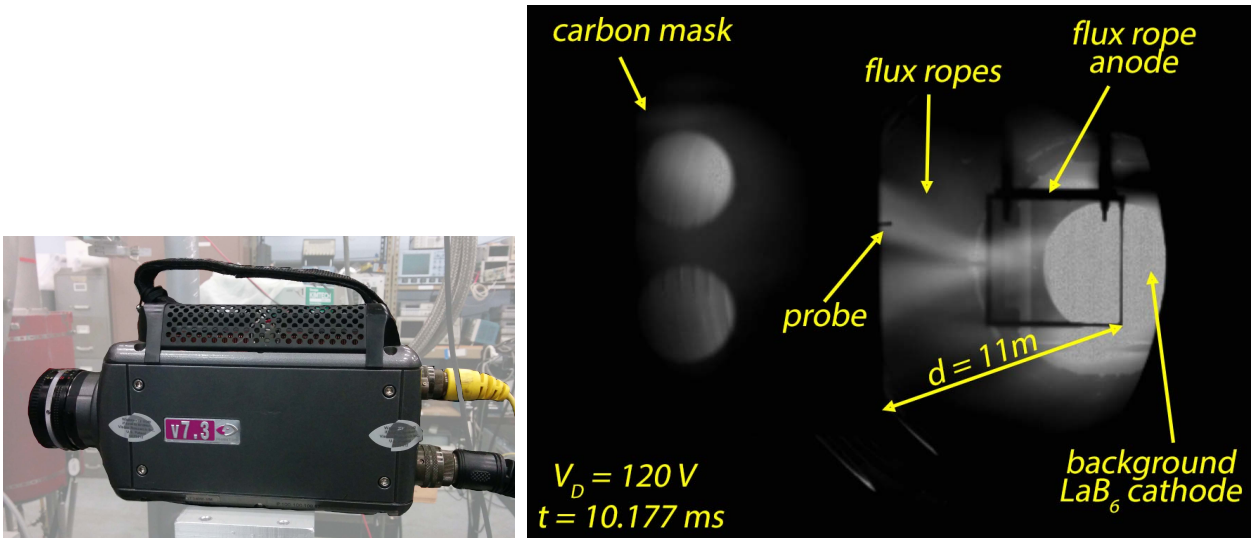

(a) (b)

Figure 2.9: (a) A high speed camera that is used to observe the motion of the flux ropes during the experiment. (b) A monochrome still frame from the high speed camera when viewed down the length of the interior of the LAPD chamber when the cathode for the flux ropes is turned on.

2.4.2 High Speed Camera

Fig. 2.9a shows a high speed camera (Vision Research Phantom v7.3) that is used to observe the flux ropes in real-time during the experiment. The camera measures the exposure level of emitted light with an CMOS sensor and outputs the data to a computer, which displays images with a 800×600 resolution. It can record videos with up to $500,000$ frames per second ($\Delta t \approx 2$ μs) under the lowest image quality setting. The camera is mounted on a jack scissor stand that allows its height and position to be adjusted.

The high speed camera is used to diagnose issues with the flux ropes before taking data. It captures footage from a single discharge cycle of the plasma and the timing of the recording is controlled by the same trigger that starts the flux rope experiment. A monochrome still frame representing the typical image observed by the high speed camera is shown in Fig. 2.9b. The view is from a glass window at the north end of the machine, down the length of the LAPD chamber. Various parts of the experimental setup are labeled showing the flux rope carbon mask, the flux

rope anode and the background LaB_6 cathode. Two flux ropes are clearly seen in the middle of the image.

2.5 Data Acquisition and Post-Processing

The LAPD has a computerized data acquisition system (DAQ) with two primary functions: the first monitors the state of the device by continuously measuring quantities such as the chamber pressure, neutral gas composition and background magnetic field. These measurements are displayed on a screen and are also collected and summarized at the end of every data run in a "machine state information" report. The second function of the DAQ is to execute a user-initiated data run, digitize the measurements made by the diagnostic probes, and then store the collected data in a hard drive.

As mentioned in Section 2.3.5, the diagnostic probes can be mounted on a probe drive which is controlled by the DAQ. The user calibrates the probe with respect to the machine center, then moves the probe head to specified points within the machine. The data collection boundaries are also specified, together with the spacing and the total number of points on each side of the plane or volume. A typical datarun for the flux rope experiment is a 41×41 plane with points spaced 0.75 cm apart (i.e. a 30 by 30 cm square). The DAQ moves the probe automatically during the datarun without requiring the attention of a user.

The signals from the probe measurements are digitized by a Struck Innovative Systeme SIS3302 8 channel digitizer with a 16-bit resolution and a sampling rate of up to 10^8 samples per second (i.e. $f = 100$ MHz). The digitizer has an input span of 4 V (i.e. ± 2 V) and signals exceeding this input range have to be attenuated in order to avoid clipping of the signal. Data to be stored by the DAQ may also be pre-processed to conserve disk space. For example, every other data point or the entire time trace may be averaged over multiple points or shots respectively by the digitizer before being recorded in the datarun file.

The measured data, together with the machine state information report, is then stored in a binary data format known as HDF5 (i.e. Hierarchical Data Format version 5). The HDF5 file format is self-defining, platform-independent and is capable of structuring large amounts of data for easy access when reading the file instead of reading the entire file. This is necessary to conserve processing memory as a single datarun on the LAPD tends to collect data on the order of a few gigabytes: a single channel collecting data from a 41×41 plane with 15 shots at each point, sampled for 14 ms with a 3.125 MHz sampling rate is about 1.1 GB.

At the end of a datarun, the HDF5 file can be read using programming languages such as Python or IDL (Interactive Data Language). Routines that interface with HDF5 are readily available in the standard library of the accompanying programming language software (e.g. `h5py` for Python). These routines slice data from anywhere within the HDF5 file and then load them into an data array which can then be read, manipulated and analyzed.

Chapter 3

Two Flux Ropes

The two flux rope experiment on the LAPD is a well-diagnosed system that has been extensively studied prior to this dissertation. Processes such as magnetic reconnection (Gekelman et al. 2010), helicity transformation (DeHaas and Gekelman 2017) and non-local Ohm's law (Gekelman et al. 2018a) have been studied and characterized by volumetric datasets of physical quantities such as the ropes' local magnetic field, plasma density n, electron temperature T_e and ion flow. These measured quantities adequately describe the geometry and time evolution of the ropes under a variety of rope conditions, which depend on factors such as the strength of the external guide field and the discharge power supplied to the ropes.

In this chapter, measurements from the two flux rope system is presented. Data from the current study is supplemented with measurements made from previous experiments (labelled `(Ref)` at the top of each figure) to provide a general understanding of the ropes that are investigated in this dissertation. Although the experimental conditions differ between each study which leads to variations in the flux rope behavior, the flux ropes generally have the same geometry (i.e. length $L = 11$ m, diameter $d = 7.6$ cm), background magnetic field ($B_0 = 330$ G) and overlapping discharge conditions (i.e. discharge voltage $V_D = 120$–160 V, rope current $I_R = 300$–700 A). Thus, the flux ropes are comparable across the different studies.

3.1 Kink Instability

3.1.1 Kruskal–Shafranov Limit

The Kruskal–Shafranov limit I_{KS} is the minimum amount of current required to induce the kink instability in a flux rope of radius a and length L. It was derived by Shafranov (1956) and Kruskal and Tuck (1958), and is expressed as

$$I_{KS} = \frac{4\pi^2 a^2 B_0}{\mu_0 L} \ , \tag{3.1.1}$$

where B_0 is the axial magnetic field and μ_0 is the vacuum permeability. For two flux ropes with $B_0 = 330$ G, $a = 3.81$ cm and $L = 1100$ cm, the value of $I_{KS} = 136.8$ A.

3.1.2 Kink Frequency & Oscillations

The flux ropes are formed when the background plasma reaches steady state and the flux rope LaB_6 cathode is turned on. The ropes are initially in axisymmetric equilibrium, but transits to a rotating, helical equilibrium as the ropes become kink unstable and the current increases past the Kruskal–Shafranov limit (Paz-Soldan et al. 2011).

This kink instability produces a global, coherent mode of oscillation in the flux ropes that can be observed in measurements such as the local magnetic field in Fig. 3.1a. In this figure, the kink instability produces oscillations in dB_x/dt between 11 ms and 15 ms which become more pronounced when integrated to give B_x. The kink frequency is then determined by performing a fast-Fourier transform (FFT) on the signal and then averaging all the signals taken at the same location. The result is plotted in Fig. 3.1b with a log-linear scale. A linear relationship below the ion cyclotron frequency ($f_{ci} = 125.7$ kHz) in a log-linear plot indicates an exponential spectra and the presence of Lorentzian pulses and deterministic chaos within the system (Maggs and Morales 2011).

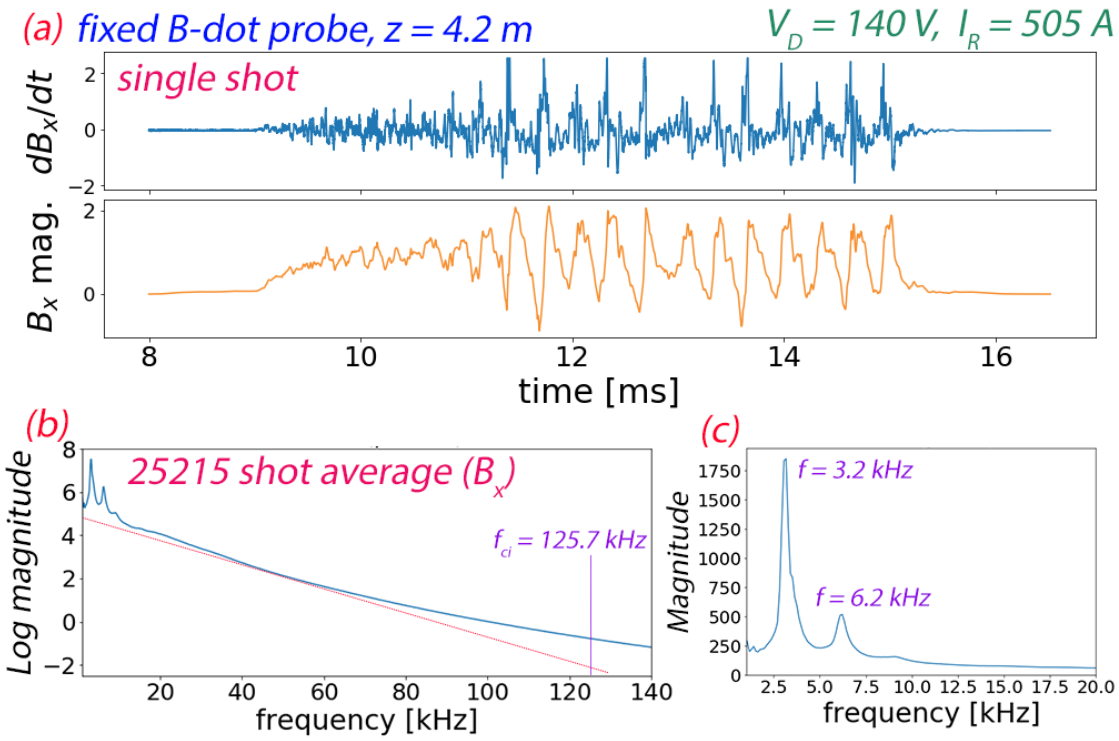

Figure 3.1: (a) A single time trace of dB_x/dt and the resulting B_x from numerical integration showing the kink oscillations that are present in the signal. (b) A log-linear plot of the average FFT from 25215 different time traces. There is an approximate linear relationship for frequencies below the ion cyclotron frequency ($f_{ci} = 125.7$ kHz). (c) A linear plot of frequencies below 20 kHz showing the two peaks due to the kink oscillation. The kink frequency of the ropes is $f = 3.2$ kHz.

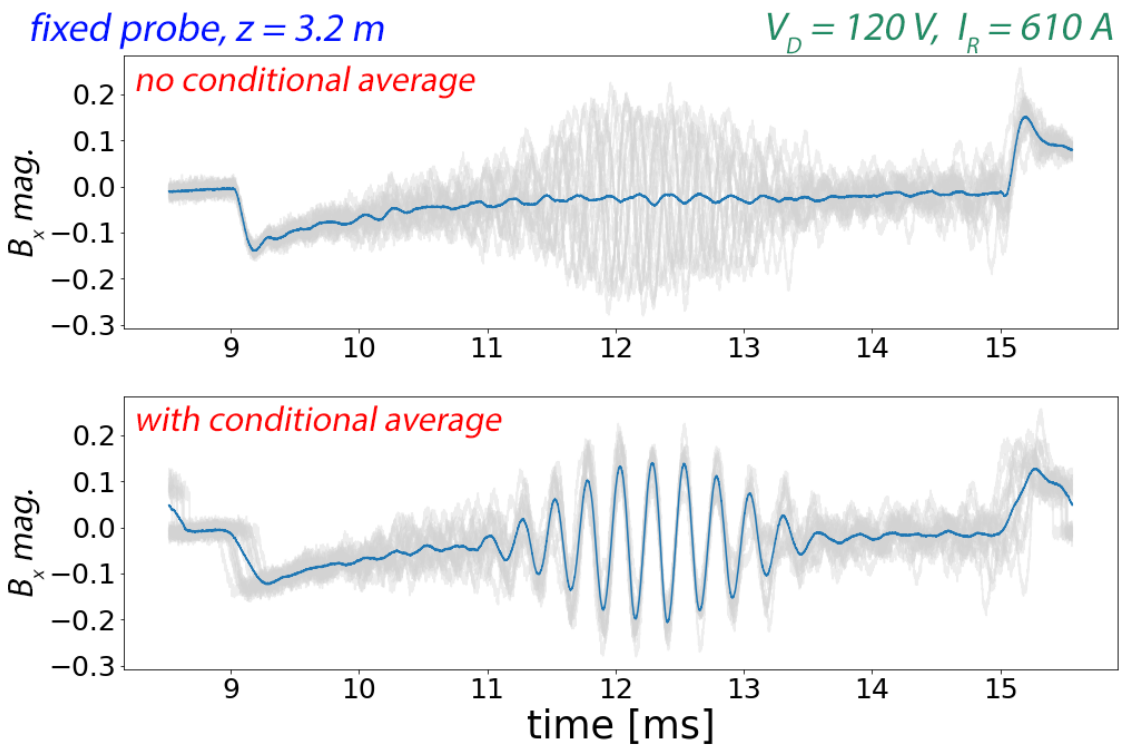

Figure 3.2: Two plots showing 15 individual time traces plotted in grey and the average plotted in blue. The top plot uses a simple average while the bottom plot shifts each time trace by a phase relative to one randomly chosen shot to perform conditional averaging.

Fig. 3.1c is a close up of the frequency peaks below 20 kHz, which shows the kink frequency of the coherent mode oscillation at $f = 3.2$ kHz. The second peak at 6.2 kHz is a harmonic. In general, the kink frequency of the two LAPD flux ropes at $B_0 = 330$ G is usually between 3 to 7 kHz.

3.2 Conditional Averaging

The phase of the flux rope's coherent mode oscillation is random and not phase-locked to the timing of the experiment. As a result, a direct averaging of all the data within the same period of time may result in the signal averaging to zero. This is shown in Fig. 3.2a where 15 time traces of B_x (in grey) are plotted together with their direct average (in blue) and the oscillations in the signal have nearly disappeared.

To avoid averaging out information contained within the kink oscillation of the ropes, the relative phase of each time trace with respect to a single reference shot has to be determined. This relative phase is then used to shift each time trace before averaging the data. This technique is known as conditional averaging and is frequently used to investigate large-scale structures in numerous plasma devices (Teliban et al. 2007; Van Compernolle and Gekelman 2012).

The relative phase of each shot is calculated with a second probe fixed in position within the LAPD such that can it observe coherent oscillations of the kink-unstable flux ropes like those shown in Fig. 3.1a. The phase is determined with respect to a randomly selected time trace on the fixed probe. This procedure requires the length of the signal containing the flux rope oscillations to be on the order of the signal's autocorrelation width (i.e. the autocorrelation time) (Stenzel and Urrutia 2000; Greiner et al. 2004; Teliban et al. 2007). This removes the influence of decorrelated signals in the calculation of the conditional average.

The cross-correlation between two discretized signals $X(t)$ and $Y(t)$ is given by

$$C_{xy}(\tau) = \sum_{t=0}^{N} \bar{X}(t+\tau) \cdot Y(t) \ , \tag{3.2.1}$$

where $\bar{X}(t)$ is the complex conjugate of $X(t)$, N is the total number of points in the signal and τ is the lag time of the signal. The overall correlation between two signals is then calculated with the cross-correlation function (also known as the Pearson's correlation coefficient)

$$r_{xy}(\tau) = \frac{C_{xy}(\tau)}{\sqrt{C_{xx}(0) \cdot C_{yy}(0)}} = \frac{\sum_{t=0}^{N} \bar{X}(t+\tau) \cdot Y(t)}{\sqrt{\left(\sum_{t=0}^{N} X^2(t)\right) \cdot \left(\sum_{t=0}^{N} Y^2(t)\right)}} \ , \tag{3.2.2}$$

where $C_{xx}(0)$ and $C_{yy}(0)$ are the autocorrelation of $X(t)$ and $Y(t)$ at $\tau = 0$ respectively. The value of r_{xy} lies between the interval of -1 (perfectly anti-correlated) and 1 (perfectly correlated), with 0 indicating no correlation between the two signals.

The time shift to be applied to each time trace is then given by the value of τ which maximizes

the value of r_{xy}. Applying the time shift τ to the time traces in Fig. 3.2a results in the signals shown in Fig. 3.2b, which recovers the coherent oscillations produced by the kink-unstable flux ropes in conditionally averaged signal.

The time shift τ can also be applied to other measurements recorded simultaneously with the fixed probe. These probes recording the measurements can be located anywhere along the LAPD as the correlation length between two probes is typically on the order of the length of the ropes (~ 11 m). This technique is also applied to the measurements presented in the following sections.

3.3 Magnetic Field & Current Density

3.3.1 xy-plane Measurements

The local magnetic fields of the two flux ropes are measured by B-dot probes (see Section 2.3.2) that move in xy-planes across the flux ropes at various z positions of the LAPD. This characterizes the three-dimensional magnetic field of the ropes within a cuboidal volume of the LAPD.

The xy-vector plots of the perpendicular magnetic field ($B_\perp$) at four z positions along the LAPD ($z = 1.28$, 2.88, 3.83 & 7.03 m) are shown in the top row of Fig. 3.3. The perpendicular current density (J_z) derived from the magnetic field vectors using Ampère's law ($\nabla \times \boldsymbol{B} = \mu_0 \boldsymbol{J}$) are shown at the bottom row. These plots correspond to $t = 12.98$ ms after the start the experiment or 3.98 ms after the flux ropes are turned on.

When the flux ropes are measured near the carbon mask at $z = 1.28$ m, they appear as two distinct, individual ropes as shown by both $B_\perp$ and J_z plots in Fig. 3.3. The J_z current is in the negative z-direction which goes into the page, towards the direction of the carbon mask. This produces a poloidal magnetic field that is overall left-handed when combined with the guide field of the LAPD.

Moving further away from the source at $z = 2.88$ m, the flux ropes begin to rotate clockwise

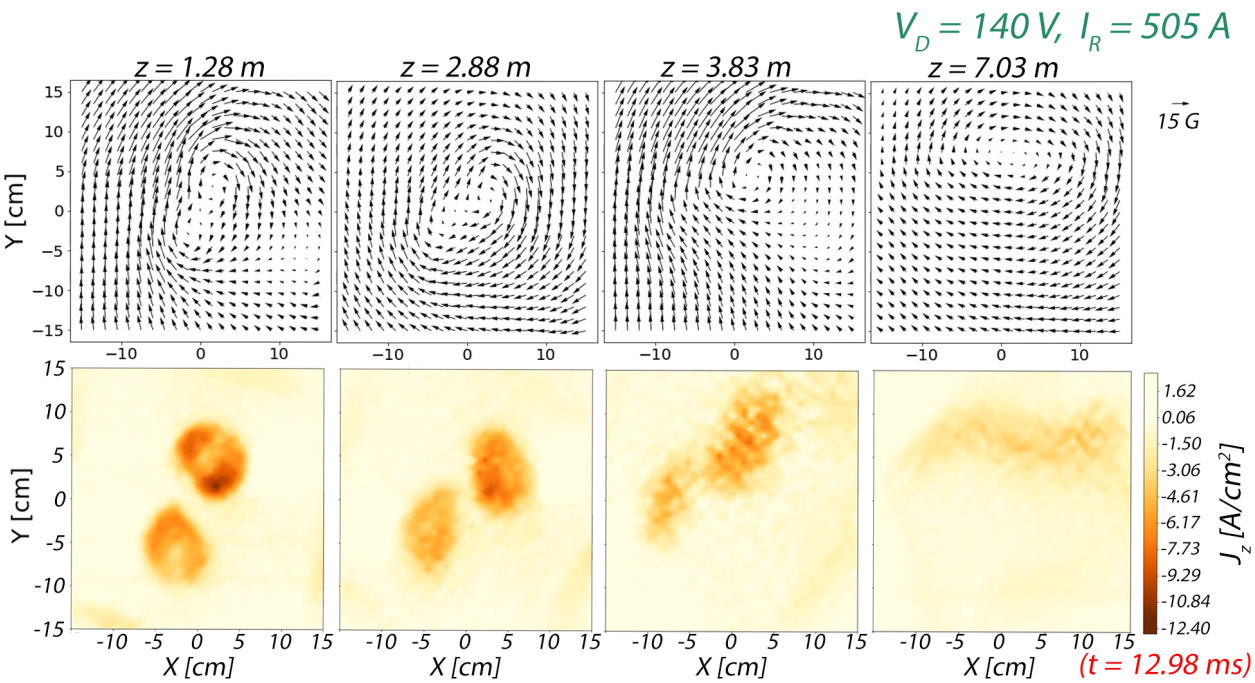

Figure 3.3: $B_\perp$ vector plots (top row) and J_z contour plots (bottom row) for the two flux ropes at various z-positions along the LAPD.

about their geometric center and stretch outwards. This is due to the mutual $\boldsymbol{J} \times \boldsymbol{B}$ forces that were induced on each rope, resulting in a twisting of field lines as the ropes rotate about each other (DeHaas and Gekelman 2017). Furthermore, the radius of rotation made by the center of each rope is greater the further away in z from the source the ropes (DeHaas et al. 2015). Magnetic reconnection becomes possible as the separation between the ropes becomes smaller and the field lines begin to touch. This is observed in J_z at $z = 3.83$ m.

Finally, at distances far away from the source of the ropes such as $z = 7.03$ m, the ropes are chaotic and merge into an elongated current structure. The peak current density J_z also decreases as the current is intertwined with the field line of the ropes and they both spread across a wider area. This was observed in earlier studies involving two reconnecting, kink-unstable flux ropes (Gekelman et al. 2014; Gekelman et al. 2016a).

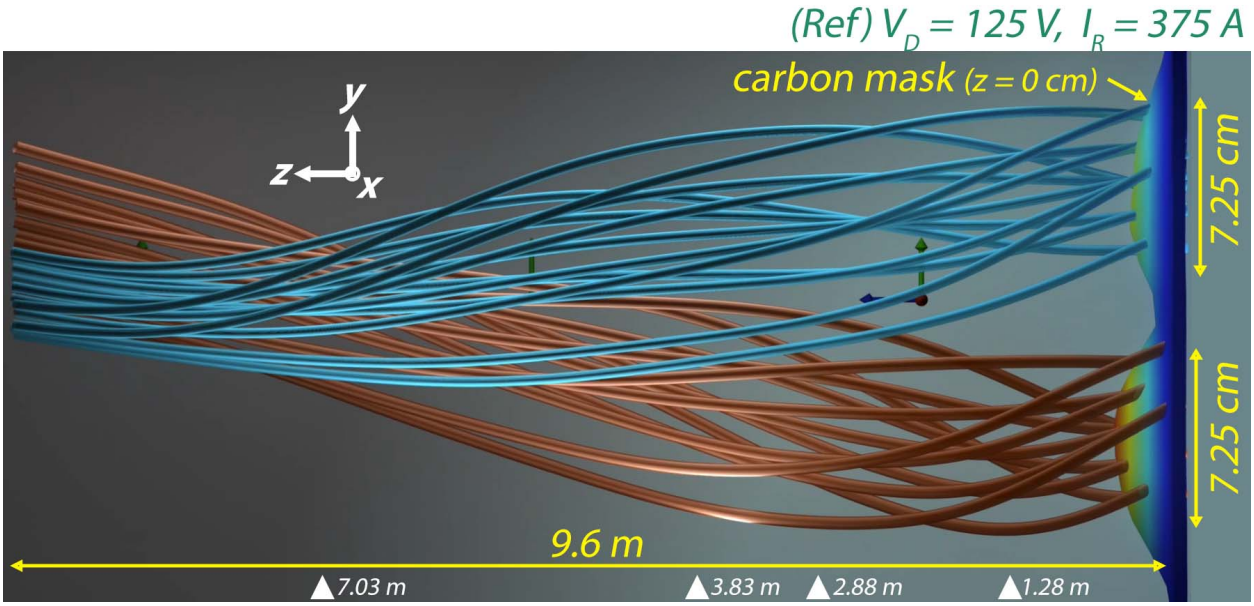

Figure 3.4: A side view of the two flux ropes showing magnetic field lines constructed with experimental data. Each field line begins from a point on the source of the ropes which follows the magnetic field vectors along the length of the machine. The dimensions are compressed such that it is 9.6 m wide but 25 cm across. The figure is a still frame from Movie S1 of the supplementary materials in Gekelman et al. (2018b), and annotations have been added to the figure.

3.3.2 Magnetic Field Lines

The side profile of the flux ropes is illustrated in Fig. 3.4 with a plot of the magnetic field lines originating from the source of the ropes (i.e. the carbon mask at $z = 0$ cm). The field lines were constructed by following the magnetic field vectors starting from points at $z = 0$ cm, and are colored differently (blue and orange) to distinguish the field lines that originate from different ropes.

It may be noted that the dimensions of the figure are compressed such that the ropes measure 9.6 m horizontally across but 25 cm wide vertically. This allows the individual field lines of the entire flux rope which writhe and twist along the length of the rope to be observed. In addition, white markers located at the bottom of the figure indicate the positions corresponding to the location of the data planes in Fig. 3.3. The geometry of the magnetic field lines at these positions in Fig. 3.4 agree very well with $B_\perp$ and J_z in Fig. 3.3. The overall left-handed rotation of the

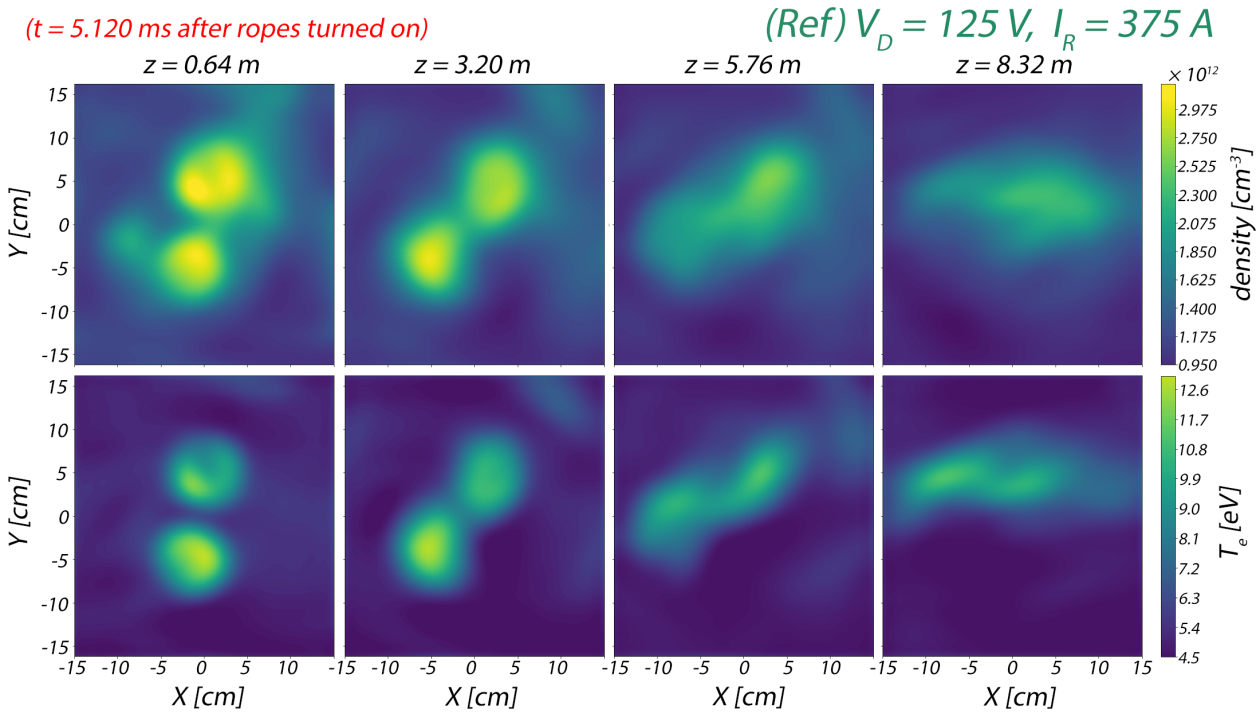

Figure 3.5: Contour plots of plasma density n (top row) and electron temperature T_e (bottom row) for the two flux ropes at various z-positions along the LAPD.

ropes about their mutual center can be observed.

3.4 Plasma Density & Electron Temperature

The plasma density n and the electron temperature T_e of the flux ropes were measured by Langmuir probes as described in Chapter 2.3.3. The top row of Fig. 3.5 are density plots while the bottom row are T_e plots for four z positions along the LAPD ($z = 0.64$, 3.20, 5.76 and 8.32 m) at $t = 5.12$ ms after the flux rope LaB_6 cathode is turned on. In this figure, the overall peak density is 3.4×10^{12} cm^{-3} and the overall peak T_e is 13 eV.

The axial development of the ropes' density and electron temperature show great similarity with the perpendicular current density J_z plotted in Fig. 3.3. This is due to the heating of the electrons by the flux rope LaB_6 cathode whose effects are correlated in the aforementioned quantities. For example, electrons energized by the cathode flow through the ropes and form the

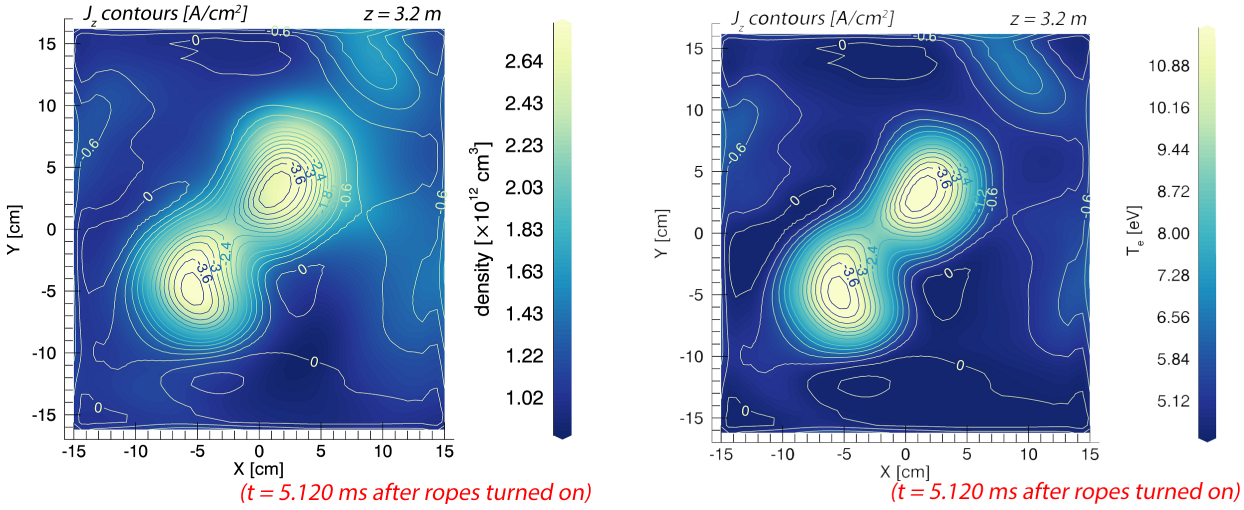

(a) Plasma density n (b) Electron temperature T_e

Figure 3.6: Colorized surface plots of the (a) plasma density n and (b) electron temperature T_e for a plane at $z = 3.2$ m. The contours of the axial current density J_z is superimposed on both plots to show that all three quantities are spatially correlated.

J_z current. This current then ionizes the neutrals required to produce the rope plasma which increases n and T_e. This effect is observed in the measurements of all three quantities as the spatial structure shows the merging of two individual ropes as the measurements are made further away from the plasma source. In addition, the peak n and T_e for each xy-plane drops along z which is similar to J_z.

The strong spatial correlation between n, T_e and J_z is further illustrated by superimposing line contours of J_z on the filled contours plots of n and T_e at $z = 3.2$ m. The result is plotted in Fig. 3.6. The J_z contours are seen to fit both n and T_e profiles well. The maximum J_z in the plot (4 A/cm^2) is consistent with the measured discharge current ($I = 375$ A) per unit area across the ropes.

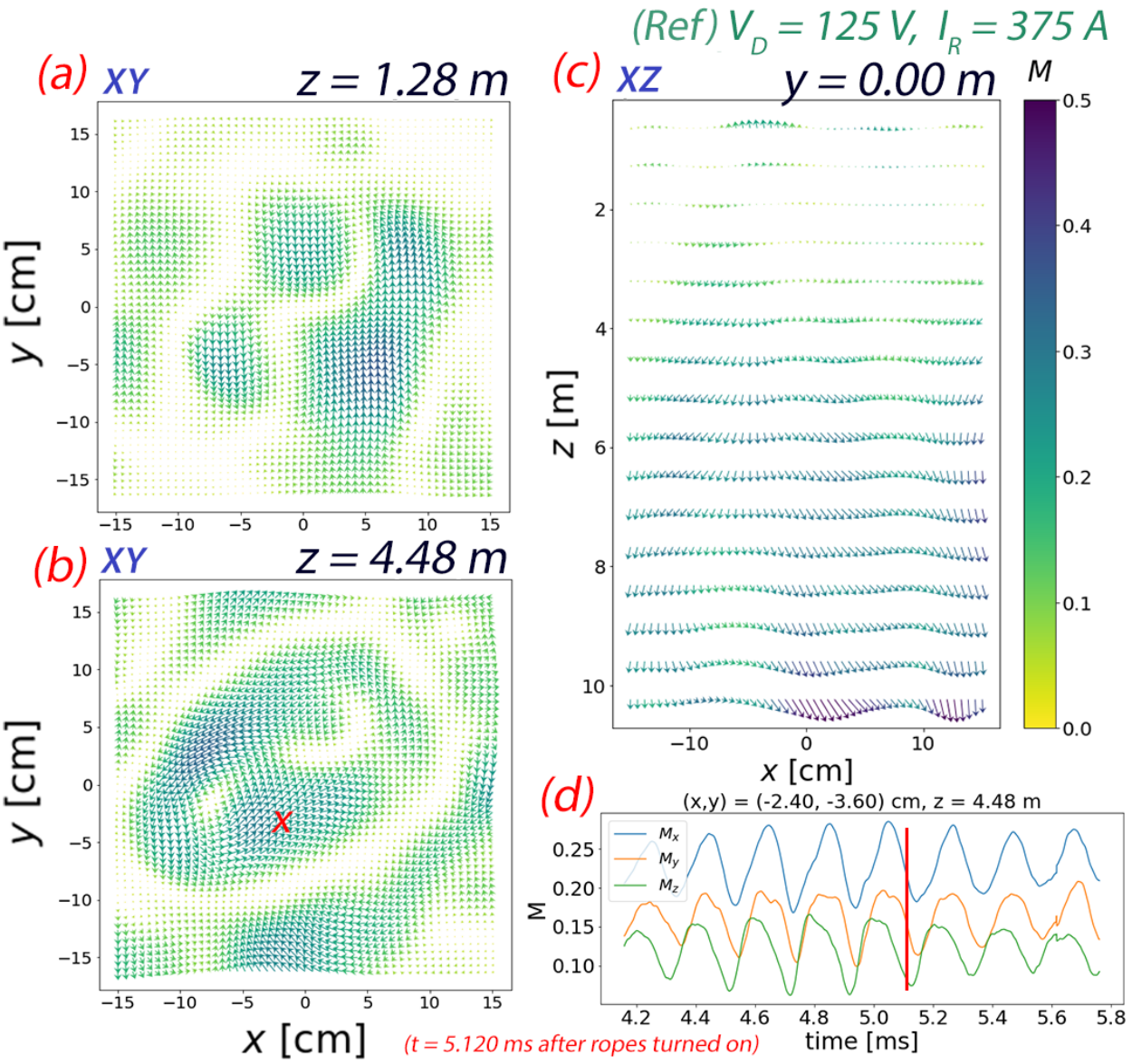

Figure 3.7: (a, b) The vector plot of the perpendicular Mach number for two different z-positions along the LAPD ($z = 1.28$ and 4.48 m). (c) The xz-plane vector plot of the Mach number showing the flow across the length of the machine. All three vector plots use the same color scale. (d) The three components of the Mach number (M_x, M_y M_z) plotted as a function of time for the position marked with a cross in (b). The red line represents the time coordinate of the other three vector plots shown in the figure ($t = 5.120$ ms).

3.5 Mach Number & Ion Flow

The ion flow of the flux ropes is characterized by the Mach number M and is measured by the Mach probe as described in Chapter 2.3.4. Fig. 3.7 shows three quiver plots of the Mach number across different cross-sections of the LAPD. Fig. 3.7a and Fig. 3.7b are xy-planes across the flux ropes at $z = 1.28$ and 4.48 m respectively. The length and color of the arrows are determined by the perpendicular Mach number $\sqrt{M_x^2 + M_y^2}$. The shape of the ropes can be observed from the ion flow as they circulate around the edges in the direction of $\boldsymbol{E} \times \boldsymbol{B}$. At locations outside and far away from the rope edges, the flow of the ions are in the opposite direction due to reverse currents that are present in the background.

Fig. 3.7c shows an xz-plane (top-down view) of the Mach number across the center of the LAPD ($y = 0$ m). The length and color of the arrows in this plot are colored by xz components of the Mach number, $\sqrt{M_x^2 + M_z^2}$. As the density n and electron temperature T_e are large near the source of the ropes, a pressure gradient is established along z which creates a flow away from the source of the ropes. The Mach number thus increases the further away it is from the source as seen in Fig. 3.7c. The peak Mach number has a value of 0.54 at $z = 10.24$ m.

Finally, all three components of the Mach number are plotted in Fig. 3.7d for a single point located at $(x, y, z) = (-2.40, -3.60, 448)$ cm. The Mach numbers are shown to oscillate at the kink frequency of approximately 5 kHz.

Chapter 4

Ion Retarding Field Energy Analyzer

The energy distribution of the ions in the flux ropes was investigated using a retarding field energy analyzer (i.e. ion energy analyzer) that is constructed specifically for deployment on the LAPD. The ion energy analyzer is designed as a diagnostic probe that measures the energies of incoming ions by selectively screening ions based on their initial velocities at the point of entry. This is achieved with a series of electrically biased grids that set up electric fields to repel ions within the interior of the ion energy analyzer. Ions that have enough energy to move past the grids are collected. The collected current I is then plotted a function of the retarding grid potential V to obtain an I-V curve which is differentiated to obtain the ion distribution function $f(E)$.

4.1 Principle of Operation

The basic operation of a four-grid ion energy analyzer is illustrated in Fig. 4.1. The setup contains four partially transparent meshed grids electrically isolated and arranged in succession such that charged particles entering the ion energy analyzer can either be transmitted or repelled depending on the bias potential that is applied on each grid.

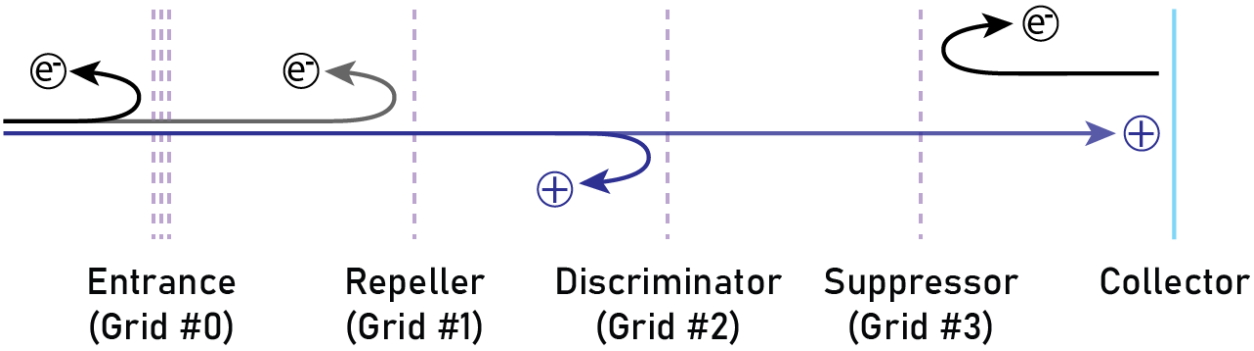

Figure 4.1: A diagram illustrating the basic operation of a four-grid retarding field energy analyzer for ions. The discriminator grid repels ions while the entrance, repeller and suppressor grid repels electrons.

Entrance grid (Grid #0) The entrance grid is the interface between the plasma and the interior of the ion energy analyzer. It is a grid mesh with multiple openings that are appropriately sized to allow the transmission of an adequate amount of particles into the energy analyzer, but is sufficiently small that the sheath around the edges of each opening does not get perturbed (Pitts et al. 2003). This ensures that the ions' trajectories are not deflected as it passes through the sheath in front of the grid and reduce the accuracy of the measurement (Pitts 1996; Brunner et al. 2013b). This requires the width of the openings to be on the order of the Debye length

$$\lambda_D = \sqrt{\frac{\varepsilon_0 k T_e}{n_0 e^2}} \ ,$$

where ε_0 is the dielectric constant, k is the Boltzmann constant, T_e is the electron temperature, n_0 is the plasma density and e is the elementary charge.

Overall, the sheath protects the entrance grid from degradation due to exposure to the plasma whilst keeping the external plasma isolated from perturbations by the interior electric fields of the ion energy analyzer. In return, the entrance grid protects the interior of the energy analyzer by attenuating the power density of the incoming ions, which prevents the inner grids from overheating and warping (Molvik 1981).

Repeller grid (Grid #1) The next grid of the ion energy analyzer is the repeller grid, which is biased negatively to deny electrons from entering the energy analyzer. It prevents the growth of a parasitic electron current as the adjacent discriminator grid is increasingly positively biased to repel incoming ions (Böhm and Perrin 1993). The negative bias also maximizes the ion current collected by the energy analyzer (Ingram and Braithwaite 1988).

The appropriate bias on the repeller grid is determined theoretically by considering the energy distribution of the incoming electrons. This assumes the electrons follow a one-dimensional Gaussian distribution

$$f(v) = \sqrt{\frac{2m}{\pi k T_e}} \exp\left(-\frac{mv^2}{2kT_e}\right) \ , \tag{4.1.1}$$

where m is the electron mass and the function is normalized by considering electrons that only move towards the energy analyzer, i.e.

$$\int_0^\infty \mathrm{d}v \, f(v) = 1 \ .$$

From the conservation of energy, electrons that approach the grid biased with a potential V_1 would need to have velocities $v \geq \sqrt{2eV_1/m}$ in order to move past the grid. The velocity v is assumed positive (i.e. $v \geq 0$). The fraction of repelled electrons p is then given by

$$p \equiv p(V_1) = \int_0^{\sqrt{2eV_1/m}} \mathrm{d}v \, f(v),$$

where p varies between 0 and 1. Substituting $f(v)$ from (Eq. 4.1.1) and with a change of variables $y = \sqrt{\frac{m}{2kT_e}} v$, this gives

$$p = \frac{2}{\sqrt{\pi}} \int_0^{\sqrt{eV_1/kT_e}} \mathrm{d}y \, e^{-y^2} \ = \mathrm{erf}\left(\sqrt{\frac{eV_1}{kT_e}}\right) \ , \tag{4.1.2}$$

where the error function is defined as

$$\mathrm{erf}(z) = \frac{2}{\sqrt{\pi}} \int_0^z \mathrm{d}t\, e^{-t^2} \ .$$

Therefore, the required bias potential V_1 is obtained by taking the inverse of (Eq. 4.1.2), which gives

$$\boxed{V_1 = \left(\mathrm{erf}^{-1}(p)\right)^2 \cdot \frac{kT_e}{e}} \ .$$

This means that repelling 99.99% of the incoming electrons from a $T_e = 7$ eV plasma will require a bias potential of $V_1 = -53$ V with respect to the energy analyzer ground.

Discriminator grid (Grid #2) The discriminator grid is a principle component of the ion energy analyzer and its bias is varied to limit the amount of ion current that reaches the collector. The bias starts at a negative potential to saturate the probe with ion current and is slowly increased linearly until the collected current drops to zero. The collected current is then plotted as a function of discriminator grid potential to obtain an I-V curve of the plasma, which can be used to determine the ion energy and temperature.

Suppressor grid (Grid #3) The suppressor grid prevents the escape of secondary electrons emitted from the surface of the collector due to the bombardment of energetic ions that make it past the discriminator grid. This is a problem when dealing with high energy ions as the bombarded electrons that escape from the collector create a net positive collector current which results in a positive offset in the measured I-V curve (Böhm and Perrin 1993).

A solution to mitigate this problem is to bias the suppressor grid negatively with respect to the collector so that the escaped electrons are returned to the collector and its net current contribution is zero. Böhm and Perrin (1993) suggested that the applied bias potential depends

on two factors: the ionization energy E_i of the incoming ion and the work function ϕ of the collector material. Then, the potential difference between the suppressor grid and the collector needs to be greater than $E_i - 2\phi$ for most of the secondary electrons to be repelled, which is the difference between the energy released from ion neutralization and the amount of energy required to liberate two surface electrons (one for the recombination and the other that escapes). This would be the maximum kinetic energy possessed by a single escaping electron and it is estimated to be 16 eV for a helium plasma ($E_i = 24.6$ eV for He I) (Lide 1993) and a collector made of tantalum ($\phi \approx 4.0$ eV) (Fiske 1942).

A second condition for the suppressor grid is that its potential has to be lower than the repeller grid. This prevents some of the energetic electrons that make it past the repeller grid from reaching the collector (Brunner et al. 2013b). The suppressor grid is thus expected to have the lowest potential bias of all the grids within the ion energy analyzer.

Collector The collector is solid piece of metal at the back of the ion energy analyzer which collects ions and is typically maintained at a constant negative potential with respect to ground in order to repel electrons. Together with the four grids as mentioned above, these form the backbone of the ion energy analyzer.

4.2 Theory of Operation

4.2.1 The I-V Curve

The current collected by the ion energy analyzer I is plotted as a function of the discriminator grid potential V to obtain a current-voltage characteristic or an I-V curve of the plasma. The collector current depends on the plasma potential V_p at the entrance of the energy analyzer. When $V \leq V_p$, the ions are not impeded by the electric field set up by discriminator grid and the probe saturates with ion current I_0. However, when $V \geq V_p$, ions with energies smaller than

$e(V - V_p)$ are repelled by the discriminator grid and the population of ions that reach the collector start to decrease.

For a one-dimensional Maxwellian distribution of ions, the collector current is written as

$$I = \begin{cases} I_0 & \text{for } V \leq V_p \ , \\ I_0 \exp\left(-\dfrac{e(V - V_p)}{kT_i}\right) & \text{for } V \geq V_p \ , \end{cases} \tag{4.2.1}$$

where V_p is measured with respect to the probe ground (Nedzelskiy et al. 2006). The ion temperature T_i is then obtained from the slope of the exponential.

However, in the case of non-Maxwellian distributions of ions, the collector current I for $V \geq V_p$ is not an exponential but given by the equation

$$I = ZeA \int_{v_{\text{min}}}^{\infty} \mathrm{d}v \ \ v f(v) \ , \tag{4.2.2}$$

where Z is the charge of the ion species, A is the effective probe area, v_{min} is the minimum velocity required of the ions to reach the collector and $f(v)$ is the distribution function of the ions. The ion temperature is then determined from the moments of the ion velocity distribution function (Fitzpatrick 2014; Salewski et al. 2018).

The general distribution function $f(\boldsymbol{r}, \boldsymbol{v})$ has six dimensions in Cartesian space that depend on the ions' position $\boldsymbol{r}$ and velocity $\boldsymbol{v}$ respectively. However, homogeneity of the velocities is usually assumed which allows the spatial dependence on $\boldsymbol{r}$ to be removed (Böhm and Perrin 1993). Then, for the distribution function that depends on the three-dimensional velocity $\boldsymbol{v}$, the density n is defined by the zeroth moment distribution function

$$n \equiv \int_{-\infty}^{\infty} \mathrm{d}\boldsymbol{v} \, f(\boldsymbol{v}) \ , \tag{4.2.3}$$

and the pressure tensor $\boldsymbol{P}$ from the second-order moment

$$\boldsymbol{P} \equiv m \int_{-\infty}^{\infty} \mathrm{d}\boldsymbol{v}\, \boldsymbol{v}\boldsymbol{v} f(\boldsymbol{v}) \ , \tag{4.2.4}$$

where $\boldsymbol{v}\boldsymbol{v}$ is the tensor product of the velocity with itself.

If the off-diagonal terms are zero and the xy-plane is rotationally symmetric, then $p_{xx} = p_{yy} \equiv p_\perp$ and the pressure tensor $\boldsymbol{P}$ is

$$\boldsymbol{P} = \begin{pmatrix} p_\perp & 0 & 0 \\ 0 & p_\perp & 0 \\ 0 & 0 & p_\parallel \end{pmatrix} \ , \tag{4.2.5}$$

where $p_\perp$ and $p_\parallel$ are the pressure components across and along the magnetic field respectively. The trace of $\boldsymbol{P}$ then gives the scalar pressure

$$p = \frac{\mathrm{Tr}(\boldsymbol{P})}{3} = \frac{2p_\perp + p_\parallel}{3} \ .$$

Finally, using $p = nkT$, the temperature in the perpendicular and parallel directions are respectively defined as

$$kT_\perp = \frac{p_\perp}{n} \qquad \text{and} \qquad kT_\parallel = \frac{p_\parallel}{n} \ , \tag{4.2.6}$$

and therefore the average ion temperature T_i is given by

$$kT_i = \frac{p}{n} = \frac{k(2T_\perp + T_\parallel)}{3} \ . \tag{4.2.7}$$

This is sometimes referred to as the *ion kinetic temperature* (Valsaque et al. 2002; Fitzpatrick 2014; Salewski et al. 2018). Reducing this equation to a one-dimensional case, the pressure

tensor simplifies (i.e. $\boldsymbol{vv} \rightarrow v^2$) and the ion temperature is

$$kT_i = \frac{m}{n} \int_{-\infty}^{\infty} \mathrm{d}v \, v^2 f(v) \equiv m \left\langle v^2 \right\rangle \ . \tag{4.2.8}$$

Thus, T_i can be determined once the distribution function $f(v)$ is known. This can be obtained from (Eq. 4.2.2) by differentiating the collected current I with respect to V.

4.2.2 The Ion Distribution Function $f(E)$

The design of the ion energy analyzer is such that it only discriminates ions moving along the direction normal to the grids. Therefore, measurements of the distribution function are directionally biased and effectively one-dimensional. A plot of the collector current I as a function of the discriminator grid potential V produces the one-dimensional distribution function $f(V)$. However, $f(V)$ is a function of the discriminator grid bias V, which does not explicitly depend on the ion velocity v. Thus, the relationship between the two variables have to be reconciled.

First, consider the relationship between the ion energy E and its velocity v which is

$$E = \frac{1}{2} m v^2, \tag{4.2.9}$$

where m is the mass of the ion. Then, the minimum kinetic energy permitted by the discriminator grid bias V is given by

$$e(V - V_p) = \frac{1}{2} m v_{\mathsf{min}}^2 \qquad \text{for } V \geq V_p \ , \tag{4.2.10}$$

where v_{min} is the minimum permitted velocity through the ion energy analyzer. With a change of

variables to E and by substituting (Eq. 4.2.10) into (Eq. 4.2.2), the collector current I becomes

$$I = \frac{ZeA}{m} \int_{e(V-V_p)}^{\infty} \mathrm{d}E \; f(E) \; . \tag{4.2.11}$$

In this equation, V only changes the lower limit of integration. The distribution function $f(E)$ may then be obtained by differentiating the above equation with respect to V using the Leibniz integral rule

$$\frac{d}{dV}\left(\int_{a(V)}^{b} \mathrm{d}E \, f(E)\right) = f(E=b) \cdot \frac{db}{dV} - f(E=a(V)) \cdot \frac{d(a(V))}{dV} + \int_{a(V)}^{b} \mathrm{d}E \, \frac{\partial f(E)}{\partial V} \; , \tag{4.2.12}$$

where only the second term on the right is non-zero. This results in

$$\frac{dI}{dV} = -\frac{Ze^2A}{m} f(E) \qquad \Rightarrow \qquad \boxed{f(E) = -\frac{m}{Ze^2A}\frac{dI}{dV}} \; . \tag{4.2.13}$$

The distribution function $f(E)$ is thus proportional to $-dI/dV$ and is only valid for $V \geq V_p$ (Eq. 4.2.10). It may be noted that this proportionality is only valid in one-dimension as an energy analyzer constructed to measure $f(E)$ in three dimensions (Stenzel et al. 1983) will have the form

$$f(E) \propto -\frac{1}{V}\frac{dI}{dV} \; .$$

4.2.3 Constructing $f(E)$ and the Average Energy $\langle 2E \rangle$

Although the $f(v)$ integrals (Eq. 4.2.3) and (Eq. 4.2.4) contain limits from $-\infty$ to ∞, the ion energy analyzer can only measure the velocity of the ions along the direction it is facing where $v \geq 0$. Thus, the $f(v)$ integrals requires two measurements from the ion energy analyzer facing

opposite directions along the same axis, i.e.

$$\int_{-\infty}^{\infty} \mathrm{d}v\, f(v) \ldots \rightarrow \int_{0}^{\infty} \mathrm{d}v_{+}\, f(v_{+}) \ldots + \int_{0}^{\infty} \mathrm{d}v_{-}\, f(v_{-}) \ldots \ ,$$

where the $+/-$ subscripts indicate a measurement in the positive or negative direction along the same axis. These integrals require a change of variables to E and thus using (Eq. 4.2.9), the $\langle v^2 \rangle$ integral yields

$$\langle v^2 \rangle = \frac{1}{n} \frac{\sqrt{2}}{m^{3/2}} \left(\int_{0}^{\infty} \mathrm{d}E_{+}\, \sqrt{E_{+}} \cdot f(E_{+}) + \int_{0}^{\infty} \mathrm{d}E_{-}\, \sqrt{E_{-}} \cdot f(E_{-}) \right) \ , \tag{4.2.14}$$

and likewise for the density n,

$$n = \frac{1}{\sqrt{2m}} \left(\int_{0}^{\infty} \mathrm{d}E_{+}\, \frac{1}{\sqrt{E_{+}}} \cdot f(E_{+}) + \int_{0}^{\infty} \mathrm{d}E_{-}\, \frac{1}{\sqrt{E_{-}}} \cdot f(E_{-}) \right) \ . \tag{4.2.15}$$

The coefficients of (Eq. 4.2.14) and (Eq. 4.2.15) can be rearranged such that the integrals simplify to obtain an expression for the average energy, i.e.

$$\langle E \rangle = \frac{m \langle v^2 \rangle}{2} = \frac{1}{n^*} \left(\int_{0}^{\infty} \mathrm{d}E_{+}\, \sqrt{E_{+}} \cdot f(E_{+}) + \int_{0}^{\infty} \mathrm{d}E_{-}\, \sqrt{E_{-}} \cdot f(E_{-}) \right) \ , \tag{4.2.16}$$

with

$$n^* = \int_{0}^{\infty} \mathrm{d}E_{+}\, \frac{1}{\sqrt{E_{+}}} \cdot f(E_{+}) + \int_{0}^{\infty} \mathrm{d}E_{-}\, \frac{1}{\sqrt{E_{-}}} \cdot f(E_{-}) \ . \tag{4.2.17}$$

Then, using the relationship between $\langle v^2 \rangle$ and $\langle E \rangle$ in (Eq. 4.2.16), (Eq. 4.2.8) suggests that the ion temperature is related to the average energy as

$$kT_i = m \langle v^2 \rangle = 2 \langle E \rangle \equiv \langle 2E \rangle \ , \tag{4.2.18}$$

which holds for a general, non-Maxwellian $f(v)$. The factor of 2 is necessary because in the limiting case of a Maxwellian $f(v)$ centered at $v = 0$, the value of kT_i represents the Maxwellian temperature of the distribution.

Although the expression $\langle 2E \rangle$ is equivalent to the ion kinetic temperature, it will be shown in Chapter 5 that the distribution function contains a beam and the term 'kinetic temperature' may be confusing to readers when describing the overall energy state of the ions with a drifting beam component. As such, the term 'average energy' will be used to refer to the expression $\langle 2E \rangle$ for the rest of the dissertation.

4.3 Probe Design

The construct of the ion energy analyzer as an LAPD diagnostic is constrained by the parameters of the flux rope experiment and the infrastructure of the LAPD. Similar to the probes described in Chapter 2.3, the probe head containing the grids and collector is attached to the probe shaft, which is a 1.3 m long, 0.95 cm ($3/8$ inch) diameter insulated stainless steel tube. The probe shaft allows the probe to maintain vacuum while inserted into the LAPD and its insulation isolates the probe from electrical ground.

The probe enters the LAPD through a 40 mm diameter vacuum port which places a restriction on the maximum size of the probe head. In addition, the probe head has to be as small as possible to avoid disturbing the plasma while withstanding the heat flux produced by two LaB_6 cathodes in a vacuum environment where heat conduction is poor. The steady state temperature within the LAPD is about $300°$C. This means that the ion energy analyzer has to be made of vacuum compatible materials that are also relatively heat-resistant to protect the grids and the collector.

Fig. 4.2 shows the design of the ion energy analyzer in an exploded-view computer-aided design (CAD) drawing. The individual components that comprise the probe head of the ion energy analyzer are shown. This design is the result of six iterations of prototyping and testing

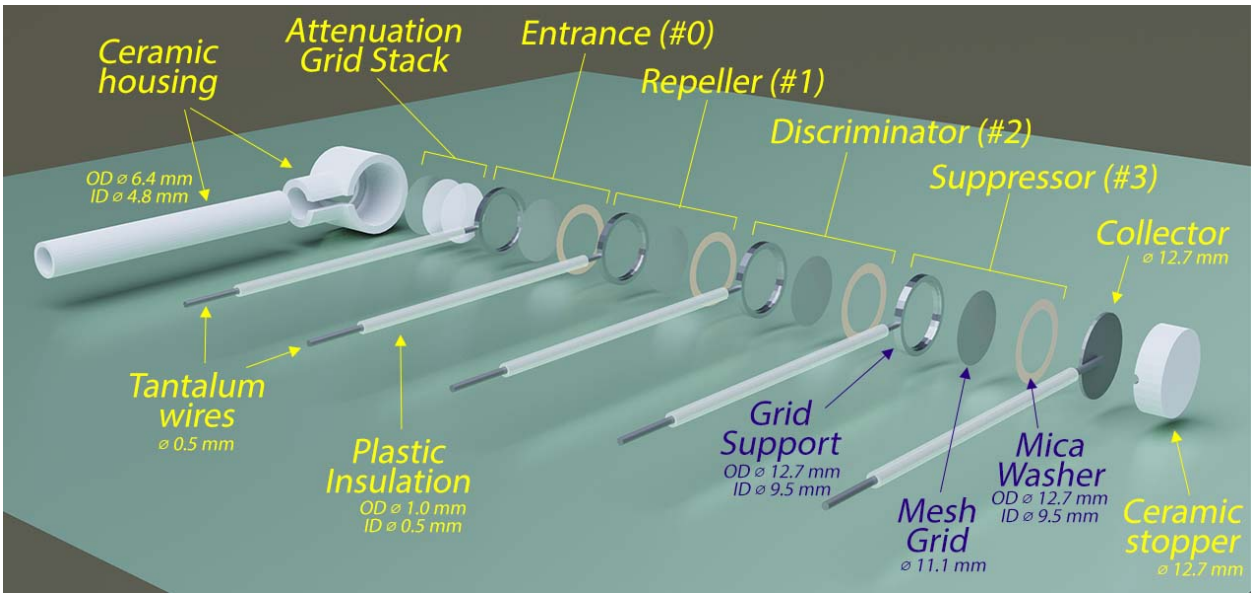

Figure 4.2: An exploded-view CAD drawing of the ion energy analyzer probe head showing individual components such as the ceramic housing, mesh grids, insulators and wires. Each grid has a set of identical components (grid support, mesh grid, mica washer, tantalum wire & plastic insulation) and all components are modeled to scale. The diameters of specific components are indicated in the drawing.

for more than 12 months to produce a working probe that could satisfy the aforementioned constraints and be successfully deployed on the LAPD. The data measured by the probe will be discussed in Chapter 5. In the following sections, the design process for each component of the ion energy analyzer is described.

4.3.1 Ceramic Housing

The ceramic housing of the probe is a protective shell constructed with tubes of various diameters made of nonporous alumina ceramic (melting point $\sim 1690°$C) that is used to shield the inner components of the probe from the heat flux of the plasma. Alumina ceramic has a very low thermal expansion coefficient (Brunner et al. 2013b), which ensures that the probe does not warp in the hot environment of the LAPD.

Fig. 4.3a and Fig. 4.3b shows the front and back of the ceramic housing respectively. The largest tube of ceramic housing accommodates circular electrodes with diameters of approximately

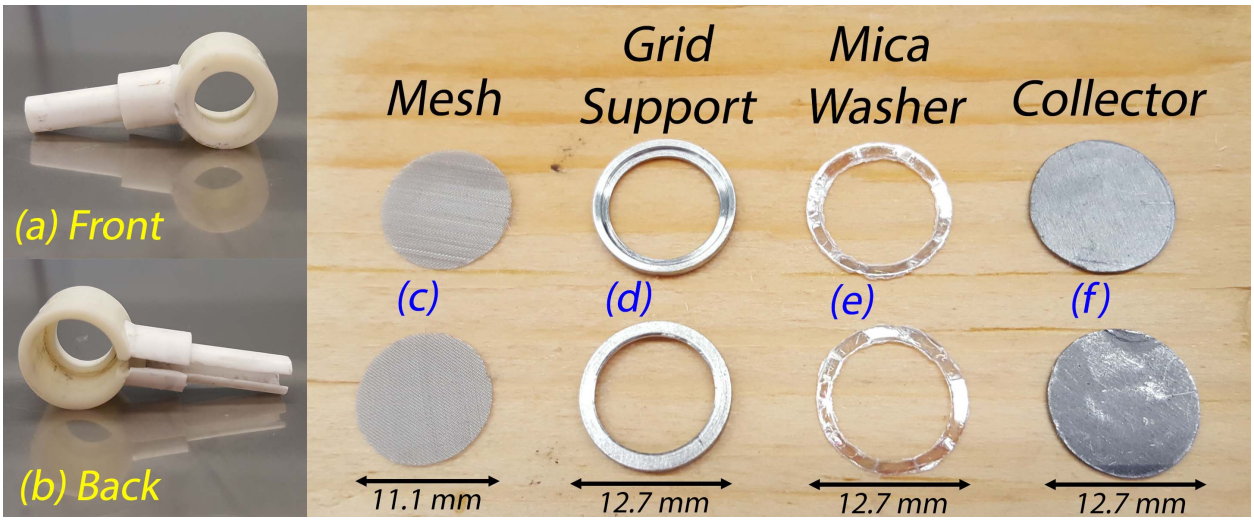

Figure 4.3: The individual components of the RFEA are shown. (a) and (b) are respectively the front and back of the ceramic housing. (c) are stainless steel grid mesh with 325 lines per inch (opening size 43.2 μm). (d) are grid supports for the stainless steel mesh. The top row shows a groove cut into the support which fits the mesh grid. (e) are mica washers, while (f) are tantalum disks for the collector.

12.7 mm ($1/2$ inch) with a height of up to 15 mm. The size of the probe, which is determined by the outer diameter of the tube, is 15.9 mm ($5/8$ inch). A short piece of ceramic 1 mm long and an inner diameter of 9.52 mm ($3/8$ inch) was then epoxied onto one end of the tube, creating a catch for the grid stack to prevent it from falling out. The effective area of the probe is the inner diameter of the ceramic catch.

The side of the ceramic tube is T-joint to a smaller two-layered ceramic tube that has an inner diameter of 4.78 mm (0.188 inch) and an outer diameter of 9.52 mm ($3/8$ inch). The tube serves as protection for the joint between the electrodes and wires after they have been connected. A 2 mm groove cut along the back of the ceramic housing is used to lower the connected electrodes into the probe head. The groove is shown in Fig. 4.3b .

4.3.2 Electrodes & Grid Stack

Although the ceramic housing shields the grids and collector electrodes from most of the heat flux of the plasma, the electrodes may still be heated by the plasma and get hot. Thus, the electrodes

have to be made of alloys or refractory metals that have high melting points, such as type 304 stainless steel for the mesh grids (melting point $\sim 1400°$C) and tantalum for the collector and wires (melting point $\sim 3017°$C).

Grids The grids are constructed from square-mesh sheets of type 304 stainless steel which are 71.1 μm thick. These meshes have a wire diameter of 35.6 μm with 325 lines per inch, creating an opening size of 43.2 μm and an mesh transparency of 30%. The grids were cut by hole punching 11.1 mm ($7/16$ inch) diameter circular holes in the mesh sheet. Some of the mesh grids are shown in Fig. 4.3c.

For reference, the Debye length λ_D is approximately 20 μm for 7 eV electrons in a 10^{12} cm^{-3} density plasma. This makes the opening size approximately two times λ_D, which is borderline acceptable for a sheath layer to be formed across the entrance grid openings. In addition, λ_D is smaller for higher plasma densities and lower electron temperatures. Thus, a smaller opening size is much preferable for the entrance grid.

The reduction in the opening size was achieved by stacking three mesh grids together in front of the entrance grid, with random angular orientations such that the interweaving of the grids produces smaller grid size openings. The stacking of the grids also attenuates the density of the plasma, as the use of multiple grids achieves an effective transmission that is equal to the product of the individual grid transparencies for ions with energies less than 100 eV (Van De Ven et al. 2018). The resulting transmission of the entrance grid is thus less than 1%.

As an aside, the upper limit to the opening width is 2 electron gyroradii ($2\rho_e$) as it ensures that very low density plasmas can pass through the entrance grid (Molvik 1981). This is automatically achieved when the opening width is on the order of the Debye length since $\lambda_D < \rho_e = 191$ μm for $T_e = 7$ eV electrons and a $B_0 = 330$ G magnetic field.

Grid supports It is difficult to attach a wire directly onto a mesh grid using solder or spot-welding due to the thinness and the delicateness of the wire mesh. Even then, a successful metallic joint tends to create a bump at the point of connection on the grid such that the grids would misalign when stacked on top of each other. Thus, grid supports are used to hold the grids and the wires are directly spot-welded onto the grid support. This allows the grid supports to be stacked in a cylinder within the ceramic housing without misaligning or damaging the grids.

Fig. 4.3d shows the front and back of a grid support used in the ion energy analyzer. It is made from a 1.3 mm thick stainless steel washer that was machined to have an outer diameter of 12.7 mm ($1/2$ inch) and an inner diameter of 9.52 mm ($3/8$ inch). A small circular groove 1 mm deep and 11.1 mm in diameter was cut within the inner diameter on one side of the washer to allow a circular mesh grid to fit while it remains flushed with the top surface.

Mica washers The electrodes of the ion energy analyzer are electrically insulated from each other using washers made from mica (melting point $700°$C), a silicate material with excellent electrical and thermal insulating properties at high temperatures. It is relatively inert and does not outgas (Böhm and Perrin 1993), which makes it suitable for operating under the low-pressure vacuum environment of the LAPD. In addition, mica can be cleaved into thin sheets (up to 25 μm without crumbling) while retaining its ability to prevent leakage currents from passing through it (Brunner et al. 2013b). This makes mica an ideal insulator for electrically isolating the grids and keeping the grid separation small.

Fig. 4.3e shows mica washers made from mica sheets approximately 50 to 100 μm thick. Each washer is created by making circular cuts centered at the same location twice: the first cut creates a disk with a diameter of 12.7 mm ($1/2$ inch), and the second cut creates a hole with a diameter of 9.52 mm ($3/8$ inch). This process has to be repeated multiple times to produce washers with a consistent radial thickness and without large cracks that usually run through damaged washers.

The thickness of the mica washers and the grid support determine the spacing between the

electrodes (~ 1.4 mm), which is used in the calculation of the space charge limited current. This is the maximum current permitted between the grids of the ion energy analyzer due to the build up of space charge that repels ions regardless of the applied potentials on the electrodes (Pitts et al. 2003). The details are discussed in Chapter 4.4.1. The grid spacing was found to be acceptable for the LAPD two flux rope experiment.

Collector The collector is a single piece of tantalum with a diameter of 12.7 mm ($1/2$ inch). It is cut from a tantalum sheet of thickness of 50.8 μm, flattened with a vice clamp, then deburred with hand tools to remove rough edges. As mentioned previously, tantalum is a refractory metal that has a high melting point. It is also relatively inert and corrosion resistant (Burke 1940), which makes it very stable to use over a long period of time. Two tantalum disks are shown in Fig. 4.3f.

4.3.3 Wiring & Probe Shaft

Tantalum wires of diameters 0.5 mm (0.02 inch) are spot-welded onto the grid support and the back of the collector as shown in Fig. 4.4a. The wires are slightly longer than the length of the probe shaft as the ends have to be attached to LEMO connectors during the final assembly of the probe. The wires are then insulated with 1 mm outer diameter plastic wire tubing that covers the wire up to the spot-welded point on the grid support. The wires have to be completely insulated in order to avoid having two neighboring wires touch and short the electrical connections after they have been assembled into the stack of electrodes.

The insulated wires are then threaded through a ceramic tube attached to the probe shaft with a MACOR® adapter as seen in Fig. 4.4b. MACOR® is a type of glass ceramic that is similar to regular ceramic but is easily machinable with a computer numerical control (CNC) machine and regular metalworking tools such as a drill or a tap. The MACOR® adapter is used to hold the ceramic tube in place while it is attached to the probe shaft by two tapped screws.

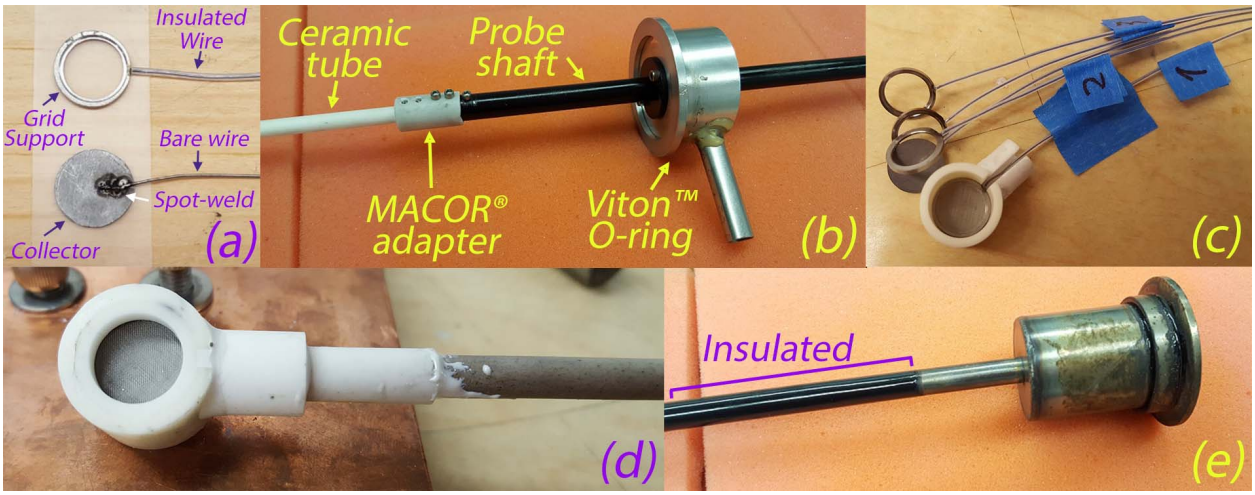

Figure 4.4: (a) Tantalum wires spot-welded to the side of a grid support (top) and the back of the tantalum collector (bottom). The top wire is insulated with plastic tubing. (b) A ceramic tube is connected to the probe shaft with an adapter made of MACOR®. This is used to insulate wires that run from the probe head to the opposite end of the probe shaft. A Viton™ O-ring is also pictured. (c) A set of grid supports with wires partially assembled into the ceramic housing. The wires enter through the groove in the ceramic. (d) The front face of the assembled probe head. The joints between the individual parts are sealed with epoxy. (e) A cylindrical-shaped cup at the end of the probe shaft that holds the LEMO connnectors. The black area of the probe is coated with insulation.

A ceramic tube with an inner diameter of 4.77 mm (0.188 inch), outer diameter of 6.35 mm ($1/4$ inch) and length of approximately 25 cm is used to protect the plastic wire tubing from being exposed to the plasma. It can slide in and out of the adapter to adjust the distance between the probe head and the tip of the probe shaft and is also secured to the MACOR® adapter with two tapped screws.

The probe shaft is a 1.3 m long stainless steel tube of inner diameter 10 mm that is open to a cylindrical-shaped cup that has ISO KF-40 fitting dimensions. As shown in Fig. 4.4e, the probe shaft is coated with a layer of black insulation that electrically isolates the probe from the plasma, while the cylindrical-shaped cup allows the probe to be vacuum sealed with a delrin cap when inserted onto the LAPD. The delrin cap has five LEMO adapters that allow electrical connections to be made to each of the electrodes while the probe is operating.

4.3.4 Final Assembly

The final assembly of the probe involves carefully stacking the electrodes into the probe head one at a time as shown in Fig. 4.4c. The stack of electrodes is then sealed off using a solid, cylindrical piece of ceramic that has a diameter equal to the inner diameter of the ceramic housing ($d = 9.52$ mm). The cylinder compresses the stack of electrodes to ensure that there are no gaps between the insulator and the grids. A groove is also made in the cylinder such that it fits the shape of the wire that is spot-welded onto the back of the collector, and the cylinder is then epoxied in place.

The wires are then slowly retracted from the other end of the probe shaft until the probe head attaches itself on top of the ceramic tube. All the gaps between the different parts of the energy analyzer are then filled with epoxy such that only the front of the probe is exposed. Fig. 4.4d shows the front of the assembled probe head.

At the end of the probe, LEMO connectors were spot-welded on the ends of the wires. The connectors are then attached to the back of the delrin cap and the assembly is complete.

4.4 Operational Considerations

In this section, some considerations that affect the operation of the ion energy analyzer are discussed.

4.4.1 Space Charge Limited Current

The accumulation of space charge within the ion energy analyzer limits the amount of current that can be measured by the probe. This generally depends on the spacing between electrodes and the potential that is applied on each of these electrodes.

As ions reach the collector, positive charges accumulate near the collector surface and increase the surface potential. This continues until the build up of charges reaches a point where the

surface potential is strong enough to start repelling more of the energetic ions and the collected current saturates. The saturated current is the *space charge limited current*. This determines the upper limit for the current collected by the ion energy analyzer.

An expression for the space charge limited current density J_{sc} is given by the Child–Langmuir law (Child 1911; Langmuir 1913),

$$J_{\mathsf{sc}} = \frac{4\epsilon_0}{9}\sqrt{\frac{2e}{m}}\frac{V^{3/2}}{x^2} \tag{4.4.1}$$

where x and V are the separation and potential difference between the suppressor grid and collector respectively. This assumes the suppressor grid and collector are infinite planes and the ions leave the suppressor grid with zero initial velocity.

Correction terms In reality, however, the ions that leave the suppressor grid may have a Maxwellian velocity distribution and this has to be accounted for when solving Poisson's equation. In addition, the ions can form a cloud around the collector when they accumulate in front of its surface, creating a potential maximum V_m a distance x_m away from the suppressor as seen in Fig. 4.5 (Langmuir 1923). This potential maximum can be treated as a virtual cathode that separates the region into two areas, one which contains the incoming current density J_0 and reflected current density $J_0 - J_{sc}$, and the other that allows only J_{sc} to pass.

Langmuir and Compton (1931) solved the Poisson's equation with the above-mentioned modifications for electrons leaving a heated cathode. However, the differential equations can be modified for ions arriving at a saturated collector with nearly identical solutions. The derivation is given in Appendix A.3. The resulting analytic approximation of J_{sc} becomes

$$J_{sc} \approx \frac{4\epsilon_0}{9}\sqrt{\frac{2e}{m}}\frac{(V_m - V)^{3/2}}{(x_m - x)^2}\left(1 + \frac{3\sqrt{\pi}}{2}\sqrt{\frac{kT_i}{e(V_m - V)}}\right) , \tag{4.4.2}$$

where kT_i/e is the ion temperature in eV (Brunner et al. 2013a). This is effectively the Child–

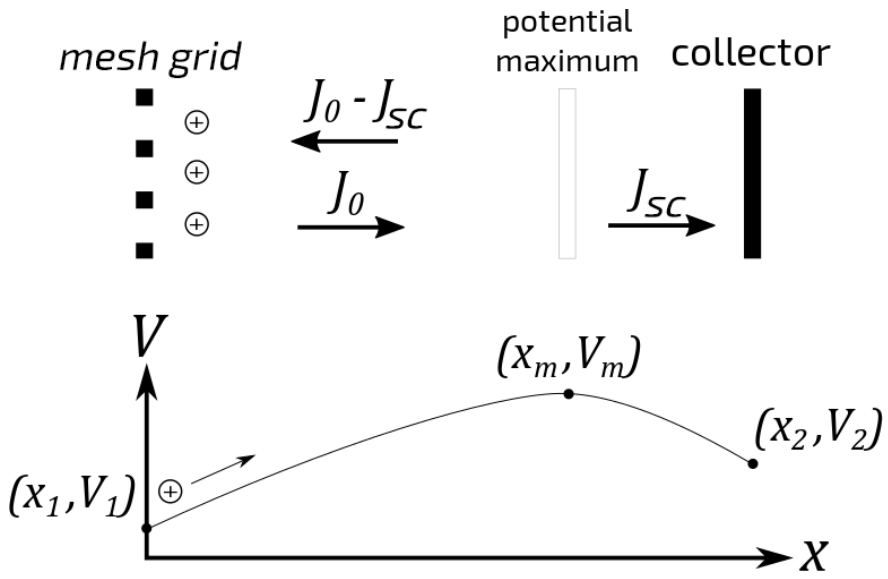

Figure 4.5: The coordinate system for calculating the space charge limited current using a virtual cathode. The build up of space charge creates a reflected current density $J_0 - J_{sc}$, where J_0 is the incoming current density and J_{sc} the space charge limited current. The suppressor grid, virtual cathode and collector are located at x_1, x_m and x_2, while their potentials are V_1, V_m and V_2 respectively.

Langmuir law in (Eq. 4.4.1) with correction terms.

Numerical approximation The difficulty of using (Eq. 4.4.2) to determine J_{sc} is that V_m and x_m are hard to obtain from experiment. As a result, J_{sc} is frequently estimated by guessing the values of V_m and setting x_m to x_2, the position of the collector (Pitts et al. 2003; Nedzelskiy et al. 2006; Dreval et al. 2009). The latter may not be desirable as it defeats the initial purpose of incorporating the cloud of ions into the model to account for the space charge around the collector.

One possible approach in improving the estimate of J_{sc} is to remove x_m as an unknown variable by matching the boundary conditions at x_m for the two regions before and after the potential maximum V_m. This involves using the characteristic equation from which (Eq. 4.4.2)

was derived

$$\xi_{\pm}(\eta) = \int_0^{\eta} \frac{\mathrm{d}\eta'}{\sqrt{e^{\eta'} - 1 \pm \left(e^{\eta'} \cdot \mathrm{erf}\sqrt{\eta'} - \frac{2}{\sqrt{\pi}}\sqrt{\eta'}\right)}} \ , \tag{4.4.3}$$

where $\mathrm{erf}(Y)$ is the error function

$$\mathrm{erf}(Y) = \frac{2}{\sqrt{\pi}} \int_0^{Y} \mathrm{d}t \, e^{-t^2} \ . \tag{4.4.4}$$

The derivation of this equation is also given in Appendix A.3. Then, ξ is a dimensionless position coordinate given by

$$\xi = 2L(x_m - x) \qquad \text{with} \qquad L = \left[\frac{J_{sc}e}{\varepsilon_0}\sqrt{\frac{2\pi m}{(kT_i)^3}}\right]^{1/2} \ ,$$

and η is a dimensionless potential coordinate given by

$$\eta = \frac{e(V_m - V)}{kT_i} \ .$$

In (Eq. 4.4.3), ξ_+ represents the region from x_1 to x_m while ξ_- represents the region from x_m to x_2. The equation (Eq. 4.4.2) was obtained from the approximation of ξ_+ in (Eq. 4.4.3) for large η. The coordinates for the suppressor grid is then

$$\eta_1 = \frac{e(V_m - V_1)}{kT_i} \qquad \& \qquad \xi_1 \equiv \xi_+(\eta_1) = 2L(x_m - x_1) \ ,$$

while the coordinates for the collector is

$$\eta_2 = \frac{e(V_m - V_2)}{kT_i} \qquad \& \qquad \xi_2 \equiv \xi_-(\eta_2) = 2L(x_m - x_2) \ .$$

Solving for J_{sc} by combining ξ_1 and ξ_2 results in

$$J_{sc} = \left(\frac{\xi_+(\eta_1) - \xi_-(\eta_2)}{2(x_2 - x_1)} \right)^2 \frac{\varepsilon_0}{e} \sqrt{\frac{(kT_i)^3}{2\pi m}} \ , \tag{4.4.5}$$

which does not depend on x_m. However, it is still necessary to guess the value of V_m as it is contained in η_1 and η_2.

The following parameters were then substituted into (Eq. 4.4.5): $m = 4.0026$ amu for helium (Meija et al. 2016), $(x_2 - x_1) = 1.4$ mm is the average grid separation determined from the thickness of the grid support plus the mica washers, $V_1 = -76.5$ V and $V_2 = -67.5$ V are the suppressor and collector biases respectively and $T_i = 4$ eV is the ion temperature. The probe area A is 71.2 mm^2 given the inner diameter of the grid support ($d = 9.52$ mm).

Using a value of $V_m = 50$ V, the value of the space charge limited current ($I_{sc} \equiv J_{sc}A$) was estimated to be 2.59 mA. This limit is very much above the observed current value of 80 μm (see Chapter 5.1. This means that space charge is not a limiting factor for the collected ion current in the energy analyzer.

4.4.2 Energy Resolution

The energy resolution of an ion energy analyzer is affected by deviations in the path of the incoming ions as they move away from the axial trajectory of the energy analyzer before reaching the discriminator grid (Molvik 1981). This reduces the energy of the ions along the axial direction and creates a spread in the measured ion energy, thus reducing the precision of the analyzer measurement.

The resolution of the energy analyzer is typically defined by the ratio $\Delta E/E$, where E is the initial kinetic energy of the ions in the axial direction, and ΔE is the overall decrease of E (Böhm and Perrin 1993). It depends on the factors such as the initial kinetic energy of the ions E, the bias applied on the grids, as well as geometric factors such as the size and spacing of the mesh

opening and the spacing between grids. As a result, $\Delta E/E$ is sometimes estimated by the ratio of the mesh opening s to the characteristic length of the energy analyzer l,

$$\frac{\Delta E}{E} \approx \frac{s}{2\pi l} \tag{4.4.6}$$

(Sakai and Katsumata 1985). Using a mesh opening size of 43.2 μm, a grid spacing of 1.4 mm and (Eq. 4.4.6), the energy resolution of the ion energy analyzer was estimated to be 0.5%.

4.5 Summary

In this chapter, the theory and operating principle of a four-grid retarding field energy analyzer that measures the ion energy distribution function was discussed. The grids are biased to repel electrons and selectively screen ions based on their kinetic energies. This allows an I-V curve to be constructed by plotting the collected current as a function of the discriminator grid voltage, which can then be integrated to give the ion energy distribution function $f(E)$. A detailed description of the design and construction process of the ion energy analyzer was presented. Operational considerations such as the space charge limited current and the energy resolution of the energy analyzer were also discussed.

Chapter 5

Ion Temperature Measurements

This chapter presents the methods and techniques used to measure and estimate the ion temperature of the two flux ropes using the ion energy analyzer described in Chapter 4. The measurements are complemented with line-of-sight, volume averaged measurement made by a high-resolution spectrometer as a check for consistency and to determine the ion temperature across the magnetic field.

5.1 Ion Energy Analyzer Measurements

5.1.1 Experimental Cases

In this study, there are two cases in which the ion energy analyzer took measurements. These are summarized in Table 5.1, which shows the discharge conditions of flux rope plasma (i.e. the discharge potential V_D and the current through a single rope I_R), as well as the location of the ion energy analyzer and the direction it was facing when taking measurements. In both cases, the energy analyzer was located near the region between the two ropes where magnetic reconnection usually occurs. Fig. 5.1 marks the position of the ion energy analyzer ('$\times$') for both cases on a quiver plot of the magnetic field at $z = 3.2$ m.

Table 5.1: The parameters of the two cases of ion energy analyzer measurements.

	Discharge conditions		Coordinates			Probe face direction
	V_D [V]	I_R [A]	x [cm]	y [cm]	z [cm]	
Case 1	120	610	(3.4 ,	0.0 ,	420)	$\pm y$, $\pm z$
Case 2	140	550	(6.0 ,	1.7 ,	540)	$\pm z$

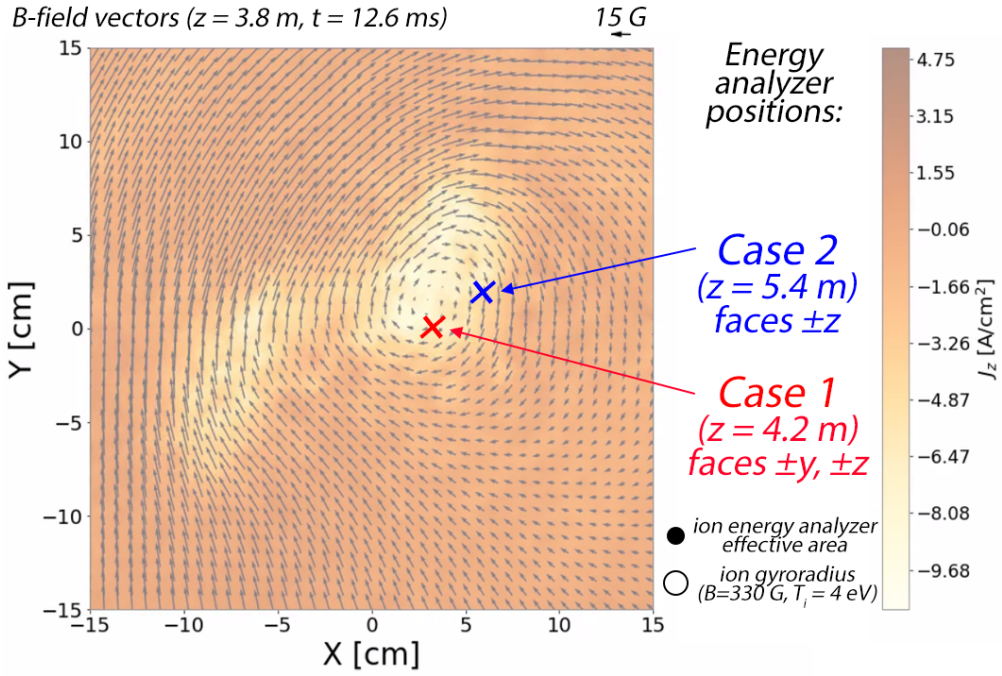

Figure 5.1: A quiver plot of the magnetic field showing the locations of the ion energy analyzer that was used to collect data. The probe was located at $z = 4.2$ m for Case 1 ($V_D = 120$ V, $I_R = 610$ A) and $z = 5.4$ m for Case 2 ($V_D = 140$ V, $I_R = 550$ A). The effective area of the probe and the size of the ion gyroradius are indicated at the bottom right.

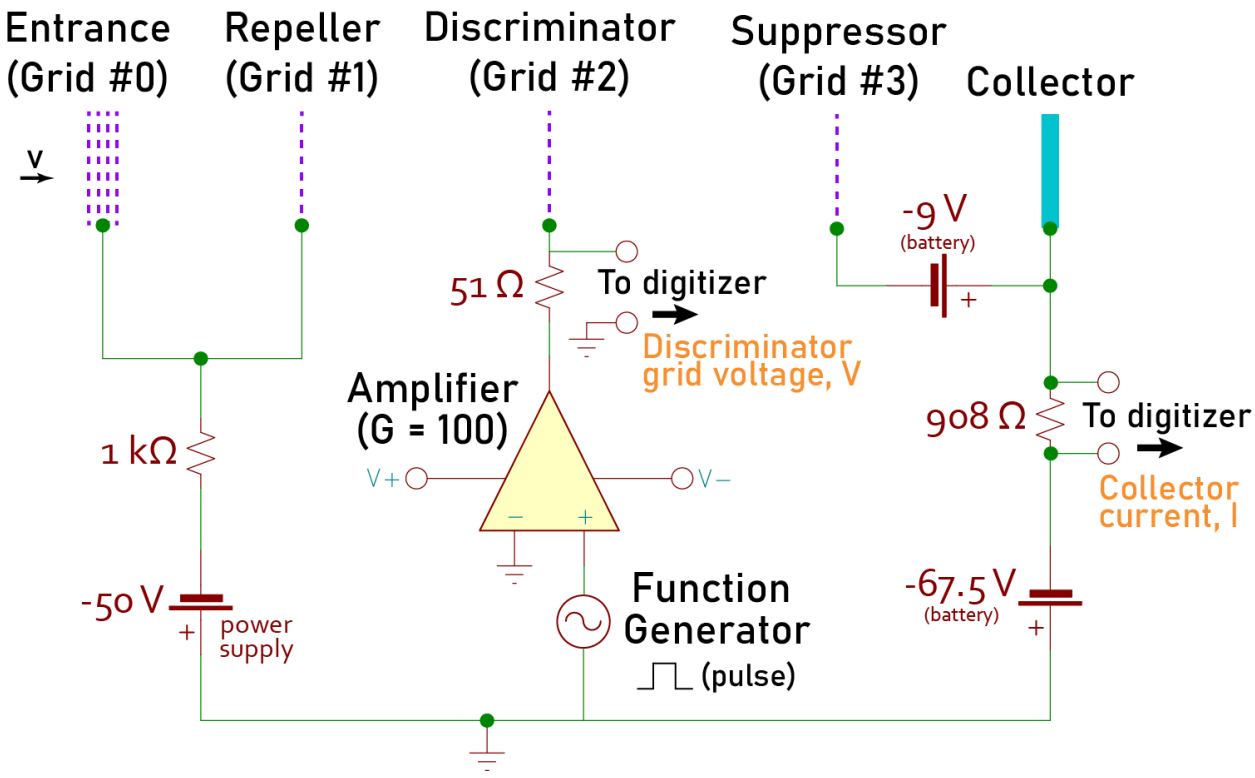

Figure 5.2: The circuit diagram for the setup of the energy analyzer.

5.1.2 Experimental Setup

The ion energy analyzer is set up according to the circuit diagram as shown in Fig. 5.2. In this experiment, the entrance grid (#0) is shorted to the repeller grid (#1) and both grids biased at -50 V with a DC power supply. The bias potential on the entrance grid was found to be necessary as it further reduces the number of electrons that enter the energy analyzer and significantly improves the quality of the measured collector current.

The potential on the discriminator grid (#2) is varied using an amplified signal from a function generator. The internal capacitance of the energy analyzer prevents the discriminator grid from rapidly being swept with a low to high voltage ramp as it produces a capacitive current (i.e. $I = C\frac{dV}{dt}$) that is significantly larger the collector current. This drowns the useful signal in noise and prevents good data from being acquired.

The solution is to then bias the discriminator grid at a constant voltage and slowly increase

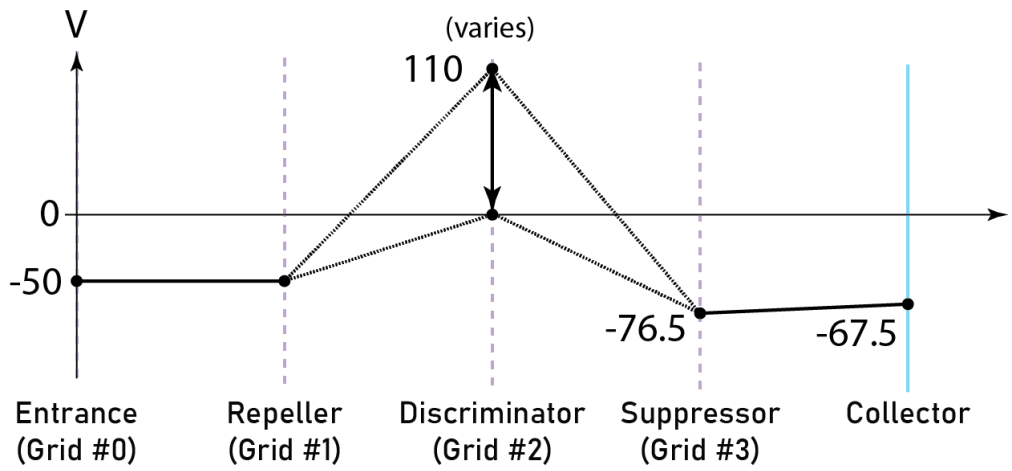

Figure 5.3: A plot of the potential distribution of the grids within the ion energy analyzer.

the voltage between each plasma discharge. The biasing is achieved with a square pulse from a function generator that triggers when the flux ropes are turned on (9 and 15 ms). The baseline of the square pulse is negative (-20 V) to avoid drawing an electron current when the probe is idle, while the high level of the pulse ranges from 0 to 110 V. The high level is gradually stepped up after every 100 shots in steps of 0.25 V (441 steps).

The grid potential is measured using a Tektronix $50\times$ attenuation high voltage differential probe and then sent to the data acquisition system (DAQ) for collection. The DAQ also automatically reprograms the pulse on the function generator to the next desired ramp voltage after 100 data shots have been collected.

As discussed in Chapter 5.1.2, the suppressor grid ($\#3$) is biased with respect to the collector at -9 V to repel secondary electrons. The collector itself is then biased negatively at -67.5 V to collect ion current. The potential distribution of the grids and collector are plotted in Fig. 5.3. For the suppressor grid and the collector, the bias is provided by smaller-than-palm-sized alkaline batteries which can produce a stable DC output and not introduce noise that is usually generated from a power supply. The collector current is then measured by determining the potential difference across a 908 Ω resistor. This signal passes through a 3 MHz opto-isolator before being digitized.

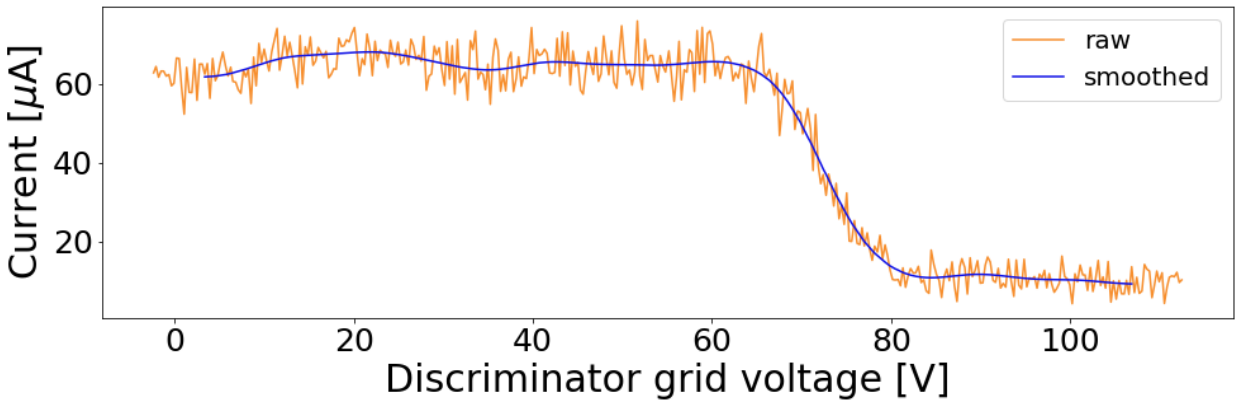

Figure 5.4: A typical I-V curve for when the flux ropes are turned on at $t = 11.27$ ms. The blue curve is the smoothed version of the raw data which is shown in orange. Each point on the orange curve was acquired from the conditionally averaged current using the phase difference from a fixed B-dot probe.

5.1.3 Obtaining the I-V Curve

The collector current I is plotted as a function of the discriminator grid voltage V to obtain an I-V curve for the ion current. To construct the I-V curve, 100 current time traces for each voltage step were conditionally averaged by temporally aligning each current traces with a phase acquired from a fixed magnetic probe (see Chapter 3.2). The procedure is then repeated for the 441 voltage steps. A specific time out of the 15650 time steps is then selected to plot the I-V curve. For example, Fig. 5.4 shows the I-V curve at $t = 11.27$ ms. The raw data is shown in orange, while a smoothed version is shown in blue.

5.1.4 Smoothing

The raw data from the I-V curve is smoothed with a digital filter as it noisy and contains fluctuations between adjacent points that would be amplified when computing the derivative $-dI/dV$ using finite differences.

The smoothing is performed with a Savitzky–Golay filter with a window of 31 points and polynomial order of 2. The parameters were determined by constructing a test distribution function, integrating it and then adding noise to mimic the raw data as shown in Fig. 5.4. This

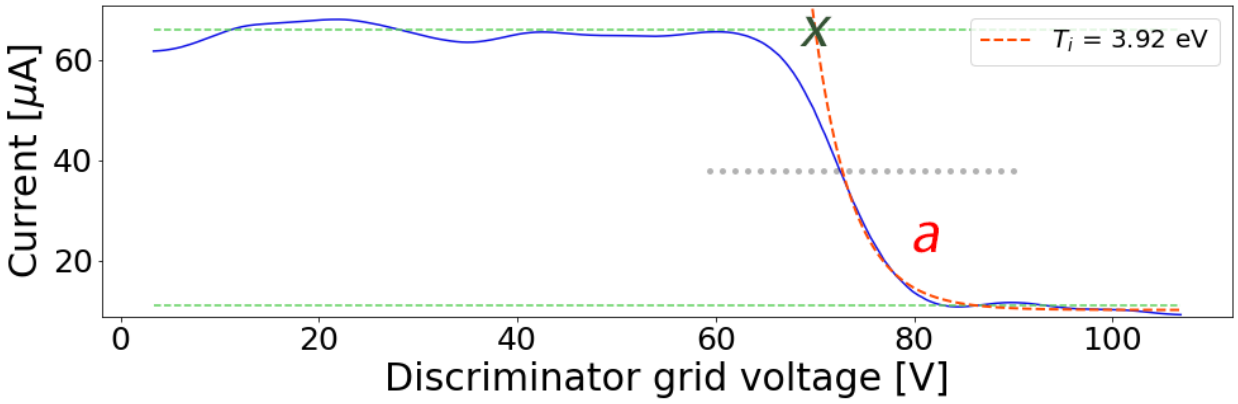

Figure 5.5: Exponential fit of the I-V curve to determine the ion temperature T_i. The green dotted horizontal lines are the ion saturation (top) and the minimum current (bottom) levels respectively. The exponential is fitted to the bottom half region of the curve denoted by a. The plasma potential V_p is estimated from the intersection of the ion saturation level and an extrapolated exponential fit and is marked by a cross ($\times$).

test signal is then passed through the filter and differentiated in an attempt to recover the original distribution function. The parameters on the filter were adjusted until an output signal close to the original is obtained. This process is optimized by visual inspection of the output (Magnus and Gudmundsson 2008) and the end result involves passing the signal through the filter twice to remove most of the noise.

The trade-off for having a smoothing window greater than 31 points is that while data is smoothed more evenly, there is a risk of skewing and distorting the gradient at the region between the saturation current and where the current is expected to be zero. This affects the determination of the ion temperature. In addition, half the number of points in the smoothing window have to be discarded at both ends of the curve as these points are not smoothed by the routine. Thus, a smoothing window of 31 points was found to be an acceptable compromise for a curve with 441 points.

5.1.5 Determining T_i From the I-V Curve

Estimates for the ion temperature T_i can be determined from the smoothed I-V curve using the two methods described in Chapter 4.2. The first is a direct fit of the I-V curve to an exponential with (Eq. 4.2.1),

$$I = \begin{cases} I_0 & \text{for } V \leq V_p \ , \\ I_0 \exp\left(-\dfrac{e(V - V_p)}{kT_i}\right) & \text{for } V \geq V_p \ , \end{cases}$$

which is expected to straightforward because the discontinuity at $V = V_p$ is a noticeable feature of the plot. In reality, however, locating $V = V_p$ is difficult as the gradient of the current decreases continuously and creates a transition region as V decreases and the current approaches the ion saturation current. This affects the starting point at which the exponential fit begins and hence the value of T_i.

A reasonable estimation for where the discontinuity is located is at the point on the curve where the gradient is a maximum, which intersects the grey dotted line at 72 V in Fig. 5.5. This avoids fitting the exponential to the transition region. In this case, fititng the exponential to the rest of the curve using least-squares where $V \geq 72$ V results in the red dashed line. The slope of the exponential gives an ion temperature of $T_i = 3.9 \pm 0.1$ eV. The error is the one standard deviation value of the variance in the best fitting T_i value.

The levels at which the ion current saturates or is at a minimum are indicated by the green dotted lines at the top and bottom of the figure respectively. The value of the minimum current level is not zero as there may be incomplete screening of the secondary electrons which creates a positive offset current (Böhm and Perrin 1993). Nevertheless, the offset is assumed to be zero when fitting the exponential to the data. In addition, the value of V_p is estimated from the value of V in which the ion saturation current crosses the extrapolation of the exponential fit function. This point is marked with a cross in Fig. 5.5.

5.2 The Distribution Function

5.2.1 Modes of the Distribution Function

As discussed in Chapter 4.2.3, ions that have non-Maxwellian distributions do not have a well-defined temperature. As such, the average energy $\langle 2E \rangle$, a quantity that is equivalent to the Maxwellian temperature when the distribution function is non-Maxwellian, is used to quantify the ion energy at localized regions within the flux ropes. This requires the determination of $f(E)$ to calculate $\langle 2E \rangle$. From (Eq. 4.2.13), $f(E)$ is given by

$$f(E) = -\frac{m}{Ze^2A}\frac{dI}{dV} \ ,$$

which is obtained by taking the derivative of the I-V curve. The derivative is computed numerically using a second-order central difference routine and then smoothed to remove the noise. A typical result is shown in green in Fig. 5.6a. The $-dI/dV$ curve is normalized such that the magnitude of $f(E)$ is comparable to the current and the single peak is visible when plotted on the same axis. This shows a single peak (i.e. unimodal distribution) which is the case for majority of the $-dI/dV$ curves plotted while the flux ropes are present. The peak is estimated to be the plasma potential V_p.

Fig. 5.6b shows a two-peaked distribution which occurs when the flux ropes collide. In this example, $f(E)$ can be fitted to a bi-Maxwellian distribution which is simply the sum of two normal distributions, i.e.

$$A_1 \exp\left(-\frac{(x-x_1)^2}{2b_1^2}\right) + A_2 \exp\left(-\frac{(x-x_2)^2}{2b_2^2}\right) + c \ , \tag{5.2.1}$$

where x_1, A_1, b_1, x_2, A_2, b_2 and c are fitting parameters. The curve of best fit is shown in blue and indicated by the red arrow, while the component Maxwellians that make up the distribution

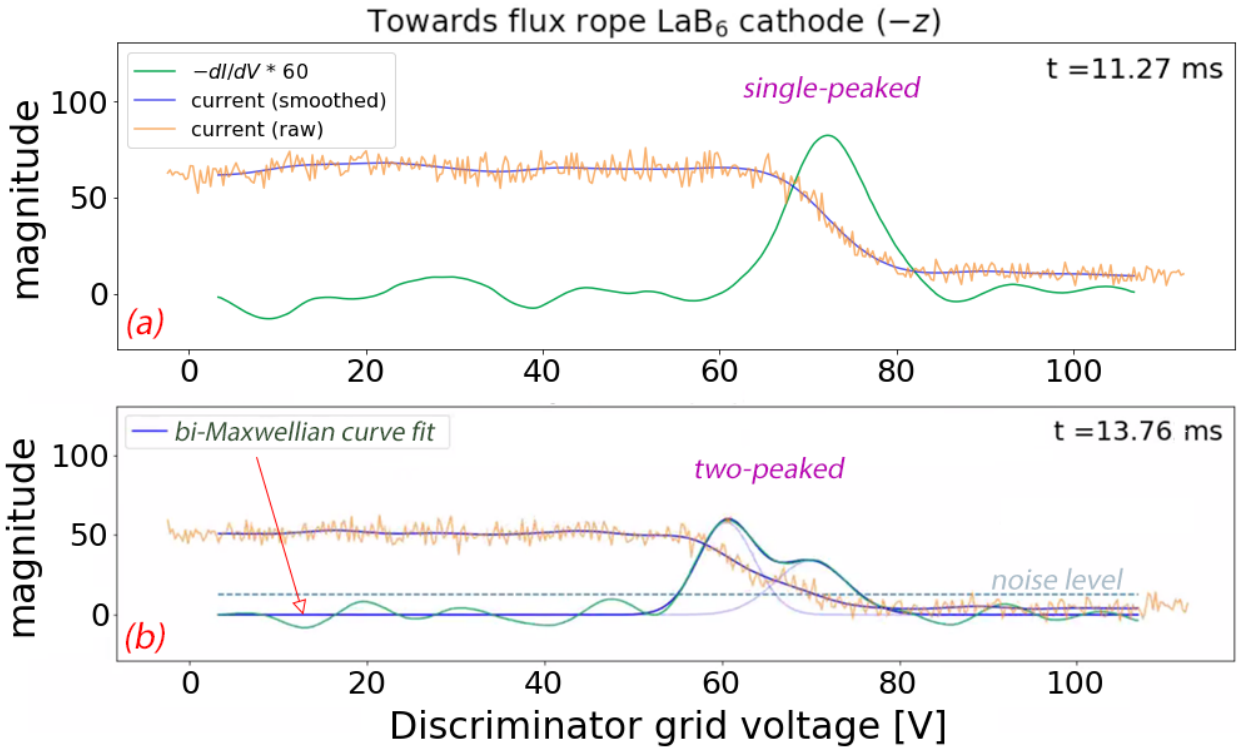

Figure 5.6: Plots of $-dI/dV$ (green) and their I-V curves for (a) a single-peaked distribution and (b) a two-peaked distribution. The unit of current is mA, while $f(E)$ is in arbitrary units. The two-peaked distribution is fitted to (Eq. 5.2.1) with parameters (x_1, A_1, b_1, x_2, A_2, b_2, c)= (60.52, 57.85, 3.17, 70.02, 33.72, 4.04, 0.04). The component Maxwellians are also plotted.

are plotted using the best fit parameters. The original data is shown in green. This fit suggests the presence of a beam that has a drift of 15 eV when compared to the primary distribution. The width of the individual distributions (i.e. b_1, b_2) is an estimate of the individual ion temperatures.

5.2.2 Establishing the Presence of a Beam

In plots of $-dI/dV$ that contain two-peaked distributions, it is necessary to ascertain if a secondary peak is due to a beam or a bump that is created by the smoothing of the noise. In Fig. 5.6, numerous bumps are present in the baseline of $-dI/dV$ where the current is expected to be constant (i.e. either when the energy analyzer is saturated with ion current or when the current is supposedly zero). These bumps could not be removed by the smoothing routine and

are inherently present in the data. A procedure was thus established to determine if $-dI/dV$ contained a secondary peak and would be fitted to a bi-Maxwellian distribution function.

The first step is to determine if the amplitude of the secondary peak is greater than the amplitude of the noise. In Fig. 5.6b, the noise amplitude was determined from the peak amplitude of the $-dI/dV$ oscillations for discriminator grid voltages less than 50 V and greater than 80 V. The noise level is indicated by the dotted line and any secondary peak has to have an amplitude greater than this level to be considered a signal. The discriminator grid voltage thresholds are determined by the inflection points that bound the primary peak and have magnitudes close to zero.

The second step is to check if the secondary peak has an amplitude at least 25% of the primary peak. This is an extension of the first test as the fitting routine would sometimes misinterpret the data as being bi-Maxwellian when the noise amplitude was too low. The 25% criteria was chosen such that a limited number of borderline cases could be rejected as most secondary peaks have amplitudes that are greater than 25% of the primary peak.

Finally, with the noise removed and the baseline of the distribution established, the last step is to establish that a beam is indeed present. It is straightforward to determine if a two-peaked distribution necessarily contains a beam by checking if the distribution is bimodal, i.e. it contains a mixture of two normal distributions. The check is established by proof (Robertson and Fryer 1969) using measurements of the individual peak heights (A_1, A_2), widths (b_1, b_2) and positions (x_1, x_2) in (Eq. 5.2.1) to determine the three dimensionless parameters

$$p = \frac{1}{1 + A_2/A_1} \ , \qquad \mu = \sqrt{2}\left(\frac{x_2 - x_1}{b_1}\right) \ , \qquad \text{and} \qquad \sigma = \frac{b_2}{b_1} \ .$$

These parameters transform the distribution function such that it is also dimensionless and invariant under scaling or translation. The function is then bimodal if and only if $\mu > \mu_0$ for some

μ_0 defined by

$$\mu_0 = \frac{\sqrt{2(\sigma^4 - \sigma^2 + 1)^{3/2} - (2\sigma^6 - 3\sigma^4 - 3\sigma^2 + 2)}}{\sigma} \ , \tag{5.2.2}$$

p lies within the open interval $(p_1,\, p_2)$ where

$$p_i^{-1} = 1 + \frac{\sigma^3 y_i}{\mu - y_i} \exp\left(-\frac{y_i^2}{2} + \frac{1}{2}\left(\frac{y_i - \mu}{\sigma}\right)^2\right) \qquad \text{for } i = 1 \text{ and } 2 \ , \tag{5.2.3}$$

and y_1 and y_2 are the roots of the equation

$$(\sigma^2 - 1)y^3 - \mu(\sigma^2 - 2)y^2 - \mu y + \mu\sigma^2 = 0 \tag{5.2.4}$$

which satisfy $0 < y_1 < y_2 < \mu$. The function is otherwise unimodal and single-peaked. A generally sufficient condition for a unimodal function is $|x_1 - x_2| \leq 2\min(b_1, b_2)$ (Behboodian 1970).

The determination of whether a single-peaked distribution contains a beam or not is, however, non-trivial. The approach taken is to fit $-dI/dV$ to both a single Maxwellian and a bi-Maxwellian function and then determine the function that best fits the data using the sum of least squares but above the noise level as determined in the previous step. A best fit of the data to a bi-Maxwellian function indicates the likely presence of a beam.

Fig. 5.7a shows an example of a $-dI/dV$ plot which is classified as unimodal but best fits a bi-Maxwellian function at $t = 12.651$ ms. The decomposition of the distribution function into its individual Maxwellians in Fig. 5.7b suggests that the beam has a 13.4 eV drift in the $+z$ direction with respect to the primary peak. However, the beam also has an amplitude that is close to the noise level which makes it slightly ambiguous to conclusively determine if it is indeed a beam. Thus, the context in which the beam is produced has to be taken into account and it is usually achieved by observing $-dI/dV$ slightly before and after the current timestep.

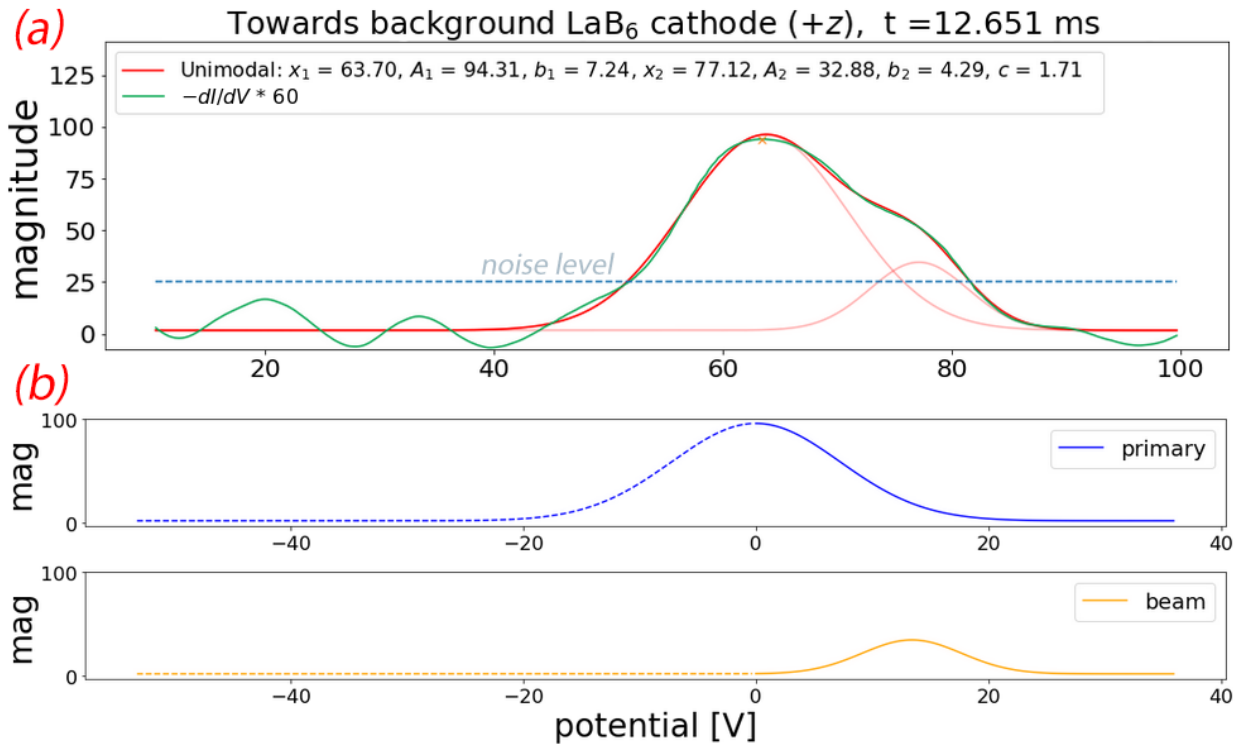

Figure 5.7: (a) Plot of a unimodal $-dI/dV$ that best fits a bi-Maxwellian function using least squares. (b) Plots of the primary and beam distributions that compose the bi-Maxwellian function in (a). The potential has been shifted such that the primary peak potential is zero. The dashed lines indicate the part of the curve that is below the primary peak potential.

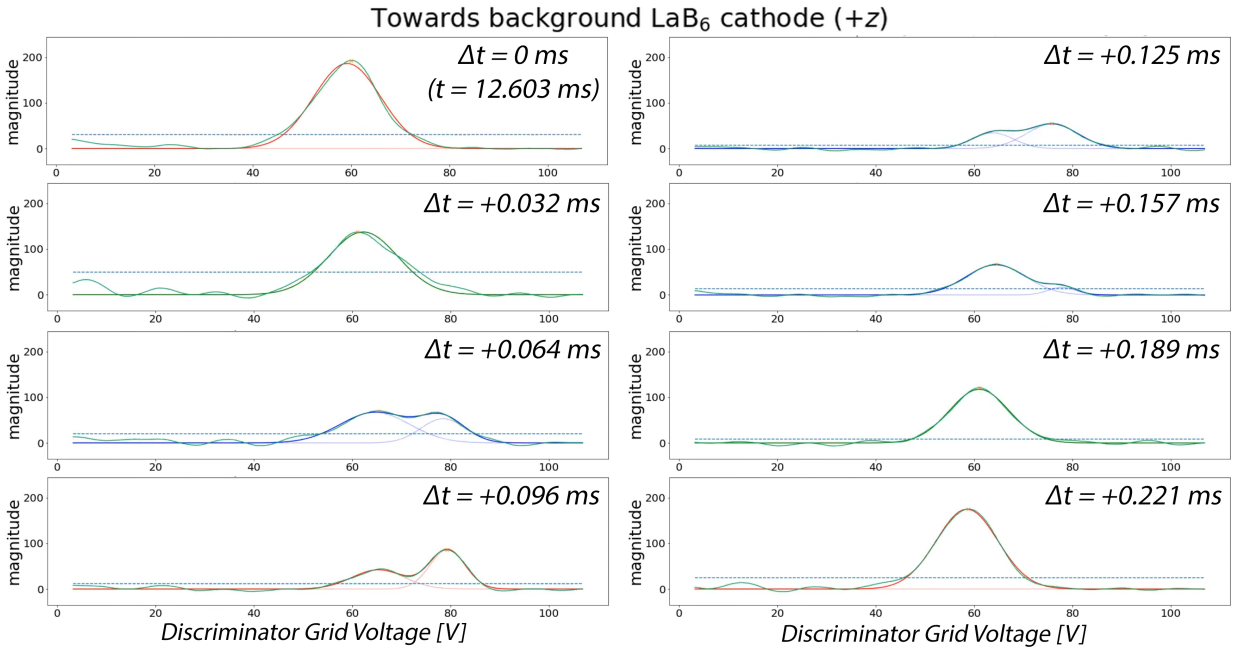

Figure 5.8: Time evolution of $-dI/dV$ showing the development of a beam for ions moving along the magnetic field and towards the background LaB_6 cathode in the $+z$ direction. The kink frequency of the ropes is about 3.9 kHz and the plots are within the duration of a single flux rope oscillation ($1/f = 0.256$ ms). The beam can be observed from the two-peaked distribution at $\Delta t = 0.096$ ms.

Fig. 5.8 shows the time evolution of $-dI/dV$ between $t = 12.603$ and 12.824 ms, which is the duration of a single kink oscillation ($f = 3.9$ kHz) and contains the $t = 12.651$ ms timestep of Fig. 5.7. The development of a beam from a single-peaked distribution is observed between $\Delta t = 0.064$ and 0.157 ms, and the presence of a beam is validated as the distribution function at $t = 12.699$ ms ($\Delta t = 0.096$ ms) was determined to be bimodal.

5.2.3 Peak Potential of the Primary Distribution

The peak potential of the primary distribution is assumed to be the plasma potential V_p as the drop in the collected current I is expected to be maximum at the point where the ion saturation current transitions to an exponentially dropping current. This is also the point where the ion energy E is set to zero and where the drift of the beam is measured with respect to. Therefore, an accurate determination of the primary peak potential would be important for constructing the

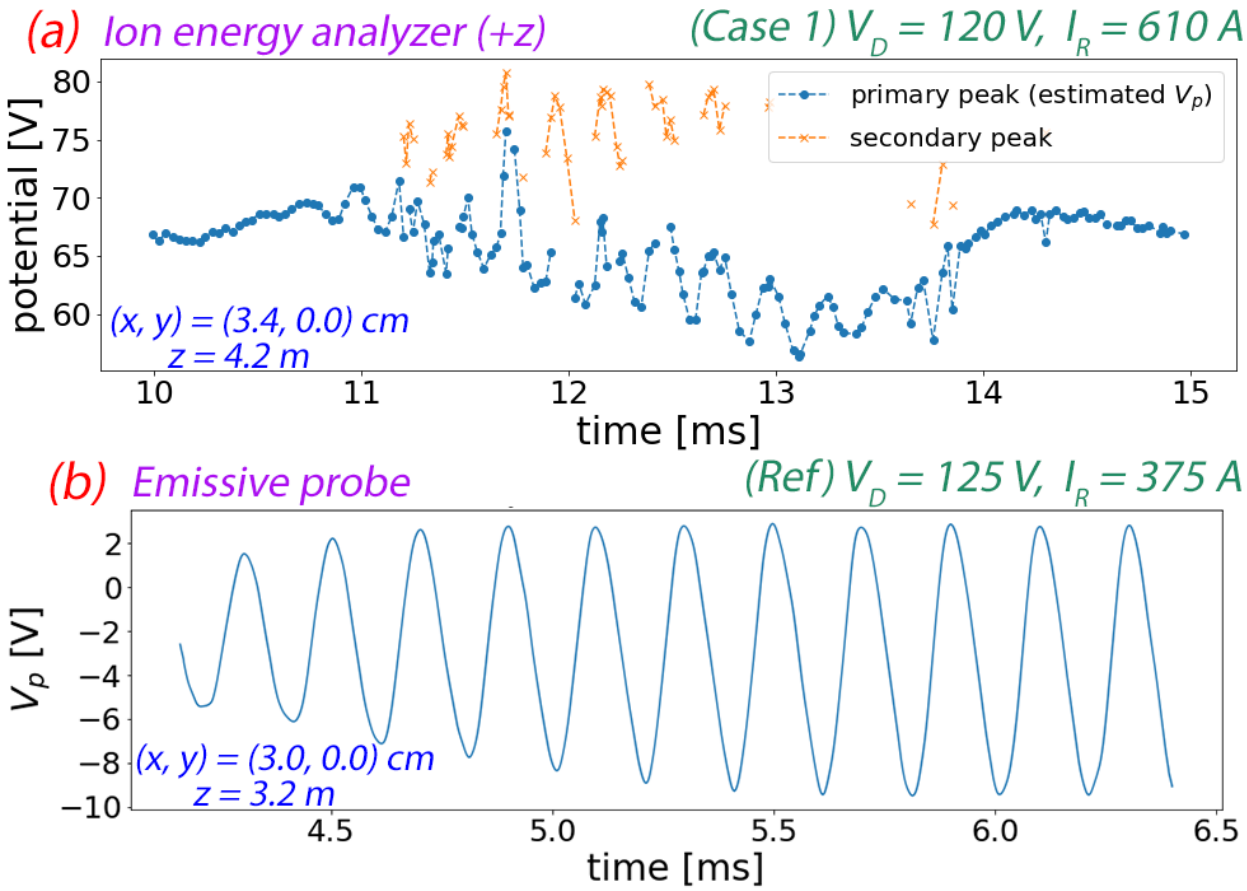

Figure 5.9: (a) Plot of the primary and beam (secondary) peak potentials as a function of time from the ion energy analyzer in Case 1. The secondary peak potentials are only plotted when $-dI/dV$ fits a bi-Maxwellian. (b) Plot of the plasma potential V_p as a function of time from an emissive probe. The data is from a reference dataset in a previous experiment (Gekelman et al. 2018a).

full bi-directional distribution function $f(E)$.

The validity of using the primary peak potential as an estimate for V_p can be shown by comparing a plot of the measured peak potentials from the ion energy analyzer to the plasma potential measured by an emissive probe in Fig. 5.9. An emissive probe measures the plasma potential from the I-V curve of a hot wire as described in Kemp and Sellen Jr. (1966). The ion energy analyzer data is from Case 1 ($V_D = 120$ V, $I_R = 610$ A) while the emissive probe data is from the reference dataset with flux ropes under slightly different conditions ($V_D = 125$ V, $I_R = 375$ A).

Fig. 5.9a shows a plot of the primary peak potential (blue) as a function of time. The potentials are above 50 V due to the -50 V applied on the entrance grid of the energy analyzer. The beam peak potentials (orange) are plotted when the distribution function best fits a bi-Maxwellian function and only occurs at specific intervals of time between 11 and 13 ms, which is when the flux ropes are rotating and colliding with each other. During this period of time, the primary peak potential fluctuates between 6 to 10 V at the kink frequency of the ropes ($f_R = 3.9$ kHz).

Fig. 5.9b shows the fluctuations in the V_p as measured by an emissive probe, which is located at approximately the same xy-position as the ion energy analyzer but spaced $\Delta z = 1.0$ m apart. The V_p fluctuations range from 8 to 12 V, which is on the same order of magnitude as the potential fluctuations of the primary peak potential. The fluctuations are also oscillating at the kink frequency ($f_R = 5$ kHz). This shows that the primary peak potential is correlated with the plasma potential. The use of the primary peak potential as an estimate for the plasma potential is therefore a valid approximation.

5.3 Ion Energy and Temperature Along the Magnetic Field

5.3.1 Combining Two Distribution Functions

As discussed in Chapter 4.2.3, the calculation of the average energy $\langle 2E \rangle$ requires splicing two $f(E)$ measurements from the ion energy analyzer when it faces opposite directions along the same axis. Each $f(E)$ curve is obtained from $-dI/dV$ for which $V \geq V_p$ and $E = 0$ is equivalent to $V = V_p$.

The value of V_p is estimated to be the peak potential of a single-peaked distribution and it is the peak potential of the primary distribution for a bimodal or two-peaked distribution. Then, denoting the distribution functions where ions travel along the positive and negative directions of the axis as $f_+(E)$ and $f_-(E)$, the $f_-(E)$ curve is reflected horizontally and then scaled in

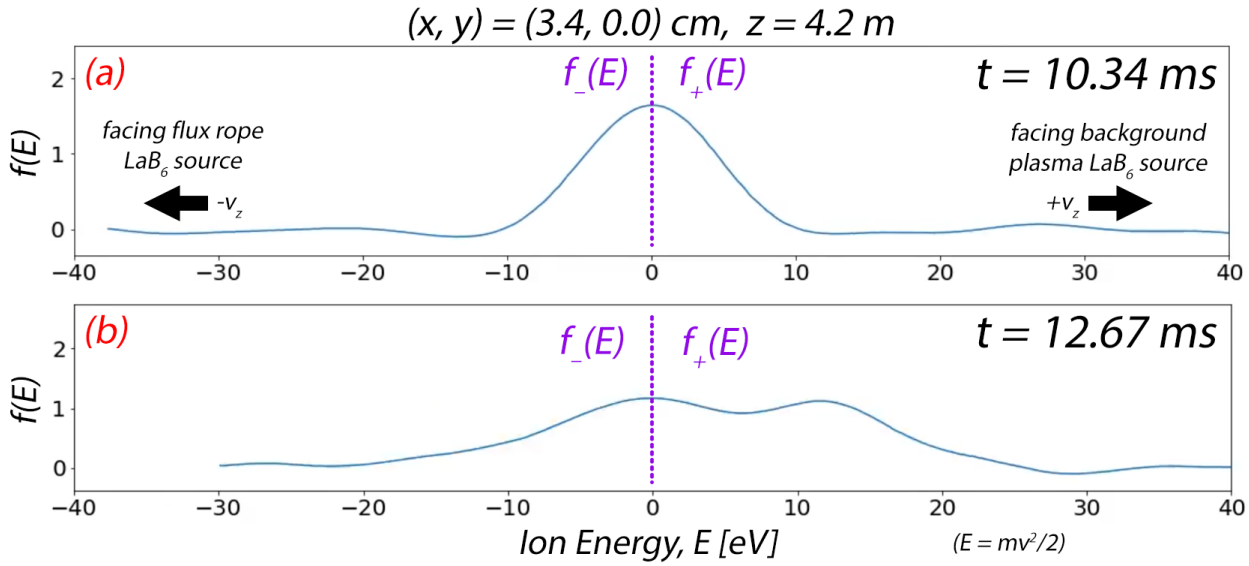

Figure 5.10: Spliced distribution functions along the magnetic field (z-axis) at two different times. The sign of E represents the direction the ions are traveling along z. (a) is a symmetric plot obtained from single-peaked $f_-(E)$ and $f_+(E)$ functions while (b) is the combination of a single-peaked $f_-(E)$ and a two-peaked $f_+(E)$.

magnitude such that $f_-(0) = f_+(0)$. The two curves are then spliced at $E = 0$ to create a continuous function in E. Some examples of spliced distribution functions for ions moving along the z-direction are shown in Fig. 5.10. Fig. 5.10a shows the combination of two single-peaked distributions while Fig. 5.10b is for a single-peak combined with a two-peaked distribution.

5.3.2 Calculating the Average Energy $\langle 2E \rangle$

The average energy $\langle 2E \rangle$ as a function of time for the ropes in both Case 1 ($V_D = 120$ V, $I_R = 610$ A) and Case 2 ($V_D = 140$ V, $I_R = 550$ A) is calculated and shown in Fig. 5.11a and Fig. 5.11c respectively. Since a bi-Maxwellian distribution function indicates that a beam is present, the data points in each of these figures are colored such that it is orange ($\times$) when either $f_+(E)$ or $f_-(E)$ contains a bi-Maxwellian function, or it is blue ($\bullet$) otherwise.

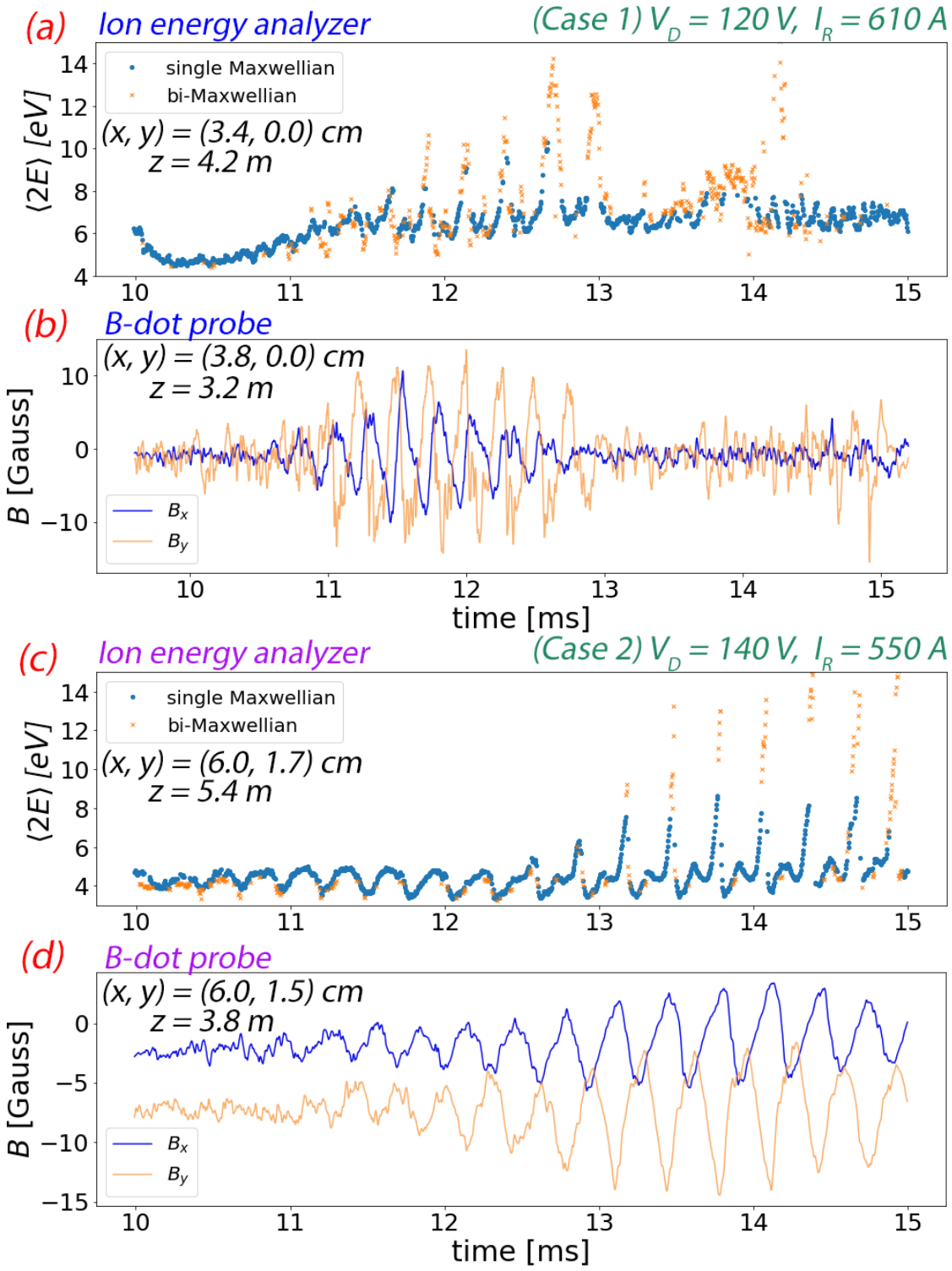

Figure 5.11: Plot of (a) the average energy $\langle 2E \rangle$ and (b) the local magnetic field B as a function of time in the presence of the flux ropes for Case 1 ($f = 3.9$ kHz). The probes are located such that the x and y coordinates are almost aligned with each other. In the z-direction, the B-dot probe is located about 1 m away from the energy analyzer and is closer to the source of the flux ropes. Plots (c) & (d) are the identical to (a) & (b), but for Case 2 ($f = 3.4$ kHz).

Case 1 In Fig. 5.11a, the bi-Maxwellian distribution functions produce spike-like structures in $\langle 2E \rangle$ between 11 and 13 ms. These spikes indicate the development of beams such as the one shown in Fig. 5.8, which appear to drift with energies between 10 and 15 eV. These drifts (~ 1.6 – 1.9×10^6 cm/s) are on the order of the ion sound speed ($c_s = 1.3 \times 10^6$ cm/s for $T_e = 7$ eV) but are significantly smaller than the Alfvén speed ($v_A = 2.54 \times 10^7$ cm/s). In addition, a comparison of the widths between the primary distribution and the beam suggest that both are approximately at the same temperature which ranges from 4 to 7 eV. This will be shown later in Chapter 5.3.3. This is the range of $\langle 2E \rangle$ values formed by majority of the single Maxwellian data points in Fig. 5.11a. Overall, these analyses suggest that the spikes in the $\langle 2E \rangle$ are primarily due to an increase in the kinetic energy of the ions rather than an increase in the temperature by heating. Therefore, the average energy does not reflect the ion temperature in the presence of a drifting beam component.

Nevertheless, $\langle 2E \rangle$ is useful in indicating changes in the kinetic energy of the system as a function of time. The spikes in $\langle 2E \rangle$ between 11 and 13 ms occur at the kink frequency ($f = 3.9$ kHz) and appear highly correlated with the coherent oscillations of the ropes within the same time interval as shown by the magnetic field components B_x and B_y in Fig. 5.11b. These magnetic field components appear slightly earlier in time as they were measured by a B-dot probe fixed at a point $\Delta z = 1.0$ m away from the ion energy analyzer, but closer to the flux rope LaB_6 cathode.

Case 2 The same analysis in Case 1 is repeated for the ropes in Case 2 (Fig. 5.11c). There is variation in the behavior of the ropes as measurement from the B-dot probe plotted in Fig. 5.11d show that the ropes oscillate at a different kink frequency ($f = 3.4$ kHz) and the large coherent oscillations occur between 13 and 15 ms. The B-dot probe in Case 2 is $\Delta z = 1.6$ m away from the ion energy analyzer. However, the data consistently shows a strong correlation between the $\langle 2E \rangle$ spikes and the coherent oscillations of the ropes.

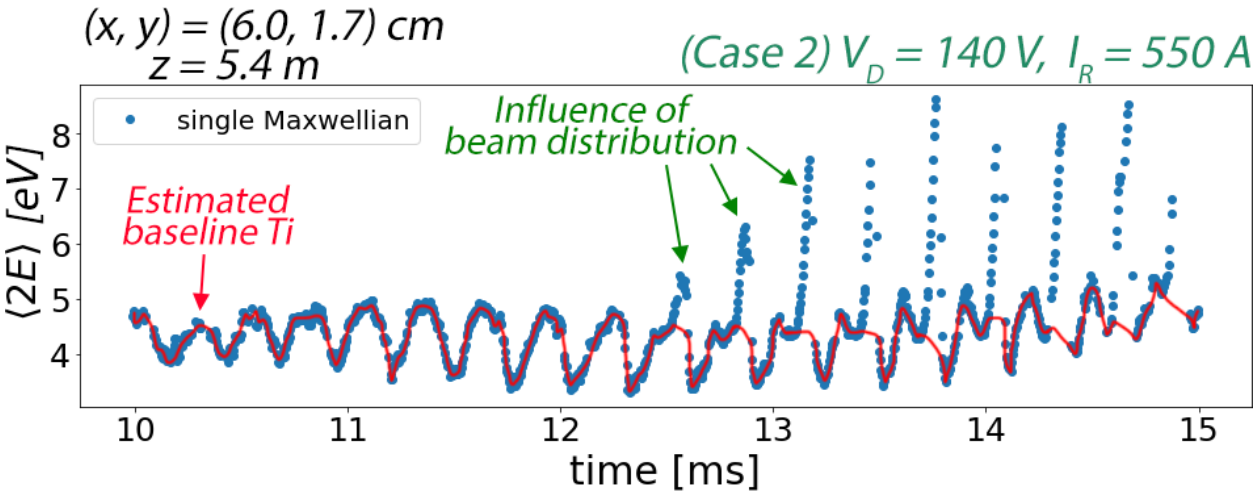

Figure 5.12: A plot of $\langle 2E \rangle$ which only consists of single Maxwellian data points from the Case 2 in Fig. 5.11c. Beam distributions begin to appear periodically at 12.5 ms and create streaks of increasing $\langle 2E \rangle$ up to 9 eV. The red line estimates the baseline ion temperature of the ropes assuming the oscillations from 10 and 12 ms continue on without being influenced by the beam.

Fig. 5.11c shows some data points that are fitted to a single Maxwellian form streaks of increasing $\langle 2E \rangle$ for up to 9 eV. These streaks are due to the presence of a beam as the data points above 9 eV that continue the streaks later in time are shown to be bi-Maxwellian. The data points that appear as a single Maxwellian are due to small beam drift velocities that do not separate the beam far enough from the primary distribution for the overall distribution to be resolved as two distinct peaks. Nevertheless, it is still able to increase the overall average energy.

The Maxwellian ion temperature of the ropes in Case 2 appear to be between 3 and 5 eV as shown by the oscillations between 10 and 12 ms in Fig. 5.11c. Since the beam is not present during this period of time as indicated by the lack of bi-Maxwellian data points with significant $\langle 2E \rangle$ above 8 eV as well as large coherent oscillations in B_x and B_y, the overall distribution is likely to be a single Maxwellian and $\langle 2E \rangle$ would reflect the Maxwellian temperature of the two ropes in the background.

The overall picture of the energy in the ropes of Case 2 is summarized in Fig. 5.12. Assuming the 3 to 5 eV background oscillations is the behavior of the primary distribution which continue for the rest of the experiment, the plot of $\langle 2E \rangle$ can be separated into two components which

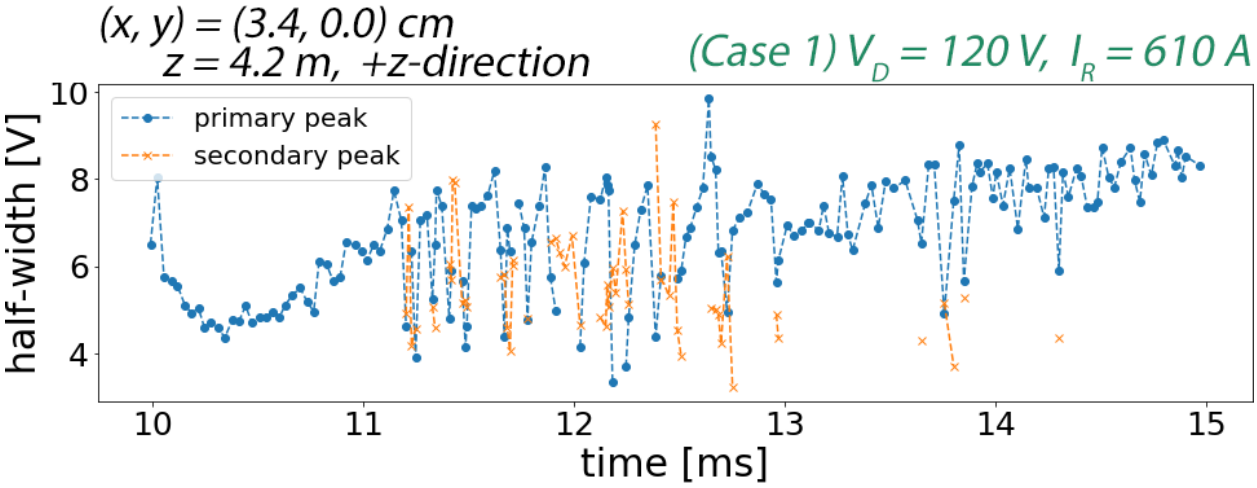

Figure 5.13: A plot of the half-width at half-maximum vs. time for the $+z$ direction in Case 1. The individual half-widths of the primary and beam distributions are plotted whenever possible. The half-width of the overall distribution is plotted otherwise.

contain the primary distribution (red line) and the streaks of increasing $\langle 2E \rangle$ due to the beam (green arrows). This is consistent with the 4 to 7 eV ion energy baseline formed by the single Maxwellian data points of Case 1 as the beam causes the average energy of the localized point to increase.

All in all, the presence of a beam increases the (kinetic) energy of the ions at the location of the ion energy analyzer. The beam is likely to be a consequence of magnetic reconnection as its appearance is highly correlated with the motion of the ropes, and magnetic reconnection is known to accelerate ions to higher energies. This implication is further explored in Chapter 6.

5.3.3 Comparing Widths of Primary and Beam Distribution

The width of a Maxwellian $f(v)$ distribution is proportional to the square root of the ion temperature $\sqrt{kT_i}$. Therefore, the standard deviation b in the bi-Maxwellian function (Eq. 5.2.1) can be used to estimate for the ion temperature. Here, it is important to note that the individual Maxwellians of (Eq. 5.2.1) depend on the discriminator voltage V (and the ion energy E) as opposed to the ion velocity v. This skews the abscissa such that b is not necessarily proportional

to $\sqrt{kT_i}$. (See comment on abscissa scaling in Appendix of Böhm and Perrin (1993).) Nevertheless, the relative magnitude of the widths of the beam and the primary distribution can still be compared using b. The goal of this calculation is to determine if heating is present when the beam appears.

Fig. 5.13 shows the plot of half-width at half-maximum vs. time for the $+z$ direction in Case 1. The half-width of both individual Maxwellians are plotted whenever a bi-Maxwellian is present, and the half-width of the overall distribution is plotted otherwise. The plot shows a strong correlation with average energy $\langle 2E \rangle$ of the single Maxwellian data points in Fig. 5.11a. However, unlike $\langle 2E \rangle$, the primary distribution and the beam are shown to have comparable half-widths between the range of 4 and 8 V. Their half-widths are also not correlated with the presence of the beam. This shows that when the beam appears, the ions are not as significantly heated as they are accelerated and most of the energy preferentially goes into increasing the ions' kinetic energy.

5.4 Ion Energy Analyzer Across the Magnetic Field

In previous sections, the average energy of the ions along the magnetic field was measured and a parallel ion temperature was estimated. The ions were expected to move straight into the energy analyzer as the magnetic field was aligned with the normal to the face of the entrance grid. However, when determining the perpendicular ion temperature, the gyration of the ions along the magnetic field have to be accounted for as the trajectory of the ions inside the energy analyzer would determine if the ion would be able to reach the collector. The effect of positioning the ion energy analyzer such that it faces a direction perpendicular to the magnetic field is thus investigated in this section.

The coordinate system for the analysis is shown in Fig. 5.14. The ion energy analyzer is simplified to an open, two-dimensional box that has a depth of $L = 5.2$ mm and an effective

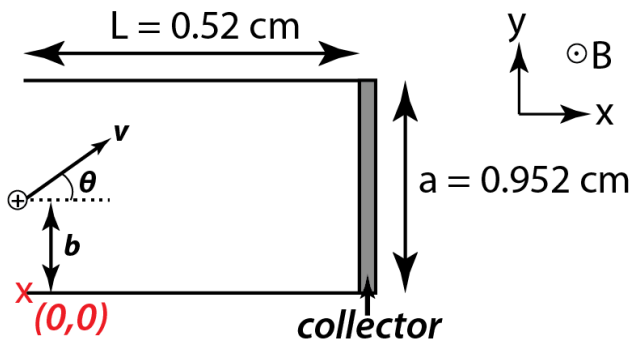

Figure 5.14: The coordinate system of the energy analyzer as it measures ions moving across the magnetic field. The figure is not drawn to scale.

opening diameter of $a = 9.52$ mm. The ions enter the energy analyzer with some velocity v and at some angle θ and a distance b with respect to the bottom edge of the energy analyzer. The direction of the magnetic field is out of the plane of the figure. Then, given the parameters v, θ and b, the trajectory of the ion is calculated to determine if the ion is able to reach the collector at the opposite end of the energy analyzer. The grids are assumed to be completely transparent to the ions and the potentials on the grids are ignored. It is also assumed that the ion does not move along the magnetic field in the z-direction.

Fig. 5.15 shows a plot of various ion trajectories for different values of b and θ. The dimensions are to scale. The trajectories were calculated with a magnetic field of $B_0 = 330$ G and the velocity is equivalent to the ion thermal velocity at 4 eV (i.e. $v = 9.8 \times 10^5$ cm/s). It is then observed that the ions will reach the collector under two conditions: (1) the ion gyroradius ρ_i has to be larger than than the depth of the energy analyzer L, and (2) the time of flight to the collector has to be shorter than the time of flight to reach the side walls. The time of flight to a given wall is infinite if the ion never makes it to the specified wall.

Using the two aforementioned conditions, the acceptable values of v and θ for a given b value can be visualized using a parametric plot as shown in Fig. 5.16. Each data point represents a triad of v, θ and b values which is colored yellow if the ion is able to reach the collector or purple if otherwise. Red lines drawn across the figure indicate benchmark velocity values. For example,

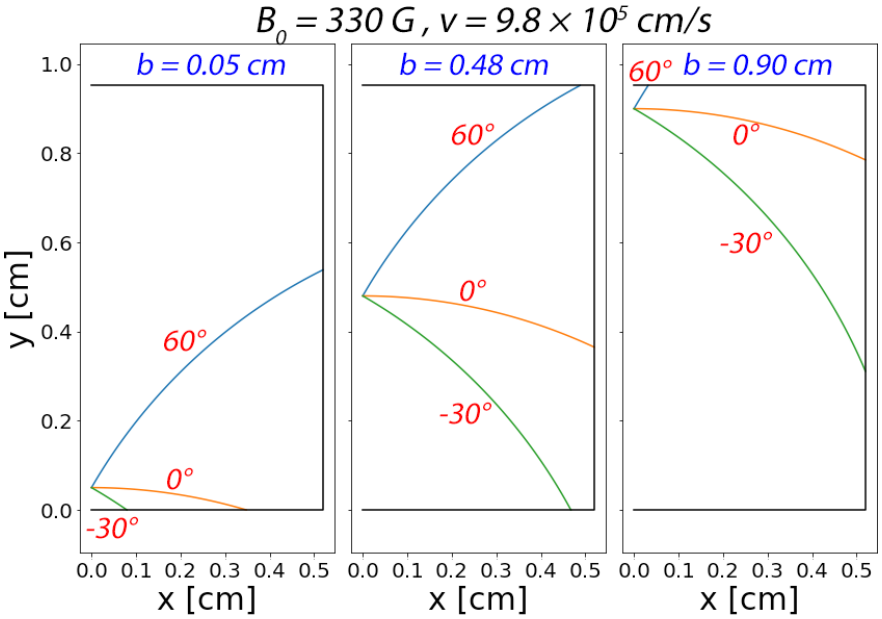

Figure 5.15: A plot of various ion trajectories drawn to scale for various starting positions b and θ. The magnetic field is in the $+z$-direction.

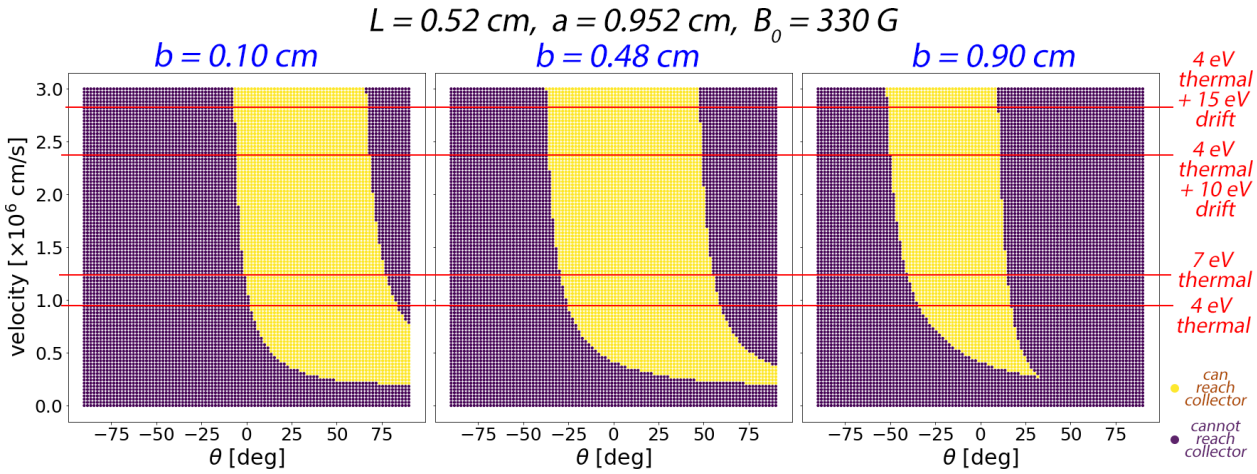

Figure 5.16: Plots of permitted v and θ values that allow the ion to reach the collector for various ion starting positions b. The v and θ values that allow the ions to reach the collector are in yellow, and are otherwise purple. The red lines indicate velocity values that are used as benchmarks.

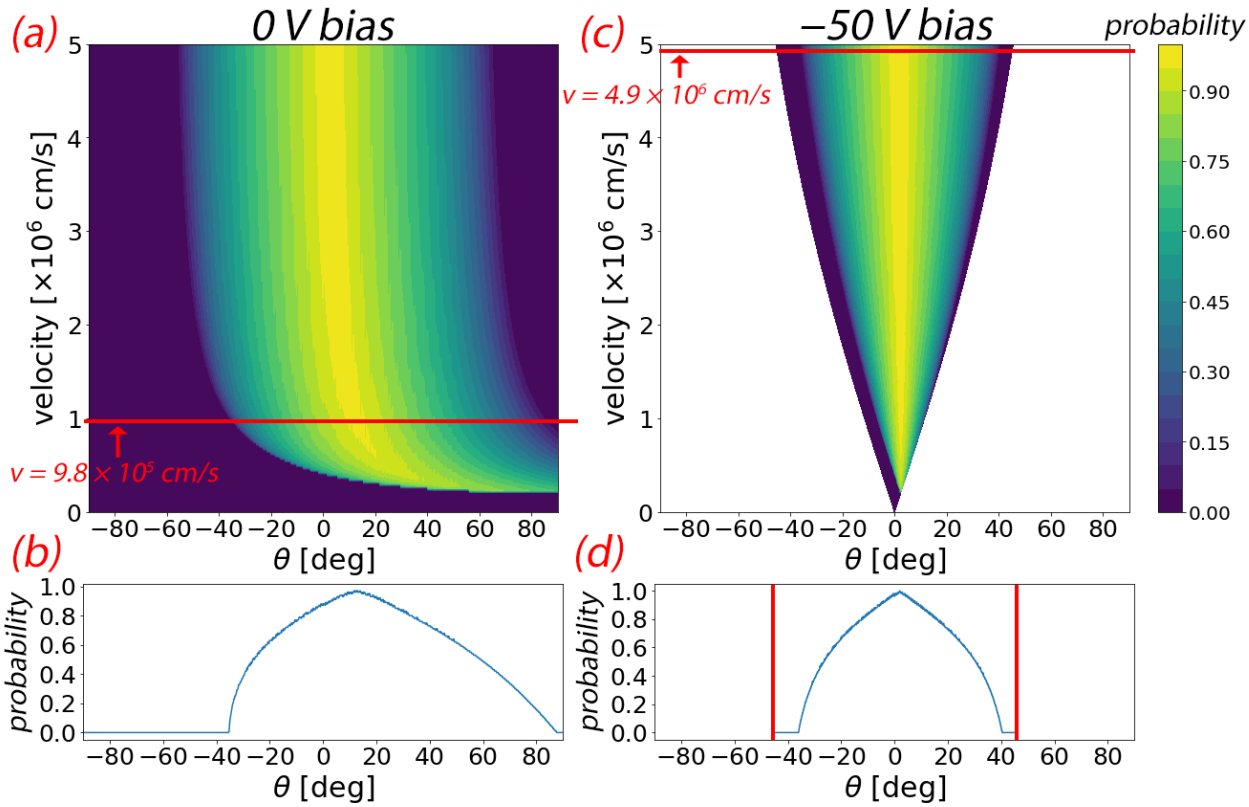

Figure 5.17: (a) The plot of the probability an ion would reach the collector for a given v and θ when the entrance grid has no bias. (b) The probability line profile for 4 eV thermal ions which have velocities of $v = 9.8 \times 10^5$ cm/s in the case of no entrance grid bias. (c) The plot of the probability an ion would reach the collector for a given v and θ when the entrance grid has a -50 V bias. (d) The probability line profile for 4 eV thermal ions which have velocities of $v = 4.9 \times 10^6$ cm/s after being accelerated by a -50 V entrance grid bias.

the bottommost line represents ions with a 4 eV thermal velocity while the topmost line is for 4 eV ions that have a 15 eV drift towards the ion energy analyzer. As the velocity of the ions increase, the range of permissible θ values start to converge.

The plots in Fig. 5.16 show that the energy analyzer generally favors ions that enter with a positive θ as the gyration of the ions are in the clockwise direction. In addition, the range of permissible θ values at a specific velocity depend on the starting position of the ion. For example, ions starting near the top of the energy analyzer ($b = 0.90$ cm) are more likely to reach the collector with a negative θ, and vice versa for ions with a positive θ near the bottom ($b = 0.10$ cm).

The probability of an ion reaching the collector p is defined by summing the number of times the ion reaches the collector over all possible values of b for a given velocity v and θ. This assumes that any starting position b is equally likely when an ion reaches the energy analyzer. The result is shown in a plot of the probability as a function of v and θ in Fig. 5.17a. The line profile of the probability as a function of θ for $v = 9.8 \times 10^5$ cm/s is shown in Fig. 5.17b. The ion energy analyzer has an angle of acceptance that is generally between -40° and 85°.

In the setup of the ion energy analyzer described in Chapter 5.1.2, a -50 V bias was applied on the entrance grid to improve the quality of the measured collector current. As ions are measured across the magnetic field, the -50 V accelerates ions into the energy analyzer and increases its starting velocity v while reducing θ. This means that each v and θ value in Fig. 5.17a can be mapped onto a different set of initial v and θ values that are bounded by a cone as shown in Fig. 5.17c.

The overall effect of the -50 V bias is that the angle of acceptance of the ion energy analyzer is increased. Ions that may not reach the collector by entering the energy analyzer with a large θ beforehand would now have a better chance of reaching the collector when the -50 V bias is applied. This can be quantified by comparing the probability line profile between the no bias case and the -50 V case at $v = 4.9 \times 10^6$ cm/s, the average velocity of the ions after a 50 V acceleration, in Fig. 5.17d. The line profile is more symmetric for the -50 V bias case with an expected θ value closer to 0° which suggests an improvement in the directional accuracy of the energy analyzer. The angle of acceptance is also reduced to between -40° and 40°. However, given that the range of θ values that would result a non-zero probability of reaching the collector now span a wider range of values, this also means that the ion energy analyzer is less precise in determining the direction of the ions when making measurements across the magnetic field.

5.5 Spectrometer Measurements

Spectroscopy is an alternative method of determining the ion temperature as it measures the broadening of the spectral lines corresponding to wavelengths of light emitted by the plasma. This is a non-contact measurement technique that can be operated concurrently with the ion energy analyzer and can serve as an independent diagnostic to verify the measurements of the ion energy analyzer. In this study, Doppler line broadening is the spectroscopic technique used to estimate the perpendicular ion temperature of the flux ropes.

5.5.1 Doppler Line Broadening

The spectrometer observes spectral lines from singly ionized helium (He^+) or He II. These spectral lines are assumed to be broadened primarily through Doppler broadening or from the shift in the observed wavelength due to the thermal motion of the ions. Other effects such as Stark broadening and the Zeeman effect are assumed to be negligible. The width of the spectral line thus depends on the ion temperature and can be determined from theory as follows (Griem 1997).

Consider non-relativistic ions moving with a velocity v, which can be positive or negative depending on the direction of the ions with respect to the detector. The Doppler shift of the frequency f due to motion of the ions is then

$$f = f_0 \left(1 + \frac{v}{c}\right) \ ,$$

where c is the speed of sound and f_0 is the frequency of the spectral line. Given the ions have a one-dimensional Maxwellian distribution

$$n(v)\ \mathrm{d}v\ = N\sqrt{\frac{m}{2\pi k T_i}}\exp\left(-\frac{mv^2}{2kT_i}\right) \ ,$$

the intensity of the observed spectra I would then be proportional to

$$\exp\left(-\frac{mv^2}{2kT_i}\right) = \exp\left(-\frac{m}{2kT_i}\frac{c^2(f-f_0)^2}{f_0^2}\right) \ .$$

Since a normal distribution with a standard deviation of σ has a full width at half-maximum of $2\sqrt{2\ln 2}\sigma$, it follows that the full width at half-maximum of the frequency normal distribution is

$$\Delta f = 2\sqrt{\ln 2 \cdot \frac{2kT_i}{m}\frac{f_0^2}{c^2}} \ ,$$

and in terms of the wavelength $\lambda = c/f$ where $\Delta f/f_0$ is small,

$$\boxed{\frac{\Delta\lambda}{\lambda_0} = 2\sqrt{2\ln 2\frac{kT_i}{mc^2}}} \ . \tag{5.5.1}$$

This relates the ion temperature T_i to the width of the spectral line $\Delta\lambda$. The equation can be further simplified for the flux rope experiment by substituting the mass of helium ions and converting the units to yield a numerical equation for the temperature in eV, which is

$$T_i \text{ [eV]} = \frac{kT_i}{e} = \frac{mc^2}{8\ln 2 \cdot e}\left(\frac{\Delta\lambda}{\lambda_0}\right)^2 \approx 6.74\times 10^8\left(\frac{\Delta\lambda}{\lambda_0}\right)^2 \ . \tag{5.5.2}$$

5.5.2 Setup

The experiment was performed on the flux ropes in Case 2 (see Table 5.1). The experimental setup used to measure the flux rope spectra is shown in Fig. 5.18. In this setup, the main apparatus is a Model 209 Czerny–Turner Monochromator from McPherson Instruments that uses a diffraction grating of 2400 grooves/millimeter and has a resolution of 0.005 nm. It is mounted on an anti-vibration table to reduce unwanted mechanical vibrations and placed in a dark room to avoid noise from stray ambient lighting.

A fiber optic cable connects the spectrometer to an optical port with a window of quartz on

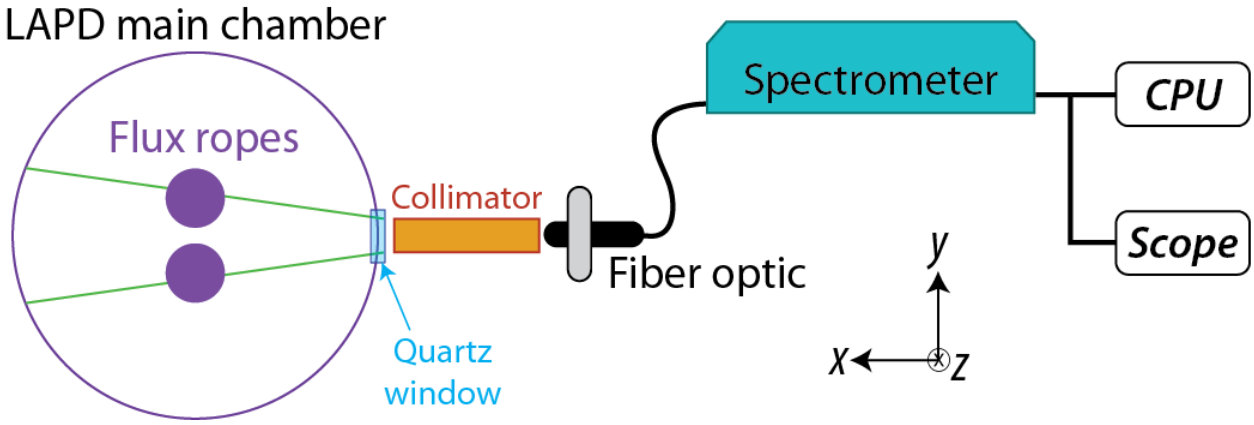

Figure 5.18: Experimental setup to measure the line-of-sight ion temperature across the flux ropes using a spectrometer.

the side of the LAPD. The quartz provides a vacuum seal on the machine and is also transparent to both UV and visible light, which makes it ideal for measuring He II lines that are close to ultraviolet wavelengths ($\lambda = 225$–450 nm). Light from the flux ropes are collimated with a rectangular cardboard box tube that is used to narrow the field of view of the fiber optic. The box has opening dimensions of 10 cm $\times$ 3 cm and its interior surfaces are painted black to reduce reflectivity.

The spectrometer is connected to a computer and an oscilloscope to collect data. The computer primarily controls the internal motors that changes the orientation angle of the diffraction grating. This allows the wavelength of light to be precisely controlled in step sizes of 0.1 Å ($= 0.01$ nm). In addition, the computer interfaces to the scope and collects the output from the spectrometer's phototube as a function of time. This is done with a Python routine that stores the output data in a HDF5 file.

The spectrometer is triggered by the plasma discharge and records photons emitted for the entire flux rope experiment. In this setup, the spectrometer measures the He II line at 320.3 nm which corresponds to the $n = 5 \rightarrow n = 3$ transition of the helium fine structure (Kramida and Ralchenko 1999). Since the intensity of the He II spectra is typically very low (about 6 photons per shot), the spectrometer has to accumulate photons from multiple shots to create a single

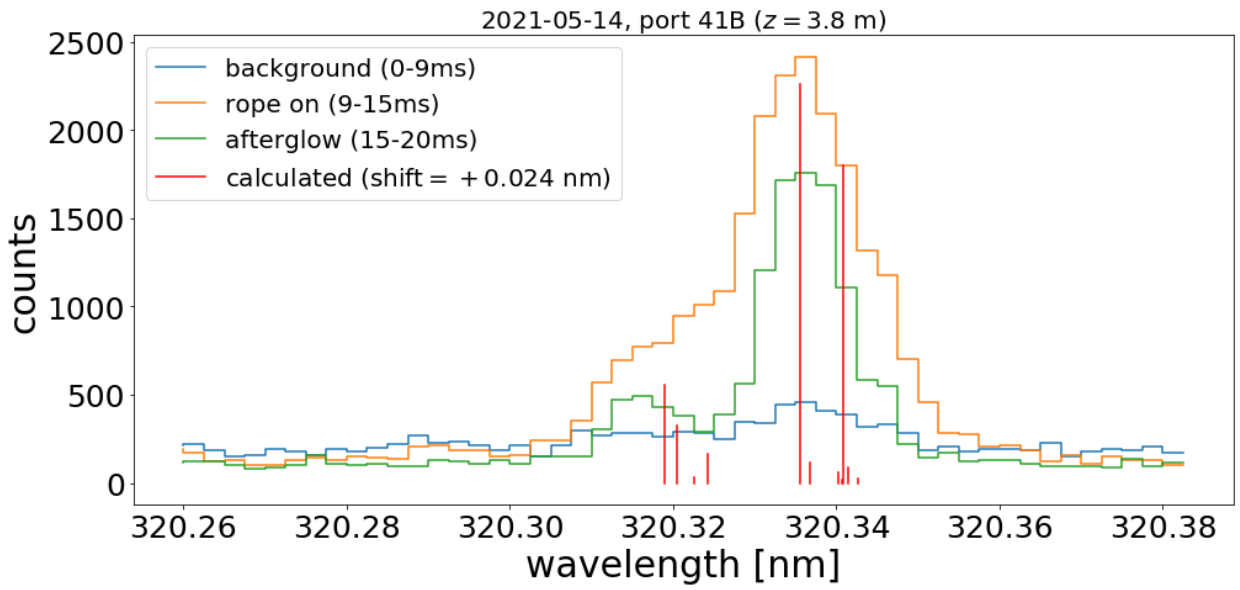

Figure 5.19: The photon count vs. wavelength plots of the He II spectral line at 320.3 nm as measured by the spectrometer. The blue, orange and green lines correspond to the aggregated photon count at three different phases of the plasma discharge. The red spectra is calculated from the fine structure of helium and then redshifted to account for instrumental error.

data point for each wavelength.

5.5.3 Results & Discussion

Fig. 5.19 shows a plot of the photon count against the observed wavelength λ for the range $320.260 \leq \lambda \leq 320.385$ nm and with step size $\Delta\lambda = 0.0025$ nm (50 steps). Each data point for the photon count was summed over 400 shots of the plasma discharge, and the data run took about 20 hours to complete.

The spectrometer collected photons for 20 ms at the start of each discharge cycle and binned them into three different time periods: the discharge of the background plasma (0–9 ms, blue), when the flux ropes are present (9–15 ms, orange) and during the afterglow immediately after the plasma is shut off (15–20 ms, green). The photon count for each of these time periods was then plotted as a function of wavelength in Fig. 5.19. Each of these plots has two distinct peaks: a large primary peak near 320.335 nm and a small secondary peak near 320.315 nm. These peaks

appear to correspond to the two clusters of spectral lines created by the $5 \rightarrow 3$ transitions at 320.3 nm, which is shown in red and calculated based on the theoretical values of the energy levels within the fine structure of helium (Okazaki and Andō 1968). In addition, these calculated spectral lines were redshifted by the $+0.024$ nm such that they align with the photon count vs. wavelength plots. This verifies that the photons are from the $5 \rightarrow 3$ transition and accounts for a hysteresis effect within the spectrometer's motorized probe drives that would randomly shift the wavelength of the entire plot by a small amount (< 0.1 nm) and create an instrumental error.

The close proximity of the spectral lines makes it difficult to resolve and determine the width of the individual spectral lines to obtain a value of the ion temperature. However, given that the wavelength and intensity of the individual spectral lines are known from theory, a theoretical line-broadened spectra was constructed by assuming all lines are Gaussians and their widths are calculated by taking the inverse of (Eq. 5.5.2) and substituting the expected T_i value into the equation. The theoretical line spectra was then scaled and translated to fit the intensity vs. wavelength plots. This was used to determine the best T_i that would fit the data.

Fig. 5.20 shows the best-fitting theoretical, line-broadened spectra superimposed on each of the individual intensity vs. wavelength plots in Fig. 5.19. Each component spectral line was fitted to a Gaussian of the form

$$A_0 \exp\left(-\frac{(\lambda - \lambda_0 - \lambda_1)^2}{2\sigma^2}\right) + c \ , \tag{5.5.3}$$

where A_0 and λ_0 are respectively the relative intensity and wavelength of the original spectral line obtained from Okazaki and Andō (1968), λ_1 is the instrumental error horizontal offset, σ is the width of the Gaussian as a function of T_i determined by taking the inverse of (Eq. 5.5.2), and c is the baseline of the spectra. These values are shown in the plot legend at the top left corner of each plot.

The values from the best fit parameters suggest that the ion temperature of the background

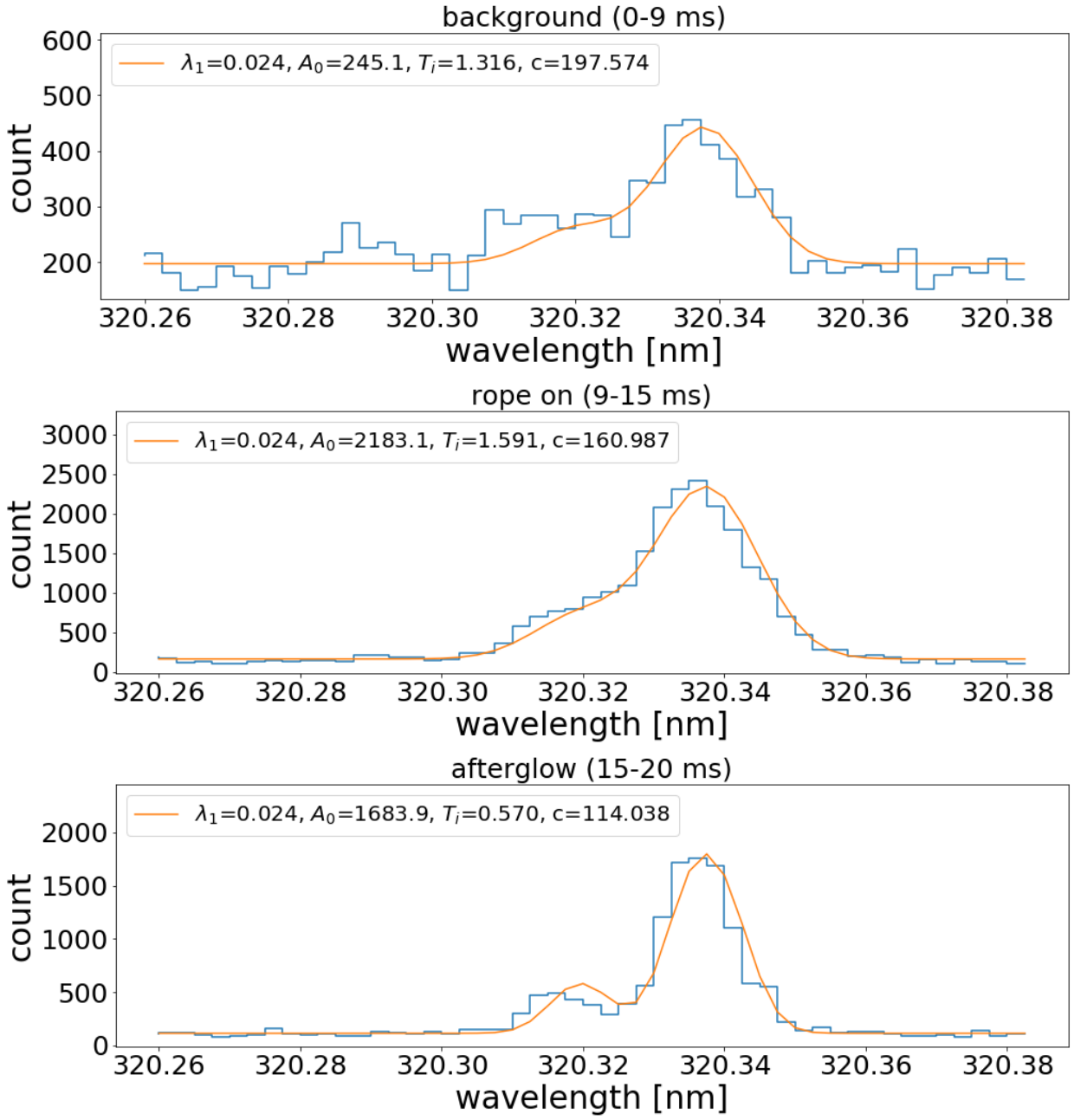

Figure 5.20: The individual photon count vs. wavelength plots (in blue) fitted to the theoretical, line-broadened spectra (in orange). The fit parameters (Eq. 5.5.3) are shown in the plot legend. T_i determines the line-broadening for each of the theoretical spectral lines.

plasma (0–9 ms) is 1.3 ± 0.3 eV. The temperature increases to 1.59 ± 0.08 eV when the flux ropes are turned on (10–15 ms) and then falls to an average of 0.57 ± 0.04 eV in the afterglow where the plasma is off. The overall temperature trend is consistent with heating of the plasma by the LaB_6 cathode. However, the overall line-of-sight temperature of the ropes are at least 3 to 4 eV lower than the ion temperature estimated from the average energy $\langle 2E \rangle$. This discrepancy is due to volume averaging of the ion temperature over a large region of space and can be demonstrated empirically with a source of known ion temperature placed in front of the spectrometer. This, however, requires knowledge of the spectrometer's field of view.

5.6 Empirical Determination of Observed Spectrometer T_i

The observed spectra of the spectrometer is highly dependent on the field of view of the fiber optic, which is the maximum volume the fiber optic samples when collecting incoming photons from the plasma. A large field of view reduces the precision of the ion temperature measurement as photons are sampled from a wider variety of positions. Thus, an significant increase in the ion temperature at a localized point is likely to be diluted by the temperature measurements from the other areas the spectrometer is sampling.

An estimate for the spectrometer's observed ion temperature was determined from the spectrometer's angular field of view, which is the intersection of the field of views of both the fiber optic and the collimator. By measuring the volume of the flux ropes within the spectrometer's field of view and then estimating the temperature of the ropes, a position-weighted average of the ion temperature is determined.

5.6.1 Setup to Determine Field of View

Fig. 5.21 shows the setup to measure the spectrometer's field of view. A fiber optic fitted with an improvised collimator made of cardboard is shown on the left, while a light-emitting diode (LED)

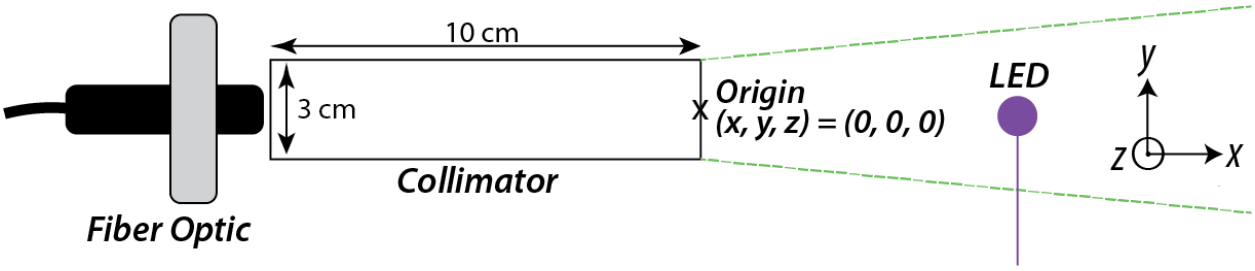

Figure 5.21: The experimental setup to determine the field of view of the spectrometer.

mounted on a stand is shown on the right. The origin is defined with respect to the center of the collimator's opening edge and the coordinate system is shown. The LED acts as a source of light that mimics the photon emission of the flux ropes and has a wavelength of about 400 nm, which is close to the wavelength of light emitted by the He II line (320.3 nm). The light on the LED is then made to diffuse by applying a blob of vacuum grease on the LED, and then pulsed with a 1 kHz square wave so that signal can be observed and measured on an oscilloscope.

5.6.2 Intensity Plane Measurements

The observed intensity of the LED was measured for points on a yz-plane, the plane that is perpendicular to the front face of the fiber optic. Data was taken at four yz-planes with different x-coordinates ($x = 31$, 49, 59 and 71 cm) and the results of each plane are shown in Fig. 5.22. Each dot represents a single measurement and the transparency of each point was normalized to the maximum intensity, with the darkest being the most intense. Data points with intensities below the background level, which were determined by measuring the intensity value when the LED was off, are not plotted. All the axes are plotted to the same scale.

The data points in Fig. 5.22 can be grouped within boundaries that have shapes corresponding to the field of views of the fiber optic and the collimator. For example, all the data points within each of these data planes appear to be bound by the green rectangle, which is the shape of the collimator opening. For data points that have a noticeably higher intensity than the rest of the plot, they can be fitted into a red circle which is the shape of the fiber optic cable. The

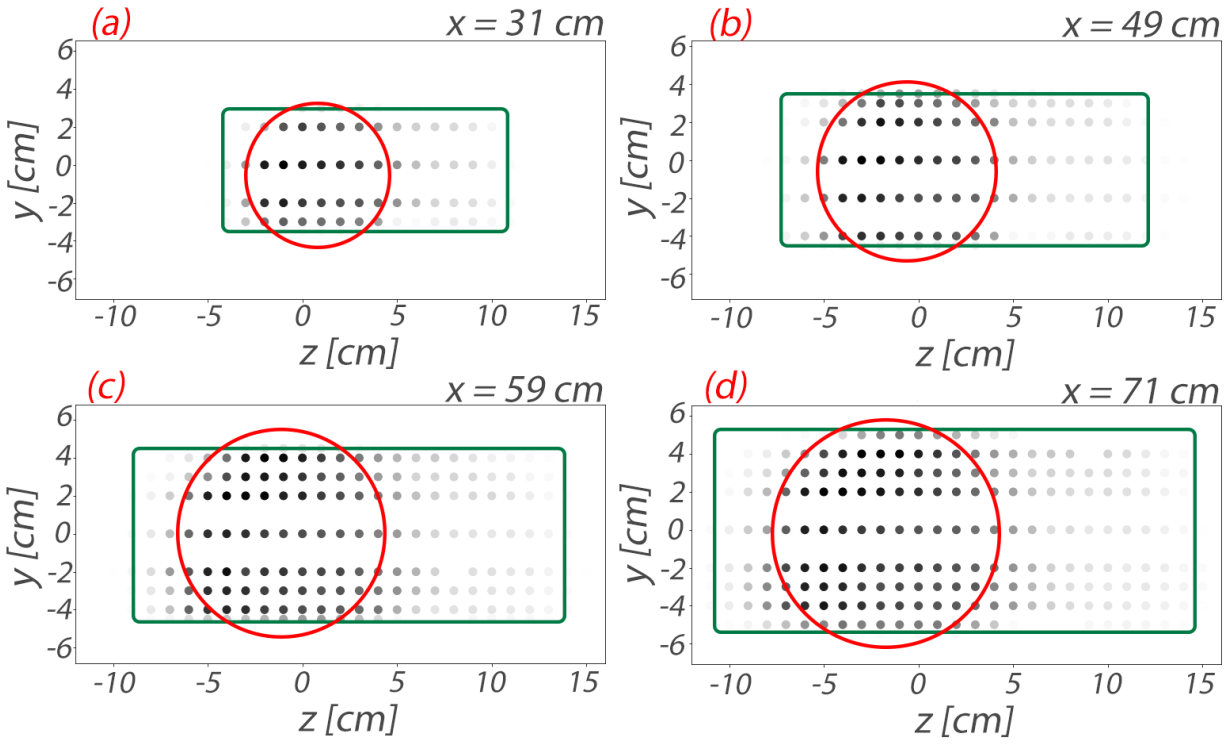

Figure 5.22: Four yz-planes of data points mapping the measured root-mean-square intensity of the LED at various location. The darker the data point, the higher the measured intensity. Almost all the plotted the data points fit within the green rectangle, which is likely to be boundary of the field of view of the collimator. The data points within the red circles have higher intensities than the rest of the data and are likely to be within the field of view of the fiber optic.

points outside the red circle are expected to be from light that is scattered off the interior of the collimator before entering the fiber optic.

The dimensions of the red circle and green rectangle become smaller as measurements are made closer to the fiber optic. This is in line with a field of view that converges towards the opening of collimator and fiber optic, which is positioned at $x = -10$ cm.

5.6.3 Field of View Reconstruction

The field of view of the spectrometer was determined by locating the edge coordinates of the field of views in each of these yz-planes, and then using linear regression to obtain a line of best fit that represents a projection of the field of view boundary onto the xy- and xz-planes. This is shown in Fig. 5.23, where the red lines are constructed with the points on the red circle and the green lines from points located on the green rectangle.

Fig. 5.23a and Fig. 5.23b are the estimated side and top-down projections of the spectrometer's field of view. The region shaded in green is the field of view of the collimator, while the region in red is that of the fiber optic. In Fig. 5.23a which shows the side view (xy-plane), these two regions overlap as the field of view of the collimator limits the field of view of the fiber optic.

As a check for consistency in the data, the edges of the field of view lines have to converge at $x = 0$ cm, which is the opening of the collimator. The dimensions are 3 cm high (in y) and 10 cm wide (in z). This agrees with Fig. 5.23a, but it is smaller in Fig. 5.23b. The discrepancy is due to a poor estimation of the cutoff region for the left and right sides of the green rectangular region, which does not have a clear cutoff boundary as compared to its top and bottom.

5.6.4 Estimation of Observed Ion Temperature

The flux ropes are now superimposed on the field of view from the side as shown in Fig. 5.23a. This assumes the ropes are invariant along z so that a volume estimation now simplifies to a

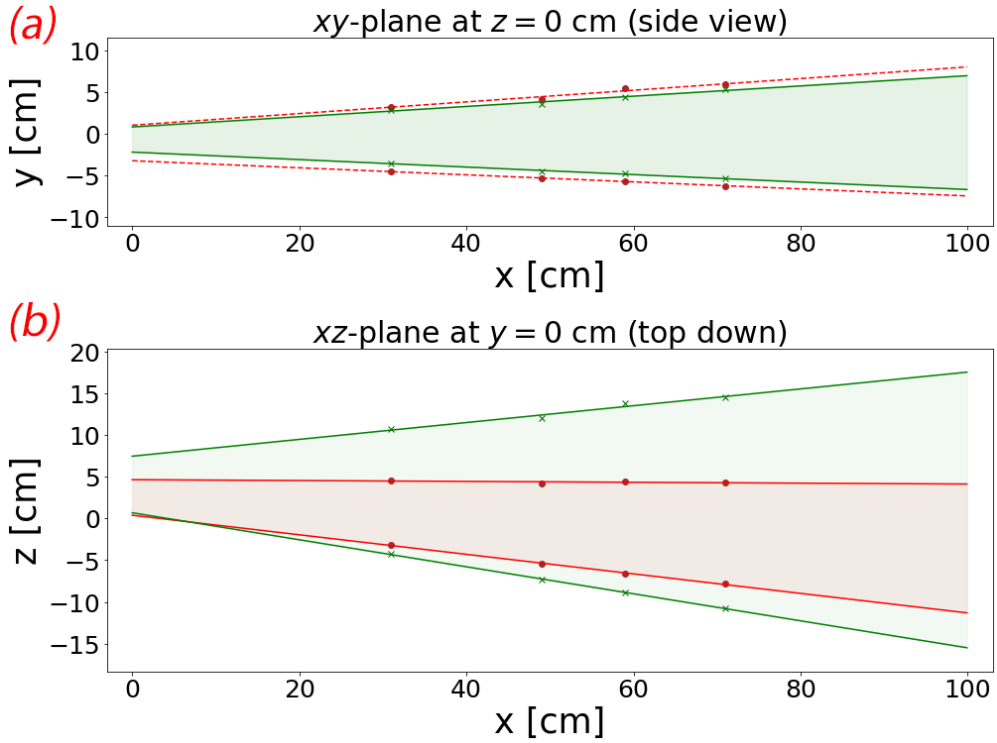

Figure 5.23: Plane projections of the field of view measurements on (a) the xy-plane or as seen from the side, and (b) the xz-plane or as seen from a top-down view. The red and green points are coordinate measurements made from yz-planes. Linear regression was used to determine the line edges. The green shaded region is the estimate for the collimator's field of view, while the red region is the estimate for the fiber optic. In (a), the collimator limits the field of view of the fiber optic.

cross-sectional estimation using the xy-plane. Then, in estimating the spectrometer's observed ion temperature (denoted by $\bar{T}_i$), each point of the flux rope is assumed to emit photons with a specific energy. The observed $\bar{T}_i$ is the aggregated, expected ion temperature from all the collected photons.

Fig. 5.24a shows a scale drawing of the LAPD cross-section ($z = 1.28$ m) with contours of the perpendicular current J_z superimposed. This figure shows the geometry of the system under consideration. Assuming the energy of the ions have a spatial distribution that is identical to J_z, energy values may then be assigned to each of these points in the plane. A peak energy of 6 eV is selected based on the estimated $\langle 2E \rangle$ value of the ropes in Fig. 5.11c. This chosen peak energy value affects the final value of $\bar{T}_i$.

Fig. 5.24b shows the final configuration used for the calculation of $\bar{T}_i$. The spectrometer's field of view is superimposed on the contour plot of the assigned energy values and data points that fall within the spectrometer's field of view are colored and filled. In addition, only values above 0.5 eV were averaged in the calculation to account for the minimum resolution that can be resolved by the spectrometer as data points below this threshold level would not be detected and make a contribution to $\bar{T}_i$.

The resulting plot of $\bar{T}_i$ is shown in Fig. 5.25, which is plotted as function of time and the steady-state value in the presence of the flux ropes oscillates at approximately 1.6 to 1.8 eV. This value agrees with the 1.59 ± 0.08 eV measured by the spectrometer during the same period of time. The consistency of the observed $\bar{T}_i$ with the spectrometer value demonstrates the feasibility of the volume averaging effect by the spectrometer and supports the data measured by the ion energy analyzer.

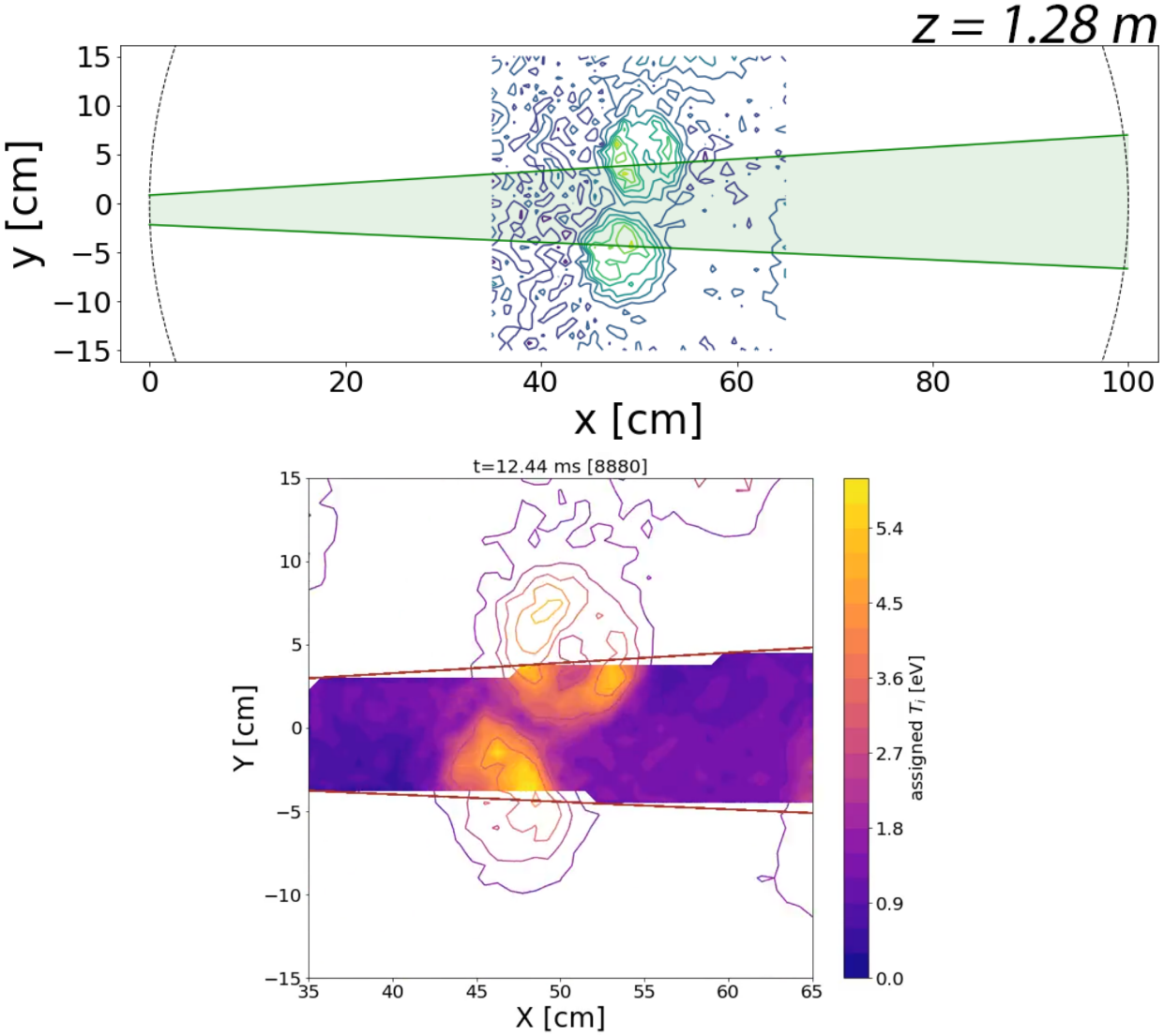

Figure 5.24: (a) A scale drawing of the LAPD cross-section showing the field of view of the spectrometer and the position of the flux ropes. The field of view of the spectrometer is indicated by the green region while the position of the flux ropes are indicated by the line contour plot of the perpendicular current J_z. The ropes are 1.28 m away from the plasma source. (b) A contour plot of the assigned energy values that uses the profile of J_z and the peak value of 6 eV from the baseline T_i of $\langle 2E \rangle$. Data points that contribute towards the spectrometer observed $\bar{T}_i$ are filled and colored.

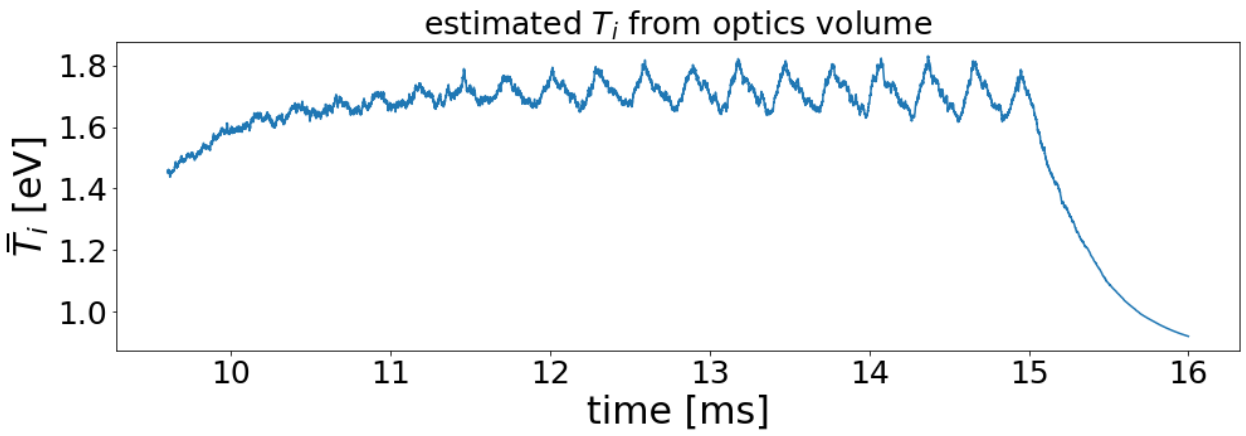

Figure 5.25: The calculated time-dependence of $\bar{T}_i$, the spectrometer volume-averaged ion temperature. The flux ropes are turned on at 9 ms. At $t = 11$ ms, $\bar{T}_i$ begins to oscillate at the kink frequency ($f = 3.2$ kHz) between 1.6 and 1.8 eV. The plasma shuts off at $t = 15$ ms.

5.7 Summary

In this chapter, measurements from the ion energy analyzer were presented. The ion energy distribution function was obtained by smoothing and differentiating the plot of the collected current I vs. the discriminator grid voltage V, and the resulting curves were fitted to single and bi-Maxwellian functions. The bi-Maxwellian functions indicate the presence of a beam with a drift of 10–15 eV that was frequently observed as the ropes oscillate. These drifts correspond to ion thermal speeds of up to 1.9×10^6 cm/s.

The parallel ion temperature was estimated using the average energy $\langle 2E \rangle$ which involves integrating spliced distribution functions that measured the ion's energy in opposite directions along the same axes. In plots of $\langle 2E \rangle$ vs. time, the presence of a beam was associated with a rise in the kinetic energy of the ions which typically had an average energy of above 8 eV. The ropes would otherwise have base levels of energies between 4 to 6 eV, which was estimated to be the ion temperature of the ropes. In addition, the beam does not heat the ions as the widths of the primary and beam distribution are shown to be comparable with no significant correlation to the presence of the beam.

The ion energy analyzer is less precise when measuring the perpendicular ion temperature, especially when a -50 V bias is applied on the entrance grid. This is due to an increase in the angle of acceptance even though the quality of measurements have significantly improved.

A spectrometer was then used to measure the line-of-sight ion temperature for the flux ropes in Case 2. The spectrometer measured the Doppler line broadened He II lines at 320.3 nm and estimated an perpendicular ion temperature of 1.59 ± 0.08 eV due to a volume averaging effect of the spectrometer's field of view. This value was found to be consistent with an empirical calculation of the observed ion temperature that uses the flux rope profile of J_z and a typical average energy ($\langle 2E \rangle = 6$ eV) from the ion energy analyzer to obtain an ion temperature that oscillates between 1.6 and 1.8 eV.

Chapter 6

Ion Distribution Functions in a Reconnecting Plasma

The measurements presented in Chapter 5 show that the average energy $\langle 2E \rangle$ is strongly correlated with the magnetic field of the ropes. This is likely to be caused by magnetic reconnection, a process known to convert energy stored in the magnetic fields into kinetic and thermal energy of the ions. In this chapter, the relationship between the beam of ions that appear in the bi-Maxwellian distribution function and magnetic reconnection is investigated. The presence of the beam indicates the presence of ion acceleration and signs of reconnective activity has to occur with the beam in order to establish a positive correlation between the two.

6.1 The Distribution Function in Two-Dimensions

6.1.1 Visualizing Anisotropy with Polar Plots

Polar plots have been used to observe anisotropy in the ion velocity distribution function for plasmoids and flux rope-like structures in the Earth's magnetosphere where they are abundant Hoshino et al. (1998). Some of these ions were non-Maxwellian and have thermalization timescales that

were longer than the reconnection time. They were shown through numerical simulations to change the magnetic structure of the reconnection site and reduce the efficiency of magnetic energy release as compared to Maxwellian ions.

In a similar manner, polar plots of the ion distribution function may be constructed for the two flux rope experiment using $f_z(E)$ and $f_y(E)$, the distribution functions along and across the magnetic field respectively. The polar plot can be loosely interpreted as the two-dimensional distribution function and is useful as a visualization tool to determine the anisotropy of the data at a specific instant in time.

The data for the polar plot is constructed by first plotting $f_z(E)$ along the abscissa and $f_y(E)$ along the ordinate. The $f_y(E)$ distribution function is then scaled such that $f_y(0) = f_z(0)$ and then normalized to the maximum $f_z(E)$ value of the entire dataset. The distribution function along some arbitrary angle θ is then calculated using a linear interpolation scheme which is expressed as

$$f(E,\theta) = f_0 + \theta \cdot (f_1 - f_0) \ , \tag{6.1.1}$$

where E and θ are the radial and angular coordinates of the polar plot respectively, and f_0 and f_1 are the distribution functions bounding each quadrant, i.e.

$$(f_0,\ f_1) = \begin{cases} (f_{z+}(E),\ f_{y+}(E)) & \text{for } 0 \leq \theta < \frac{\pi}{2} \ , \\ (f_{y+}(E),\ f_{z-}(E)) & \text{for } \frac{\pi}{2} \leq \theta < \pi \ , \\ (f_{z-}(E),\ f_{y-}(E)) & \text{for } \pi \leq \theta < \frac{3\pi}{2} \ , \\ (f_{y-}(E),\ f_{z+}(E)) & \text{for } \frac{3\pi}{2} \leq \theta < 2\pi \ . \end{cases}$$

Although there exist other interpolation schemes that can improve the finesse of the polar plot and have properties such as shape-preservation (Williamson and Rasch 1989), the interpolated

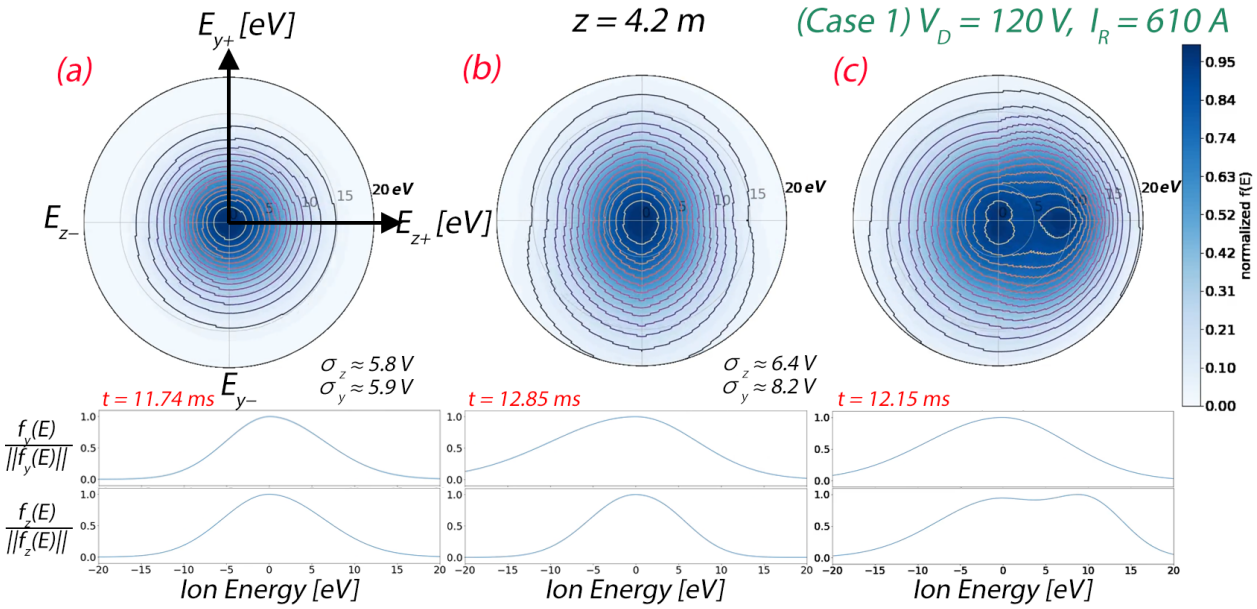

Figure 6.1: Polar plots of the two-dimensional distribution function and their corresponding $f_y(E)$ and $f_z(E)$ plots for Case 1 at three different times. All three contour plots are normalized with respect to each other and use the same color scale. The line profiles of $f_y(E)$ and $f_z(E)$ are normalized such that their peak amplitudes are equal to 1.

values of $f(E, \theta)$ are purely speculative and intended to guide the eye of the viewer. Thus, linear interpolation was found to be sufficient and was chosen for ease of implementation.

Fig. 6.1 shows some examples of the polar plots and their corresponding $f_y(E)$ and $f_z(E)$ line profiles at different times. The line profiles are normalized such that the peak amplitude of each plot is 1. The coordinate system is shown in Fig. 6.1a, which is a typical distribution function obtained when the ropes are not colliding. The polar plot appears as a circular island symmetric in both y and z. The plot can be fitted to a Maxwellian that has an width of 5.9 V, which estimates the ion temperature of the ropes as there are no drifts along any of the y and z directions.

Fig. 6.1b and Fig. 6.1c are polar plots with anisotropic distribution functions. In Fig. 6.1b, the ions across the magnetic field ($\sigma_y = 8.2 \pm 0.7$ V) have higher energies as compared to ions along the magnetic field ($\sigma_z = 6.3 \pm 0.1$ V). This produces a polar plot that is wider along y as compared to z. In addition, it may be noted that the shape of the polar plot is not completely

smooth on the axis with the shorter width. This is due to the non-shape-preserving nature of the linear interpolation.

In contrast, Fig. 6.1c shows a polar plot that contains a beam in the $+z$ direction at $E_z = +10$ eV. The beam drifts at a velocity of $v_{th} = 1.55 \times 10^6$ cm/s and creates a smaller bubble to the right of the primary distribution in the polar plot. This is a makes a suitable visual indicator to show that a beam is present and is moving in a specific direction at a given time.

6.1.2 Time Evolution in the Presence of the Beam

Fig. 6.2 demonstrates how a polar plot is used to visualize the time evolution of the distribution function and the development of a beam in a single cycle of the flux rope oscillation. The time interval ($t = 12.53$ to 12.78 ms) is marked by the red parallel lines in Fig. 6.2a and is overlaid on a reproduction of Fig. 5.11a. This interval is approximately the period of one flux rope oscillation ($f = 3.9$ kHz).

The polar plots of the ion distribution function is shown in Fig. 6.2b. The time interval between each plot is $\Delta t = 0.05$ ms. The distribution function begins as a Maxwellian distribution where the width in both y and z directions are almost identical, and maintains its shape for about 0.1 ms. A small amount of heating may be present as the polar plot contours grow and the average width increases from 5.7 to 6.1 V. However, heating may or may not be present as the error of these values are approximately ± 0.5 V, which is estimated from the potential step size of the I-V curve.

At $t = 12.63$ ms, the distribution function no longer Maxwellian as the distribution function becomes asymmetric. A beam then emerges in the $+z$ direction at $t = 12.68$ ms with an energy of about 13 eV, creating a second bubble to the right of the primary distribution. The line profiles of $f_y(E)$ and $f_z(E)$ are shown in Fig. 6.2c and $f_z(E)$ clearly shows a bimodal distribution. The width of $f_y(E)$ is larger than the width of $f_z(E)$ which results in a figure-of-eight pattern of the primary distribution. At $t = 12.73$ ms, the energy of the beam drops to 10 eV. Two contour

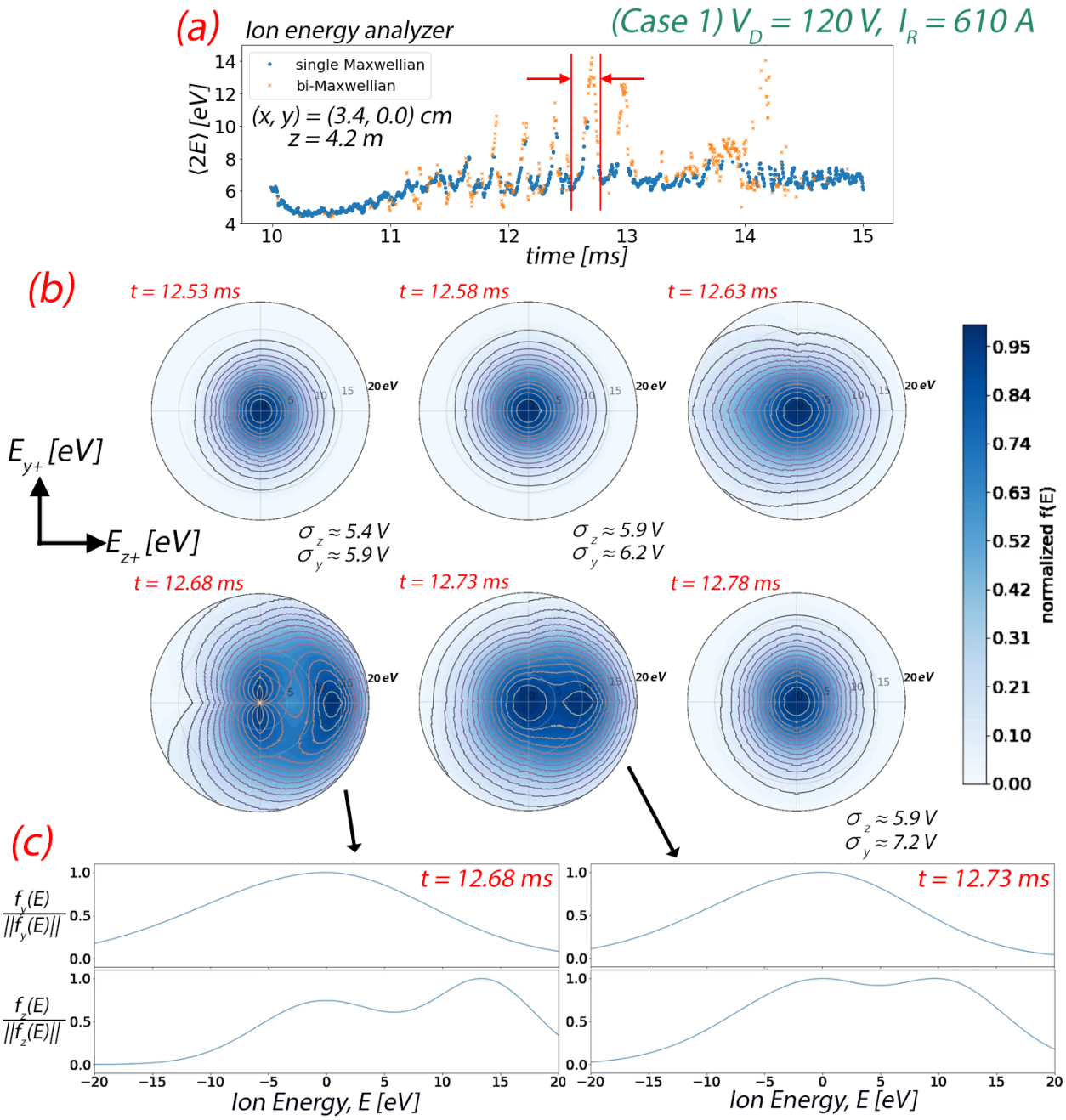

Figure 6.2: Time evolution of the two-dimensional distribution function for a time interval ($t = 12.53$ to 12.78 ms) which contains an average energy spike. (a) A reproduction of Fig. 5.11a, which is a plot of $\langle 2E \rangle$ as a function of time. The time interval of interest is marked by the red parallel lines. (b) Polar plots of the 2D distribution function with a time difference of $\Delta t = 0.05$ ms between adjacent plots. (c) Normalized line profiles of $f_y(E)$ and $f_z(E)$ at $t = 12.68$ and 12.73 ms.

bubbles can still be observed in the polar plot indicating that the beam is still present.

Finally at $t = 12.78$ ms, the beam disappears and the shape of the distribution function returns to an ellipse. As the width of $f_y(E)$ is observed to be consistently larger than $f_z(E)$ during this time interval, it appears that the ions moving across the magnetic field have a higher temperature than the ions moving along the magnetic field. Nevertheless, the disappearance of the beam marks the end of the oscillation cycle and the entire cycle repeats itself at other times between $t = 11.7$ and 13.3 ms. The beam usually appears at the peak of each $\langle 2E \rangle$ spike with a drift that is between 9 and 15 eV ($v_{Ti} = 1.5$–1.9×10^6 cm/s). This, together with the data presented in Chapter 5, suggest that the beam is highly correlated with the magnetic field of the ropes, increases the overall average energy of the system and is very likely to be associated with magnetic reconnection.

6.2 Correlation with Magnetic Reconnection

6.2.1 The Magnetic Vector Potential A_z

The correlation of the beam with magnetic reconnection can be further established by studying the magnetic field geometry of the ropes as a function of time when the beam appears. A typical geometry of the three-dimensional field lines of the two flux ropes is shown in Fig. 6.3, where multiple X-points are observed in the region between the two ropes with a position that varies along z. However, these field lines cannot be directly compared with the data from the ion energy analyzer as the data presented in Fig. 6.3 is from an earlier study (Gekelman et al. 2010).

Fortunately, a few planes of magnetic field data was taken together with data from the ion energy analyzer. Although there is insufficient data to reconstruct three-dimensional magnetic field lines, the xy magnetic field data planes can be used to construct two-dimensional line contours of magnetic vector potential A_z. These A_z line contours serve as a guide to indicate the probable position of the reconnection site and to observe its temporal evolution to determine

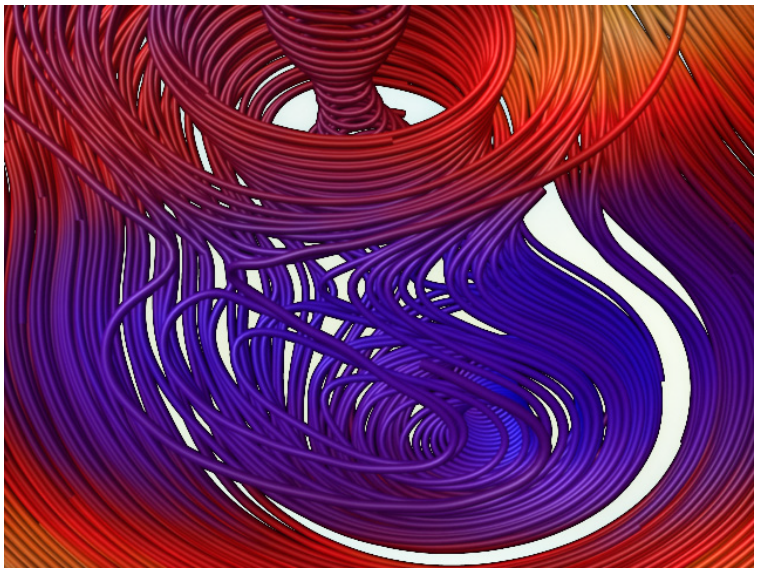

Figure 6.3: A three-dimensional plot of the magnetic field lines of two flux ropes ($d = 2.6$ cm, $V_D = 100$ V, $I_R = 30$ A) at $z = 6.6$ m. Multiple X-points are shown along the length of the rope which are potential sites for magnetic reconnection. Reproduced from Figure 9 of Gekelman et al. (2010).

the reconnection timeline. It is important to note that using A_z inherently assumes the field lines are invariant along z, but it is clearly not the case as observed in Fig. 6.3.

The value of A_z is calculated from the perpendicular current density J_z (derived from $\nabla \times B$) using

$$A_z = \frac{\mu_0}{4\pi} \int \mathrm{d}\boldsymbol{r}' \, \frac{J_z(\boldsymbol{r}', t')}{|\boldsymbol{r} - \boldsymbol{r}'|} \ , \tag{6.2.1}$$

where $\boldsymbol{r}$ and $\boldsymbol{r}'$ are the distances to the observation and source point respectively. This was calculated using the magnetic field plane closest to the ion energy analyzer in Case 2 and the results are summarized in Fig. 6.4. For convenience of annotation, the plots of $\langle 2E \rangle$ from Fig. 5.11c and the magnetic field components B_x and B_y from Fig. 5.11d are reproduced in Fig. 6.4a.

Fig. 6.4b are planes of A_z calculated for the time interval $t = 13.15$ to 13.20 ms, which are indicated by the red parallel lines in Fig. 6.4a. The value of J_z was calculated for the time indicated at the top right corner of each frame. Within each frame, the two flux ropes are visible but the

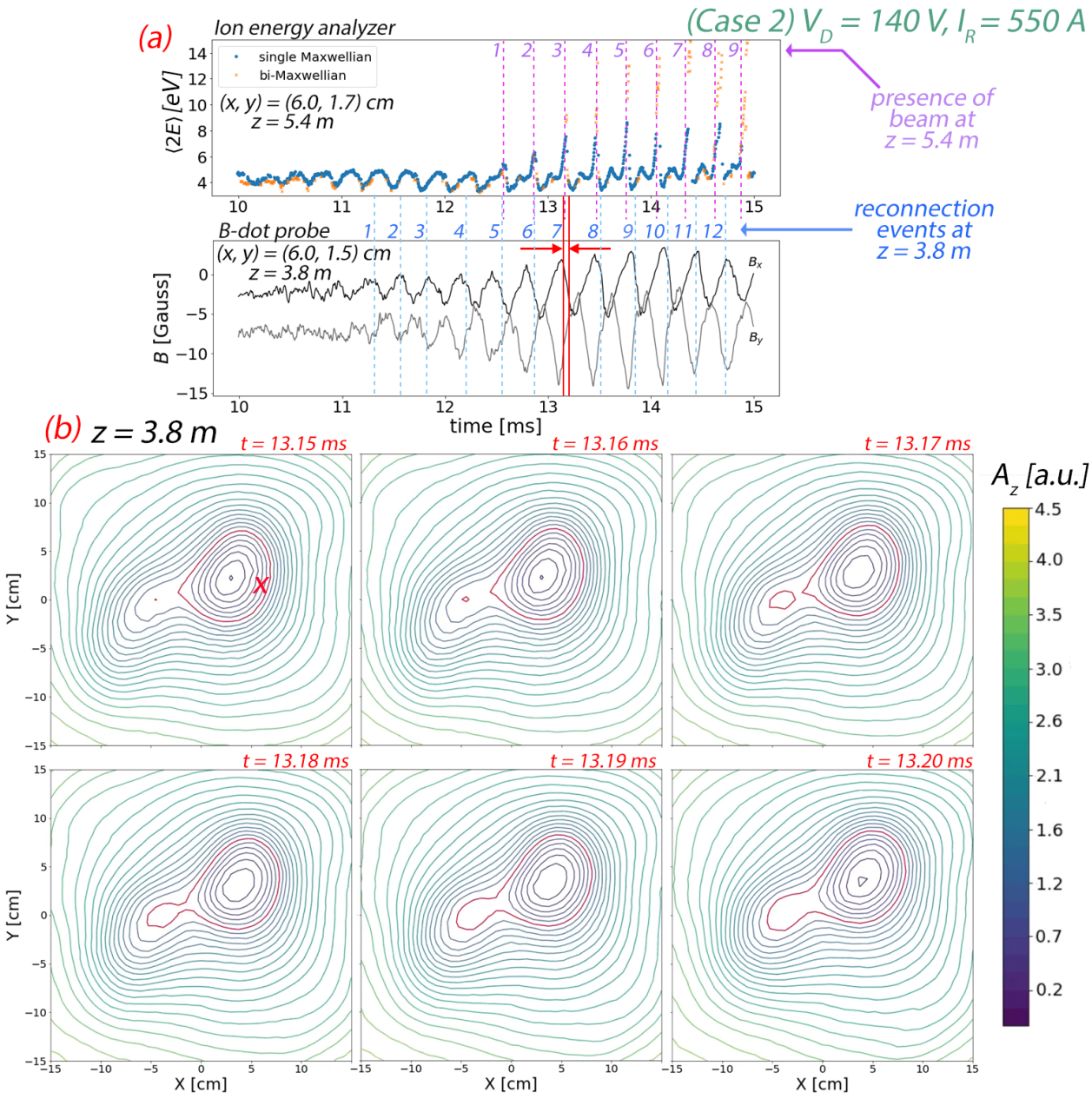

Figure 6.4: (a) Plots of the average energy $\langle 2E \rangle$ and magnetic field components B_x, B_y as a function of time from Fig. 5.11c and Fig. 5.11d are reproduced respectively. The dashed lines in $\langle 2E \rangle$ indicate the times at which a beam is present while the dashed lines in B indicate reconnection events. The times at which the beam is present and when reconnection events appear are numbered by their order of appearance. The time interval of interest ($t = 13.15$–13.20 ms) is indicated by the red parallel lines of the B-dot probe plot. (b) Contour plots of the vector potential A_z. A pair of field lines that appear to reconnect are highlighted in red. The position of the B-dot probe is marked by the cross at $t = 13.15$ ms.

size of the flux rope on the right is larger due to a larger J_z. In addition, a pair of A_z contours colored red is observed to merge, which is evidence to suggest that magnetic reconnection is taking place. In 2D reconnection within the xy-plane, this region would be interpreted as the position of the reconnection site. For reference, the position of the B-dot probe for the B_x and B_y measurements in Fig. 6.4a is marked by the cross at $t = 13.15$ ms.

6.2.2 Observation of Periodic Reconnection Events

The observation of reconnection events similar to Fig. 6.4b also occur at other times indicated by the dashed lines in the B_x, B_y plot of Fig. 6.4b. A total of 12 different reconnection events were observed for the ropes in Case 2. The timing of these events appear to coincide with the oscillations of the ropes.

The timing of the beam, which is indicated by dashed lines in the plot of $\langle 2E \rangle$ in Fig. 6.4a, is also periodic and correlated with the oscillations of the ropes. However, this only implies an indirect correlation between the reconnection events and the beam because of the $\Delta z = 1.6$ m separation between the ion energy analyzer and the B-dot probe. Ions measured by the ion energy analyzer do not necessarily have to originate from the plane of the B-dot probe. In addition, magnetic reconnection is known to occur at multiple locations in three-dimensions (Priest et al. 2003) and have been shown to occur throughout the volume of the flux ropes using topology (Gekelman et al. 2020a). This means that it is very likely for there to be multiple reconnection events that occur at different locations and times within a single flux rope oscillation cycle, giving rise to an observable phase differences between the timing of a reconnection events and the appearance of a beam.

In addition, the peak magnitude of $\langle 2E \rangle$ appears to be correlated with the amplitude of the B_x and B_y oscillations. This is consistent with the hypothesis that the beam is produced by magnetic reconnection as a stronger magnetic field can release more energy to accelerate the ions during magnetic field annihilation.

6.3 Magnetic Reconnection and Ion Heating

6.3.1 Observation of Sub-Alfvénic Ion Flows Along the Magnetic Field

Having established a strong correlation between the presence of the beam and magnetic reconnection, it would then be relevant to consider the physics in which the observed beam is produced. This is likely to be the effect of ion heating and particle acceleration caused by magnetic reconnection when magnetic field energy is rapidly converted into kinetic energy at rates higher than classical dissipation mechanisms (Zweibel and Yamada 2009). If one uses a two-dimensional model of magnetic reconnection, ions jets are expected to leave the reconnection site within the plane of the X-point at the Alfvén speed. This was observed in laboratory reconnection experiments such as the TS-3 spheromak device (Ono et al. 1996) and the Swarthmore Spheromak Experiment (SSX) (Brown 1999).

However, the characteristics of ions in the beam are observed to be different from the Alfvénic ion jets. First, the ions are sub-Alfvénic as their ion thermal velocities ($v = 1.9 \times 10^6$ cm/s) are significantly lesser than the Alfvén speed ($\sim 0.08 v_A$ with $v_A = 2.5 \times 10^7$ cm/s). Although observations of sub-Alfvénic flows are not uncommon in space (Paschmann et al. 1986; Gosling et al. 2007; Liu et al. 2012) and in various reconnection experiments (Gekelman et al. 1982; Hsu et al. 2001; Brown et al. 2006), these flows tend to involve a suppressing mechanism that acts against the flow of ions. For example, the presence of a strong guide field can suppress fast ion outflows by reducing the overall reconnection rate and stabilize the reconnection region by enforcing the frozen-in condition of the field lines (Treumann and Baumjohann 2013). Essentially, the small ion gyroradii which occur as a result of the strong guide field restrict uninhibited ion motion across the magnetic field. In addition, suppressed reconnection outflow velocities were observed in studies where a strong guide field was present (Hsu et al. 2001; Ricci et al. 2004; Pritchett and Coroniti 2004; Huba 2005). Since the background magnetic field of the flux ropes is considered strong ($\beta < 0.01$ for $B_0 = 330$ G), this may be a cause of the sub-Alfvénic flows

observed by the ion energy analyzer.

Next, the drift of the beam is primarily observed along the background magnetic field in the $+z$ direction. This is an unexpected result as ions are frequently observed accelerating across the reconnection layer as opposed to traveling out of the plane. To the author's knowledge, there are only two experiments that measured the flow of ions leaving a two-dimensional plane of reconnection, but neither of those involve ion beams. One of them is from a merging spheromak experiment on the SSX, which had a long tail distribution of super-Alfvénic ions drifting with energies up to 90 eV in a 30 eV (super-thermal) ion background (Brown et al. 2002). These highly energetic ions were predicted by 2D resistive magnetohydrodynamic simulations which showed the ions trapped in "magnetic bubbles" for an Alfvén transit time before they were accelerated by the out-of-plane electric field (Matthaeus et al. 1984). The other experiment is the Magnetic Reconnection Experiment (MRX), where sub-Alfvénic ions (< 1 eV) were observed to leave the plane of two reconnecting flux cores with poloidal magnetic fields (Hsu et al. 2001). The ion energy distribution function was not measured and there was no evidence to suggest that a beam was observed.

As an aside, the plasma parameters of the MRX (helium gas, $n = 5 \times 10^{13}$ cm^{-3}, $T_e = 10$–15 eV, $T_i = 5$–15 eV and $B = 250$ G) are very similar to the LAPD and the plasma sources that trigger magnetic reconnection have similar helicity as the two flux ropes. The MRX used an optical probe to measure the local ion temperature (Fiksel et al. 1998) and showed that the heating and acceleration of ions was weaker for sources that are co-helical as compared to the case of null-helicity which had no guide field (Yamada et al. 1997). The temperature increase for the MRX co-helical case was 3 to 7 eV during reconnection, which is comparable in magnitude to the 6 to 10 eV increase in $\langle 2E \rangle$ from the flux rope ions.

Overall, the conclusion to be drawn from these observations is that the ions of the flux ropes in the beam are likely to be accelerated along the direction of the inductive electric fields ($+z$, which is also the direction of the background magnetic field). The strong guide field is then likely

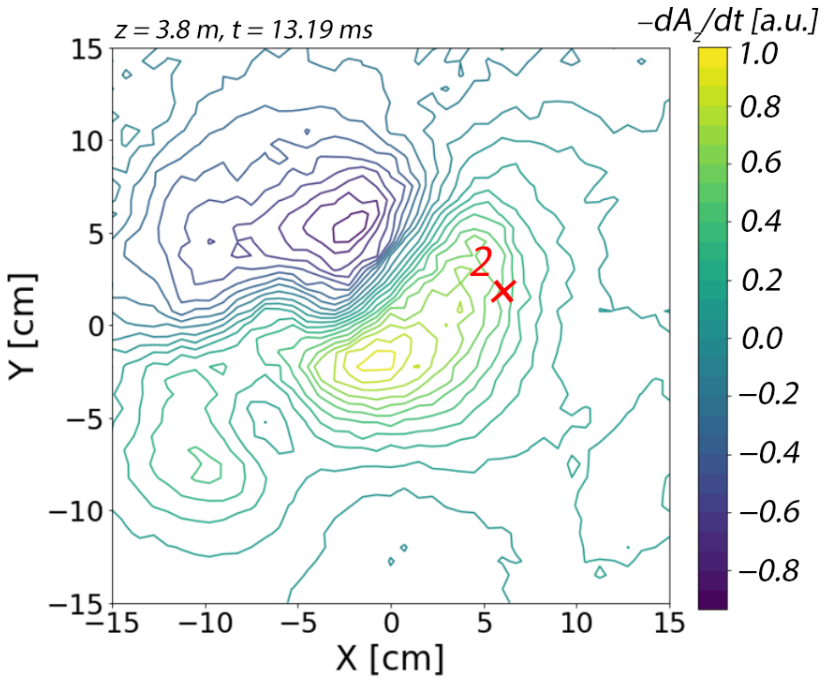

Figure 6.5: A contour plot of $-dA_z/dt$ at $z = 3.8$ m for the ropes in Case 2 ($V_D = 140$ V, $I_R = 550$ A). The position of the ion energy analyzer ($z = 5.4$ m) marked by the cross. The values of $-dA_z/dt$ were normalized such that the minimum and maximum values are from -1 to 1.

to suppress the outflow of ions such that the speeds were sub-Alfvénic.

6.3.2 Inductive Electric Fields and Magnetic Field Annihilation

Inductive electric fields are created when magnetic fields are annihilated during the process of magnetic reconnection. These induced fields drive reverse currents within the plasma that accelerate particles and cause instabilities that heat up the plasma by increasing the reconnection rate (Kulsrud 2001). One example of such an instability is the current-driven ion acoustic instability which propagates longitudinally along the magnetic field (Coroniti and Eviatar 1977). Although it has not been observed in the two flux rope experiment, it was postulated to create large induced electric fields that resulted in anomalously high AC Kubo resistivity (Gekelman et al. 2018a) and large, negative electric potential structures that were present at the edge of the ropes and near the reconnection sites (Gekelman et al. 2018b).

The amount of energy transferred to the ions during reconnection can be estimated by integrating the power density $\boldsymbol{J} \cdot \boldsymbol{E}$ over a unit volume of the reconnection region, i.e.

$$\left(\frac{1}{V}\int \mathrm{d}V\, \boldsymbol{J} \cdot \boldsymbol{E}\right) \cdot \tau_R \tag{6.3.1}$$

where V is the volume of the reconnection region, τ_R is the timescale of a reconnection event and $\boldsymbol{E}$ is the induced electric field $-\frac{\partial \boldsymbol{A}}{\partial t}$. The space charge component of the electric field, $-\nabla\phi$, is ignored as it is not affected by the changing magnetic fields despite having magnitudes that are over 50 times larger than $-\frac{\partial \boldsymbol{A}}{\partial t}$ (Gekelman et al. 2018a). Since the induced electric fields are primarily in the z-direction normal to the plane of reconnection, a contour plot of $-dA_z/dt$ for the ropes in Case 2 is plotted as a reference in Fig. 6.5. The magnitude of the contours cannot be accurately determined and are therefore normalized to a range of -1 and 1. However, the reference dataset estimates the peak magnitude of dA_z/dt to be 0.004 V/cm. The xy-coordinates of the ion energy analyzer is marked by a cross on the figure, showing that $-dA_z/dt$ is in the $+z$ direction at this location.

Given that the local current density of a single flux rope is $J_z = 2.5$ A/cm^2 and estimating a reconnection timescale of $\tau_R = 50$ μs, the total available energy density output of the reconnecting magnetic fields is 0.5 J/m^3. This corresponds to the annihilation of magnetic fields with a magnitude of 0.19 G or 0.06% of $B_0 = 330$ G, which is less than 1% of the total magnetic field annihilated. This is consistent with a previous flux rope study by DeHaas and Gekelman (2017) ($\Delta B = 0.2$ G) and with a series of field line reconnection experiments by Stenzel et al. (1982) where $\Delta B/B_0 \approx 0.3\%$ ($B_0 = 20$ G). However, it is significantly smaller than in solar flares where hundreds of Gauss of magnetic fields are annihilated (Parker 1957), which is estimated to be a third of the total magnetic field (Emslie 1981).

The energy density is then compared to the energy required to heat a unit volume of ions over a defined temperature increase which is given by $n_2 k \Delta T_i$. Here, n_2 is the density of ions

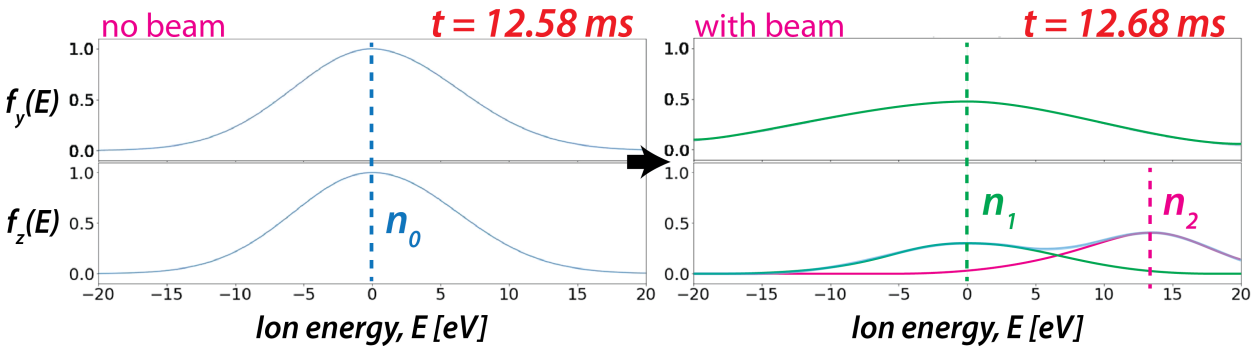

Figure 6.6: An estimation of the ion beam density comparing the distribution function with a beam ($t = 12.68$ ms) to slightly earlier in time when is no beam ($t = 12.58$ ms). The amplitudes are normalized to the distribution function at $t = 12.58$ ms. The initial overall distribution has a density of n_0. When the beam appears, the primary distribution (green) has a density of is n_1 while the beam (pink) has a density of n_2. It is expected that $n_0 = n_1 + n_2$.

that are accelerated by the inductive fields and ΔT_i is the effective temperature increase of the ions. This determines if magnetic reconnection can provide enough energy to energize the ions as observed by the the change in $\langle 2E \rangle$ from the ion energy analyzer.

The value of n_2 is then estimated from the fraction of ions that are present in the beam of the bi-Maxwellian distribution function in proportion to the overall distribution function. For example, consider the beam that was previously shown in Fig. 6.2. The distribution functions before ($t = 12.58$ ms) and during ($t = 12.68$ ms) the appearance of the beam is plotted in Fig. 6.6. The distribution functions are normalized to the peak amplitude of $t = 12.58$ ms. The initial density of the plasma is denoted by n_0 and when the beam appears, the density of the primary distribution is n_1 and the beam is n_2. It is expected that the density does not change within $\Delta t = 0.1$ ms and $n_0 = n_1 + n_2$. However, given that the primary distribution of ions is also spread along other directions (e.g. y) and not only in z as shown in Fig. 6.6, a method of estimating n_2 while accounting for the other directions involve integrating the the distribution function of the beam (pink curve) and comparing it to the integrated overall distribution function in both y and z directions (green and pink curves). A very rough approximation of n_2 is $0.2n_0 = 4 \times 10^{11}$ cm^{-3}. Using a typical increase in $\langle 2E \rangle$ of 6 eV to 10 eV in Case 2 for $k\Delta T_i$, the total energy per unit

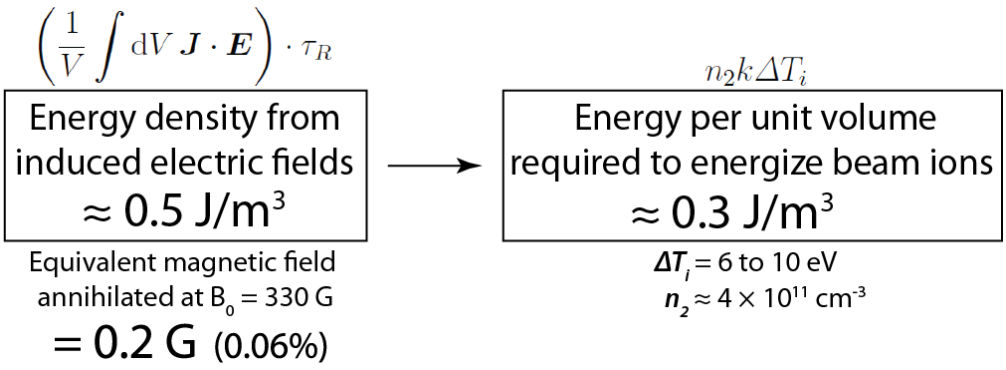

Figure 6.7: A summary of the calculations comparing the energy density produced by the inductive electric fields to the energy per unit volume required to energize the ions by the observed average energy $\langle 2E \rangle$ increase.

volume required to heat ions is calculated to be 0.3 J/m^3.

In general, the dissipated magnetic energy from reconnection is converted into various forms of energy which does not necessarily lead to a direct increase in the kinetic energy of the ions. It is estimated that only 33% of the total magnetic energy reaches the ions from measurements of a laboratory reconnection layer (Yamada et al. 2014), and about 20% for solar flares and coronal mass ejections (Aschwanden et al. 2017). Therefore, it is expected that the beam ions receive only a fraction of the energy produced from the induced electric fields. This appears to be the case for our experiment. The calculations presented in this section are summarized in Fig. 6.7 and is consistent with magnetic reconnection producing an ion beam along the magnetic field that is energized by the inductive electric fields.

6.3.3 Ion Collisions and Energy Losses

The ion-ion collision timescale of the flux ropes is $\tau_{ii} = 33$–94 μs ($T_i = 4$–8 eV), which gives an ion mean free path of 33 to 130 cm. This is shorter than the length of the reconnection region of the ropes which is estimated from a combination of the twist and reconnective activity along with the quasi-sepratrix layer (QSL) to be $\Delta z \approx 2$ m in length (Gekelman et al. 2020a). This means that the ions in the flux ropes are collisional (and by extension the electrons as their mean

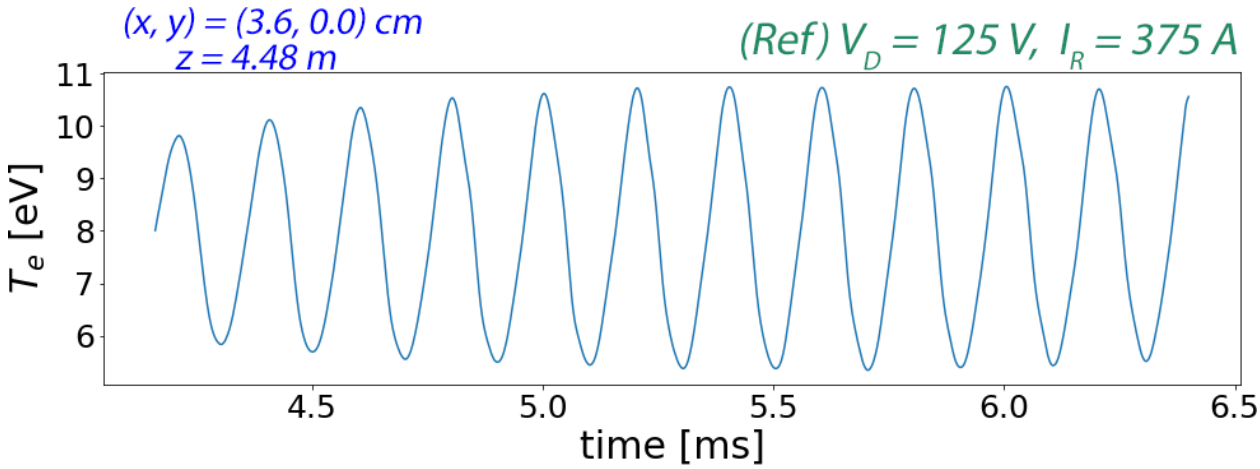

Figure 6.8: A plot of the electron temperature T_e as a function of time in the presence of flux ropes from the reference dataset. The data was measured by an Langmuir probe and is used to estimate the variation of T_e when the flux ropes are present.

free path is smaller) (Gekelman et al. 2018a) and therefore the collision of ions with electrons or neutrals should not be neglected when considering the transfer of energy during reconnection.

The timescale of electron-ion collisions is $\tau_{ei} = 0.16$ μs ($T_e = 7$ eV), which is shorter than the reconnection timescale of 50 μs. However, the energy from electron-ion collisions is insufficient to energize the ions to energies that were observed by the ion energy analyzer. The calculation involves the electron temperature T_e as a function of time measured by an Langmuir probe from the reference dataset as shown in Fig. 6.8. The value of T_e fluctuates between 5.5 and 11 eV which follows the oscillation of the ropes ($f_R = 5$ kHz). By using the largest $T_e = 11$ eV, the smallest $T_i = 4$ eV and a density of 2×10^{12} cm^{-3}, the rate of ion heating by the electrons is calculated by the equation

$$Q_i = \frac{3m_e}{m_i}\frac{nk_B}{\tau_{ee}}(T_e - T_i) \ , \tag{6.3.2}$$

where $\tau_{ee} = 0.63$ μs is the electron collision time and the result is $Q_i = 1.5 \times 10^{-3}$ W/cm^{-3}. Assuming this rate of heating occurs during the reconnection timescale (i.e. $\Delta t = \tau_R = 50$ μs), the energy density works out to be 0.08 J/m^3. This cannot fully account for the observable rise in

$\langle 2E \rangle$ measured by the ion energy analyzer as it is smaller than 30% of the energy that is required to heat the ions (0.3 J/m^3).

On the other hand, collisions can remove energy from the ions after they have been energized by magnetic reconnection. Consider the equipartition time τ_{eq} which is the time taken for two groups of particles mixed with different temperatures to reach a Maxwellian distribution (Spitzer 1967). It is given by the expression

$$\tau_{eq} = 5.87 \frac{m_a m_b}{\sqrt{\mu} n \ln \Lambda} \left(\frac{T_a}{m_a} + \frac{T_b}{m_b} \right)^{3/2} , \qquad \text{(CGS)} \qquad (6.3.3)$$

where the subscripts a and b represent the two species of particles, μ is the atomic mass unit and $\ln \Lambda$ is the Coulomb logarithm. The ion-ion equipartition time for 10 eV helium ions mixed with 4 eV ions of the same species is $\tau_{eq} = 35$ μs, which means that the energetic ions can equilibrate with the background ions within the same time it takes for the ions to be energized. The ions, however, cannot equilibrate with the electrons because ions are more massive than the electrons and $\tau_{eq} = 989$ μs, which is greater than the reconnection timescale.

In addition, ion-neutral collisions through charge exchange (i.e. slow neutrals which transfer electrons to fast ions and as a result produce fast neutrals with slow ions) may also occur. The charge exchange time is given by the expression

$$\tau_c = \frac{1}{n_n \langle \sigma v \rangle} , \qquad (6.3.4)$$

where n_n is the neutral density, σ is the charge exchange cross-section and v is the velocity of the ions. Given $\sigma = 22.8 \times 10^{-16}$ cm^2 for He–He$^+$ charge exchange at 5 eV (Helm 1977), $v = 2 \times 10^6$ cm/s (15 eV) and assuming the largest possible neutral density which is 50% of the plasma density ($n_n = 1 \times 10^{12}$ cm^{-3}), this gives a charge exchange time of 219 μs. In reality, the neutral density is close to 10% in the LAPD and this is increases the charge exchange time. This means that charge exchange can be ignored as it is consistently longer than the reconnection

time.

Finally, it may be noted that the beam ions can drift up to 15 eV or 2×10^6 cm/s along the magnetic field. This means that the ions typically travel a distance of about 100 cm during the reconnection timescale and are therefore very likely to leave the reconnection region after they have been energized. The ions may also lose energy to other mechanisms other than collisiions such as convection and conduction which can account for a significant amount of energy lost be the ions (Hsu et al. 2001). However, a full diagnosis of the relevant transport mechanisms and the resulting energy budget would not be possible here due to the lack of volumetric data of the ion's temperature and energy. This could be the subject of a future study.

6.4 Summary

In this chapter, polar plots were used as visual representations of the two-dimensional distribution function of the ropes in Case 1 ($V_D = 120$ V, $I_D = 610$ A, $f = 3.9$ kHz). The anisotropic distribution functions indicated the directions in which the ions were energized and were used to observe the time evolution of the distribution function for the duration of a spike in the average energy $\langle 2E \rangle$. During this time, the distribution function began as a Maxwellian distribution before a beam appears and was travelling along the magnetic field in the z-direction with sub-Alfvénic drifts of 9 to 15 eV. The beam then disappears and the ion distribution function returns to a Maxwellian. This suggests that the beam is accelerated by $-dA_z/dt$, the out-of-plane induced electric field that is produced by magnetic reconnection.

The correlation between the the spiky structures in $\langle 2E \rangle$ and magnetic reconnection was established using the magnetic field data of the flux ropes in Case 2 ($V_D = 140$ V, $I_D = 550$ A, $f = 3.4$ kHz). The line contours of the magnetic vector potential A_z served as a guide for the position of the reconnection site and reconnecting A_z line contours was used to indicate the time at which magnetic reconnection events occured. The presence of multiple reconnection events

and the correlation between the $\langle 2E \rangle$ spikes and the B_x and B_y amplitudes of the B-dot probe signals indicates that a larger magnetic field can drive a larger increase in the average energy, thereby suggesting that magnetic reconnection may be the cause of the energized ions.

The ions are observed to move in the $+z$ direction normal to the plane of reconnection, which suggests that the acceleration of the ions is caused by the inductive electric fields created by magnetic field annihilation. The ions are sub-Alfvénic which is postulated to be due to the strong guide field in the LAPD ($\beta < 1$) that suppress the reconnection rate. To determine if it is possible for the inductive electric fields to accelerate the ions, the energy density of the inductive electric fields (0.5 J/m^3) was compared to the energy required per unit volume to heat the ions from 6 to 10 eV, the average change in $\langle 2E \rangle$ when the beam appears (0.3 J/m^3). Given that the efficiency of ions receiving energy from the annihilated magnetic fields was less than 50%, the values were found to be comparable and supported the hypothesis that the energy from magnetic field annihilation was enough to drive the acceleration of the ions in the beam.

The impact of collisions on the energy of the ions was also investigated. It was determined that electron-ion collisions were unable to impart enough energy to the ions (0.08 J/m^3) to account for the increase in observable average energy $\langle 2E \rangle$. Yet, the equipartition time of ions (35 μs for 10 eV ions in a 4 eV background) is comparable to the reconnection time ($\tau_R = 50$ μs). Ion-neutral collisions through charge exchange can be ignored as its timescale ($\tau_c = 219$ μs) is longer than the reconnection time.

Overall, magnetic reconnection is very likely to be responsible for releasing energy to accelerate the ions in a beam along the magnetic field. To the author's knowledge, this is the first experimental observation of a field-aligned ion beam generated in a reconnection experiment.

Chapter 7

Conclusion

In this study, the energization of ions in a two flux rope system on the Large Plasma Device (LAPD) was investigated. The two flux ropes were created in a helium plasma and were driven kink-unstable by field-aligned currents that exceeded that Kruskal–Shafranov limit. When these ropes collide, the field lines rearrange themselves and magnetic reconnection occurs. Magnetic field energy is dissipated and the energy can be used to heat or accelerate ions.

A retarding field energy analyzer was constructed to measure the local energy distribution function of ions. The ion energy analyzer was built specifically for deployment on the LAPD and consisted of four transparent grids that were biased to remove primary electrons and selectively screen ions based on their kinetic energies. The current collected by the energy analyzer is then plotted as a function of the discriminator grid bias, which produces an I-V curve that can be differentiated to give the energy distribution function $f(E)$. The ion energy analyzer is directionally biased and can only measure the distribution function in the direction it is facing.

The measured ion distribution functions mostly consisted of a single peak that can be fitted to a Maxwellian distribution. However, some distribution functions were bi-Maxwellian as they consisted of a beam with a primary ion distribution. A time evolution of the distribution function showed that the beam emerges from a single Maxwellian distribution with energies of 10 to 15 eV

and for about 0.1 ms before disappearing. The energies correspond to ion thermal speeds of 1.6–1.9×10^6 cm/s which is considered sub-Alfvénic ($\sim 0.08 v_A$ with $v_A = 2.5 \times 10^7$ m/s).

The average energy $\langle 2E \rangle$, a quantity that is equivalent to the Maxwellian temperature for non-Maxwellian distribution functions, was calculated as a function of time. The distribution function used is a spliced function using the two $f(E)$ curves in opposite directions along the same axis. $\langle 2E \rangle$ was calculated for two different rope conditions: Case 1 with $V_D = 120$ V and $I_R = 610$ A, and Case 2 with $V_D = 140$ V and $I_R = 550$ A. In both cases, the plot of $\langle 2E \rangle$ vs. time consisted of peaks that were strongly correlated with the local magnetic field $\Delta z = 1.6$ m away. The peaks had energies above 8 eV and they were due to the presence of a beam in a bi-Maxwellian distribution function. In addition, the baseline $\langle 2E \rangle$ level was between 4 to 6 eV, which has a range that is similar to the individual peaks' half-width. However, the half-width was not correlated in time. This suggests that the beam ions may only be accelerated and not heated, and that the ion temperature of the flux ropes could be between 4 and 6 eV.

A spectrometer was used to verify the ion temperature of the ropes. This was achieved by measuring the Doppler line broadening of the He II line spectra at 320.3 nm in Case 2 and then fitting it to an artificially-broadened theoretical line spectra. The line-of-sight $\bar{T}_i$ value was found to be 1.59 ± 0.08 eV due to a volume-averaging effect of the spectrometer's field of view. The discrepancy with the ion energy analyzer ($\langle 2E \rangle_z \sim 4-6$ eV) was then reconciled by modeling the spectrometer's field of view to predict the volume-averaged T_i given the ion temperature profile of the flux ropes. The profile was assumed to be identical to J_z and the peak value was set to 6 eV. This produced a T_i value that oscillates between 1.6 and 1.8 eV and is comparable to the measured spectrometer value, thereby supporting the data from the ion energy analyzer.

The ion distribution function in a reconnecting plasma were then further investigated. Using polar plots as a visualization tool, 2D ion distribution functions were constructed, allowing anisotropy in the ion distribution functions to be observed. A beam generally appears as a bubble separate from the primary distribution that is centered on the polar plot and its direction is

indicated by its position on the y or z axes. A time evolution of the $\langle 2E \rangle$ spikes using the polar plots revealed that the beam usually travels in the $+z$ direction along the magnetic field and out of the reconnection plane.

An indirect correlation between the presence of the beam and magnetic reconnection was then established when reconnection events as frequent as the flux rope oscillations were observed. Line contour plots of the magnetic vector potential A_z were used to visualize the location of the reconnection sites and determine the times at which magnetic reconnection occured. The inductive electric field $-dA_z/dt$ was also plotted and was found to be in the $+z$ direction at the location of the ion energy analyzer. As this is the direction in which the beam travels, this suggests that $-dA_z/dt$ is involved in accelerating the ions. A future study could analyze the ion energy analyzer data when $-dA_z/dt$ is negative ($-z$).

Last but not least, magnetic reconnection is very likely to drive the acceleration of the beam ions as the energy density produced by the inductive electric fields (0.5 J/m^3) is comparable to the energy per unit volume required to heat the ions from 6 to 10 eV (0.3 J/m^3). This took into consideration the less than 50% efficiency of energy being transferred to the ions. In contrast, the energy density from electron-ion collisions (0.08 J/m^3) was insufficient to heat the ions by the same amount. More energy transfer mechanisms could be explored and an energy budget for the reconnection process could be drafted. However, this would require volumetric data of the ion temperature and energy at various other positions, which could be the subject of a future study.

Appendix A

Space Charge Limited Current

A.1 Introduction

The Child–Langmuir law for two parallel conductors biased with a potential difference V and separated a distance x is given by (SI units)

$$J_{\text{sc}} = \frac{4\varepsilon_0}{9}\sqrt{\frac{2e}{m}}\frac{V^{3/2}}{x^2} \ , \tag{A.1.1}$$

where J_{sc} is the first order approximation for the space charge limited current. This was originally derived by Child (1911) and Langmuir (1913), who assumed a constant velocity for the emitted charged particles and zero electric field at the surface of the electrode.

In Child and Langmuir's derivation, electrons are the primary charge carriers and are emitted from a hot cathode. A build up of electrons near the surface of the cathode repels other incoming electrons and thus limit the overall current that is emitted from the cathode.

In the ion energy analyzer, however, ions are the primary charge carriers. The collected ion current is thus of interest in the derivation. Similar but opposite to an emitting cathode, ions accumulate near the surface of the collector and repel incoming ions to limit the overall ion

current that is collected. It is then assumed that most electrons have been repelled by earlier grids and the region near the collector would mostly electron-free, even though this may not be the case in reality (Hobbs and Wesson 1967). Nevertheless, the space charge limited current represents the upper limit of the collected current and it is a useful parameter to consider when designing an ion energy analyzer.

The solution to the ion space charge limited current is very similar to that of the electron-emitting cathode as derived by Langmuir and Compton (1931). A more accurate expression is obtained when the velocity distribution of the ions is taken into consideration as these add correction terms to the Child–Langmuir law in (Eq. A.1.1). This will be explored in Appendix A.3.

A.2 Derivation of Child–Langmuir Law

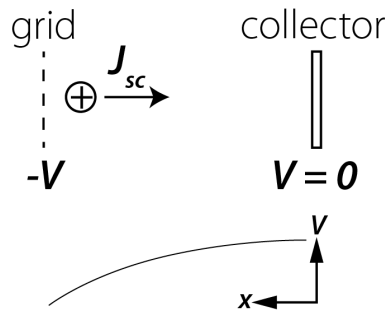

Figure A.1: Coordinate system for a grid-collector system in an ion energy analyzer. $x = 0$ is defined at the collector. The grid allows passage of ions to the collector.

Consider a grid-collector system shown in Fig. A.1 where the grid is biased such that it allows passage of ions to the collector. As more ions enter the system and accumulate near the collector, space charge builds up and creates a potential hill near the collector. The potential hill begins to decelerate more ions and prevent them from reaching the collector.

Then, defining a coordinate system where $x = 0$ is at the collector and is positive from the

collector to the grid, the space charge current density is negative (Umstattd et al. 2005), i.e.

$$J_{sc} = -\rho v \ ,$$

where ρ is the density and v is the velocity of the ion.

Now, the velocity of the ions is ignored and all ions are assumed to reach the collector with zero velocity. The potential of the collector is set to zero (i.e. $V = 0$ at $x = 0$). By the conservation of energy, the energy of an ion located at a point with potential $-V$ is

$$\frac{1}{2}mv^2 = eV \ .$$

Assuming the collector and grid are two infinite parallel planes, the Poisson equation can be reduced to one-dimension (i.e. $\nabla^2 V \rightarrow d^2V/dx^2$) and this gives

$$\frac{d^2V}{dx^2} = \frac{J_{sc}}{\varepsilon_0}\sqrt{\frac{m}{2eV}} \ , \tag{A.2.1}$$

which can be solved in a variety of ways. One solution is to multiply both sides of (Eq. A.2.1) by dV/dx and integrate from x to the collector which has the boundary condition ($V = 0$ at $x = 0$),

$$\left(\left.\frac{dV}{dx}\right|_x\right)^2 - \left(\left.\frac{dV}{dx}\right|_{x=0}\right)^2 = \frac{2J_{sc}}{\varepsilon_0}\sqrt{\frac{2mV}{e}} \ , \tag{A.2.2}$$

which can be re-written as

$$\left(\frac{dV}{dx}\right)^2 = E_0^2 + \frac{2J_{sc}}{\varepsilon_0}\sqrt{\frac{2mV}{e}} \ , \tag{A.2.3}$$

where E_0 is the magnitude of the electric field at the surface of the collector which is dV/dx at

$x = 0$. When the J_{sc} is sufficiently large, it follows that E_0 has to be small or close to zero as it is saturated with the space charge that prevents additional current from flowing to the collector. Therefore, (Eq. A.2.3) can be approximated as

$$\left(\frac{dV}{dx}\right)^2 \approx \frac{2J_{sc}}{\varepsilon_0}\sqrt{\frac{2mV}{e}} \ , \tag{A.2.4}$$

and integrating again with the collector boundary condition ($V = 0$ at $x = 0$) gives

$$J_{sc} = \frac{4\varepsilon_0}{9}\sqrt{\frac{2e}{m}}\frac{V^{3/2}}{x^2} \ , \tag{A.2.5}$$

which is the Child–Langmuir law in (Eq. A.1.1).

A.3 Derivation with Maxwellian Velocity Distribution

In practice, the velocity of the ions that enter the ion energy analyzer may not be zero. When Epstein (1919), Fry (1921), and Langmuir (1923) independently derived the electron space charge limited current, they assumed a Maxwellian velocity distribution for the emitted electrons. Thus, the same consideration will be applied to the ions.

We begin by considering that the number of ions that pass through the grid with velocities between v' and $v' + \mathrm{d}v'$ is

$$\mathrm{d}N \ = N_0\sqrt{\frac{m}{2\pi kT_i}}\exp\left(-\frac{mv'^2}{2kT_i}\right)\mathrm{d}v' \ , \tag{A.3.1}$$

where N_0 is the total number of electrons emitted per unit time per unit area, and v' is the initial emitted velocity of the electrons. As an aside, although (Eq. A.3.1) applies to an emitting solid

of any geometry, it may be noted that in the case of a plane geometry, $\mathrm{d}N$ can be expressed as

$$\mathrm{d}N = \underbrace{N_0 \frac{mv'}{kT_i} \exp\left(-\frac{mv'^2}{2kT_i}\right)}_{n(v')} \mathrm{d}v' \ . \tag{A.3.2}$$

In both equations, the primed velocity v' is used to distinguish the velocity of the ions that enter the area between the grid and collector from the velocity v of the ions at a later point in time and space. The relationship between v and v' can be determined from the conservation of energy when a coordinate system has been established.

This infinitesimal rate of emission $\mathrm{d}N$ makes a contribution to the current density $\mathrm{d}J$ as it moves with a velocity v within the energy analyzer, i.e.

$$e\ \mathrm{d}N = \mathrm{d}J \equiv v\ \mathrm{d}\rho \ ,$$

and therefore the space charge density ρ is given by

$$\rho = e \int \mathrm{d}v' \frac{n(v')}{v} \ , \tag{A.3.3}$$

which is integrated over all permissible *initial* velocities v' for any given position in space.

A.3.1 Coordinate System

The coordinate system is slightly different than in Section A.2 as $x = 0$ is now defined at the mesh grid and x is positive from the grid to the collector. As ions are collected by the energy analyzer, a build-up of positive space charge occurs near the collector as the energy analyzer saturates. This creates a potential hill with potential V_m at position $x = x_m$ as illustrated in Fig. A.2a. The incoming ions have to overcome the potential barrier built up by the space charge and this causes the net current to saturate. This compares with the case of an electron-emitting

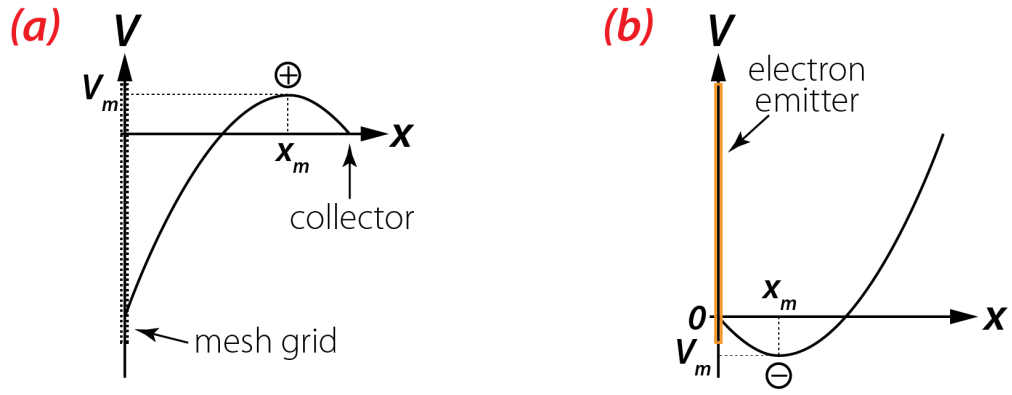

Figure A.2: Potential plots for (a) the grid-collector system in an ion energy analyzer, and (b) a regular electron-emitting cathode.

cathode in Fig. A.2b whose electrons have to overcome the space charge in front of the cathode in order to be emitted.

The space charge potential maximum divides the space between the grid and collector into two different regions, and the overall potential is equivalent to the insertion of a virtual electrode with potential V_m at $x = x_m$ (Langmuir 1923). The continuity of the potential solutions in both regions are then enforced by the boundary condition of the virtual electrode.

Fig. A.3 further defines the coordinate system of the grid-collector system. The grid and collector are assumed to be infinite planes located along one dimension. Let the grid, collector and the space charge potential maximum be defined by positions x_1, x_2 and x_m respectively, with $x_1 < x_m < x_2$. The electric potentials are V_1, V_2 and V_m respectively.

A.3.2 Space Charge Current Densities

The space charge density in both regions have to be determined in order to solve Poisson's equation. Assuming the system is in steady state where $\nabla \cdot \boldsymbol{J} = 0$, let the space charge density for the range $[x_1, x_m]$ be ρ_1 and for $[x_m, x_2]$ be ρ_2.

Calculating the space charge density for the range $[x_m, x_2]$ is straightforward. There is only one current that is present, which is due to the space charge limited current density J_{sc}. These

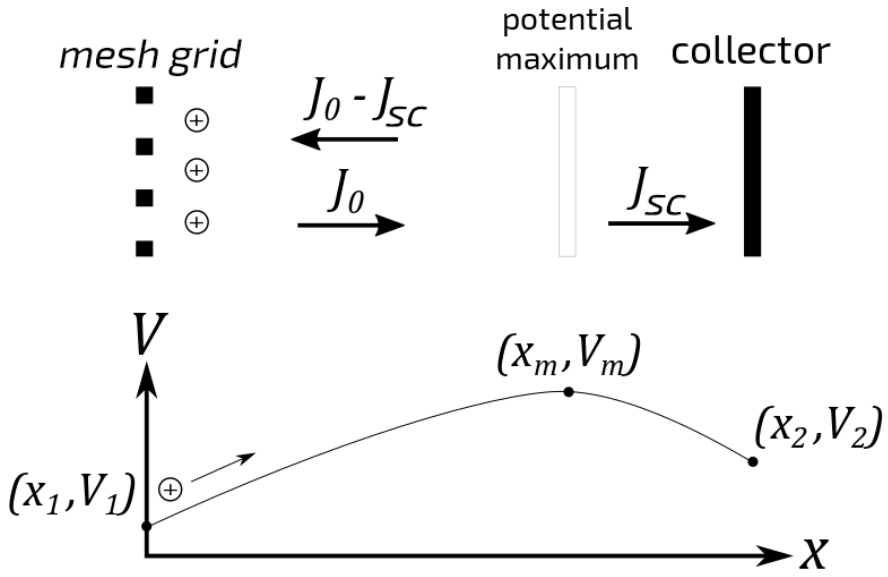

Figure A.3: The initial setup for calculating the space charge limited current in an ion energy analyzer. The potential maximum can be treated as a virtual cathode with potential V_m located at position x_m, and it splits the space charge calculation into two regions. The shape of the potential as a function of position x is plotted but not to scale. The biased grid can be considered to be a source of ions (i.e. a boundary condition).

are from ions that have enough energy to overcome the potential hill created by the space charge.

By the conservation of energy, the criteria for the minimum velocity required of the ions is

$$v = \sqrt{v'^2 - \frac{2e}{m}(V_m - V_1)} > 0$$

or by defining a velocity at the potential hill v_m,

$$v' > \sqrt{\frac{2e}{m}(V_m - V_1)} \equiv v_m \ . \tag{A.3.4}$$

Therefore, the space charge density in this range is

$$\rho_2 = e \int_{v_m}^{\infty} \mathrm{d}v' \, \frac{n(v')}{v} \ . \tag{A.3.5}$$

The space charge density for the range $[x_1, x_m]$ is slightly more complicated. It has contri-

butions from two currents: the first is from all the ions that initially make it past the grid and have a current density J_0, while the second is from ions that do not have enough energy to make it past the potential hill are reflected back into the region. This results in a current density of $J_0 - J_{sc}$ but in the opposite direction. The total space charge density of the region is then the magnitude sum of both space charge current densities, which is $2J_0 - J_{sc}$.

In addition, the ions that are located at x requires an initial minimum velocity that depends on the potential $V(x)$ as these ions need to climb an increasing potential. This minimum velocity condition is given by

$$v(x) = \sqrt{v'^2 - \frac{2e}{m}(V(x) - V_1)} > 0 \ , \tag{A.3.6}$$

which can be rewritten as

$$v' > \sqrt{\frac{2e}{m}(V - V_1)} \ . \tag{A.3.7}$$

Therefore, the total contribution to the overall space charge for this region is

$$\rho_1 = \underbrace{e \int_{\sqrt{\frac{2e}{m}(V-V_1)}}^{\infty} \mathrm{d}v' \, \frac{n(v')}{v}}_{\text{forward}} + \underbrace{e \int_{\sqrt{\frac{2e}{m}(V-V_1)}}^{v_m} \mathrm{d}v' \, \frac{n(v')}{v}}_{\text{reflected}} \ , \tag{A.3.8}$$

or by rearranging the limits to produce a term that is identical to (Eq. A.3.5),

$$\rho_1 = e \left[2 \int_{\sqrt{\frac{2e}{m}(V-V_1)}}^{v_m} + \int_{v_m}^{\infty} \right] \mathrm{d}v' \, \frac{n(v')}{v} \ . \tag{A.3.9}$$

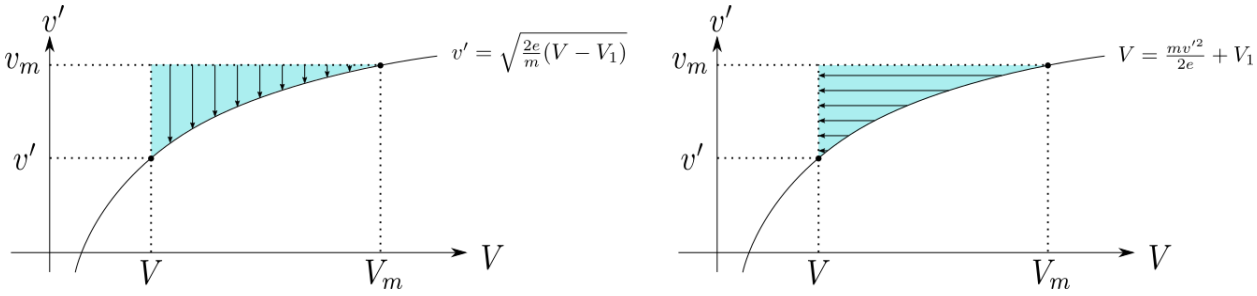

Figure A.4: Changing the order of integration involving the variables V and v'. The blue area is conserved as the integration limits are changed.

A.3.3 Solving Poisson's Equation

Second-order linear partial differential equation To solve for the potential V within the range $[x_1, x_m]$, (Eq. A.3.9) is substituted into Poisson's equation to give

$$\frac{d^2V}{dx^2} = -\frac{e}{\varepsilon_0}\left[2\int_{\sqrt{\frac{2e}{m}(V-V_1)}}^{v_m} + \int_{v_m}^{\infty}\right] \mathrm{d}v' \, \frac{n(v')}{v} \; . \tag{A.3.10}$$

Without loss of generality to the integrand $n(v')/v$, the equation may be integrated between x and x_m by multiplying both sides by $2(dV/dx)$. The boundary condition of the potential hill ($dV/dx = 0$ when $V = V_m$) is also applied. This gives

$$\begin{aligned} 2\int_{x_m}^{x} \mathrm{d}x \left(\frac{d^2V}{dx^2} \cdot \frac{dV}{dx}\right) &= -\frac{2e}{\varepsilon_0}\int_{x_m}^{x} \mathrm{d}x \, \frac{dV}{dx}\left(\left[2\int_{\sqrt{\frac{2e}{m}(V-V_1)}}^{v_m} + \int_{v_m}^{\infty}\right] \mathrm{d}v' \, \frac{n(v')}{v}\right) \\ \left(\frac{dV}{dx}\right)^2 &= -\frac{2e}{\varepsilon_0}\int_{V_m}^{V(x)} \mathrm{d}V \left(\left[2\int_{\sqrt{\frac{2e}{m}(V-V_1)}}^{v_m} + \int_{v_m}^{\infty}\right] \mathrm{d}v' \, \frac{n(v')}{v}\right) \; . \end{aligned} \tag{A.3.11}$$

The first integral on the right of (Eq. A.3.11) can be simplified by changing the order of integration as the limits of the $\mathrm{d}v'$ integral depends on V,

$$\int_{V_m}^{V} \mathrm{d}V \int_{v_m}^{\sqrt{\frac{2e}{m}(V-V_1)}} \mathrm{d}v' \; \rightarrow \int_{v_m}^{\sqrt{\frac{2e}{m}(V-V_1)}} \mathrm{d}v' \int_{\frac{mv'^2}{2e}+V_1}^{V} \mathrm{d}V \; .$$

This is illustrated in Fig. A.4. The blue shaded area is the value of the integral which is conserved when the order of integration and limits are swapped between V and v'. The $\mathrm{d}V$ integral is then evaluated by noting that the denominator depends on V using (Eq. A.3.6) as the substitution,

$$\begin{aligned}\int_{\frac{mv'^2}{2e}+V_1}^{V} \frac{\mathrm{d}V}{\sqrt{v' - \frac{2e}{m}(V - V_1)}} &= \left[-\frac{m}{e}\sqrt{v' - \frac{2e}{m}(V - V_1)}\right]_{\frac{mv'^2}{2e}+V_1}^{V} \\ &= -\frac{mv}{e} \ . \end{aligned} \tag{A.3.12}$$

The same can be done for the other double integral. When all integrals have been evaluated, the result for the range $[x_1, x_m]$ is

$$\left(\frac{dV}{dx}\right)^2 = \frac{2m}{\varepsilon_0}\left(2\int_{\sqrt{\frac{2e}{m}(V-V_1)}}^{v_m} \mathrm{d}v'\, n(v') \cdot v + \int_{v_m}^{\infty} \mathrm{d}v'\, n(v') \cdot (v - v_k)\right) \ , \tag{A.3.13}$$

where $v_k \equiv \sqrt{v'^2 - v_m^2}$, and because the second integral of ρ_1 is ρ_2, the Poisson's equation for the range $[x_m, x_2]$ is

$$\left(\frac{dV}{dx}\right)^2 = \frac{2m}{\varepsilon_0}\int_{v_m}^{\infty} \mathrm{d}v'\, n(v') \cdot (v - v_k) \ . \tag{A.3.14}$$

First-order linear partial differential equation The first-order differential equation (Eq. A.3.13) was derived for any $n(v')$ without loss of generality. However, the distribution of the ion density is now taken into consideration. Assuming an infinite plane geometry, $n(v')$ is given by (Eq. A.3.2),

$$n(v') = N_0 \frac{mv'}{kT_i} \exp\left(-\frac{mv'^2}{2kT_i}\right) \ .$$

It is also convenient to express the integral as a function of v by converting v' to v using (Eq. A.3.6), which is

$$v = \sqrt{v'^2 - \frac{2e}{m}(V - V_1)} \ .$$

Then, the new integration limits become

$$\int_{\sqrt{\frac{2e}{m}(V-V_1)}}^{v_m} \mathrm{d}v' \, v' \to \int_0^{\sqrt{\frac{2e}{m}(V_m-V)}} \mathrm{d}v \, v \ .$$

In (Eq. A.3.13), the first integral is evaluated as

$$\int_{\sqrt{\frac{2e}{m}(V-V_1)}}^{v_m} \mathrm{d}v' \, n(v') \cdot v = \frac{N_0 m}{kT_i} \int_0^{\sqrt{\frac{2e}{m}(V_m-V)}} \mathrm{d}v \, v^2 \exp\left(-\frac{mv^2}{2kT_i} - \frac{e(V-V_1)}{kT_i}\right) \ , \quad \text{(A.3.15)}$$

while the second integral is

$$\int_{v_m}^{\infty} \mathrm{d}v' \, n(v') \cdot (v - v_k) = \frac{N_0 m}{kT_i} \int_{\sqrt{\frac{2e}{m}(V_m-V)}}^{\infty} \mathrm{d}v \, (v^2 - vv_k) \exp\left(-\frac{mv^2}{2kT_i} - \frac{e(V-V_1)}{kT_i}\right) \quad \text{(A.3.16)}$$

$$= \frac{N_0 m}{kT_i} \left[\int_0^{\infty} \mathrm{d}v \, v^2 - \int_0^{\sqrt{\frac{2e}{m}(V_m-V)}} \mathrm{d}v \, v^2 - \int_{\sqrt{\frac{2e}{m}(V_m-V)}}^{\infty} \mathrm{d}v \, vv_k\right] \times \exp\left(-\frac{mv^2}{2kT_i} - \frac{e(V-V_1)}{kT_i}\right) \ . \quad \text{(A.3.17)}$$

As the second integral of (Eq. A.3.17) is exactly the same as (Eq. A.3.15) and the difference between $(dV/dx)^2$ of $[x_1, x_m]$ and $[x_m, x_2]$ is twice the integral in (Eq. A.3.15), $(dV/dx)^2$ can

then be conveniently expressed as

$$\left(\frac{dV}{dx}\right)^2 = \frac{2N_0m^2}{kT_i\varepsilon_0}\exp\left(-\frac{e(V-V_1)}{kT_i}\right) \times \left[\int_0^\infty \mathrm{d}v\, v^2 \pm \int_0^{\sqrt{\frac{2e}{m}(V_m-V)}} \mathrm{d}v\, v^2 - \int_{\sqrt{\frac{2e}{m}(V_m-V)}}^\infty \mathrm{d}v\, vv_k\right]\exp\left(-\frac{mv^2}{2kT_i}\right) \ , \tag{A.3.18}$$

where the plus sign is for the region $[x_1, x_m]$ and the minus sign for $[x_m, x_2]$. The integrals that contain v in (Eq. A.3.18) are then evaluated individually. The first integral contains a Gaussian integral when integrated by parts

$$\int_0^\infty \mathrm{d}v\, v^2 \exp\left(-\frac{mv^2}{2kT_i}\right) = \frac{kT_i}{m}\left(\frac{\sqrt{\pi}}{2}\sqrt{\frac{2kT_i}{m}}\right) \ , \tag{A.3.19}$$

while the second integral uses the error function

$$\begin{aligned}
&\int_0^{\sqrt{\frac{2e}{m}(V_m-V)}} \mathrm{d}v\, v^2 \exp\left(-\frac{mv^2}{2kT_i}\right) \\
&= -\frac{kT_i}{m}\left(\left[v\cdot\exp\left(-\frac{mv^2}{2kT_i}\right)\right]_0^{\sqrt{\frac{2e}{m}(V_m-V)}} - \int_0^{\sqrt{\frac{2e}{m}(V_m-V)}} \mathrm{d}v\, \exp\left(-\frac{mv^2}{2kT_i}\right)\right) \\
&= \frac{kT_i}{m}\sqrt{\frac{2kT_i}{m}}\left[-\sqrt{\frac{e(V_m-V)}{kT_i}}\exp\left(-\frac{e(V_m-V)}{kT_i}\right) + \frac{\sqrt{\pi}}{2}\mathrm{erf}\left(\sqrt{\frac{e(V_m-V)}{kT_i}}\right)\right] \ .
\end{aligned} \tag{A.3.20}$$

The last integral requires the evaluation of v_k in terms of v, i.e.

$$v_k = \sqrt{v^2 - \frac{2e}{m}(V_m - V)} \ ,$$

and this gives

$$\int_{\sqrt{\frac{2e}{m}(V_m-V)}}^{\infty} \mathrm{d}v \left(v \cdot \sqrt{v^2 - \frac{2e}{m}(V_m - V)} \right) \exp\left(-\frac{mv^2}{2kT_i} \right) .$$

Then, using the substitution $u^2 = v^2 - \frac{2e}{m}(V_m - V)$, the integral becomes

$$\int_0^{\infty} \mathrm{d}u \, u^2 \exp\left(-\frac{mu^2}{2kT_i} \right) \exp\left(-\frac{e(V_m - V)}{kT_i} \right) = \frac{kT_i}{m} \sqrt{\frac{2kT_i}{m}} \frac{\sqrt{\pi}}{2} \exp\left(-\frac{e(V_m - V)}{kT_i} \right) .$$

A.3.4 Dimensionless Coordinates

The above integrals can be further simplified with the introduction of two new dimensionless variables. The first is a dimensionless potential η, which contains V

$$\eta = \frac{e(V_m - V)}{kT_i} , \tag{A.3.21}$$

and the second is the dimensionless position coordinate ξ which contains x

$$\xi = \left[\frac{N_0 e^2}{\varepsilon_0} \sqrt{\frac{2\pi m}{(kT_i)^3}} \cdot \exp\left(-\frac{e(V_m - V_1)}{kT_i} \right) \right]^{1/2} (x_m - x) . \tag{A.3.22}$$

These two coordinates reduce $(dV/dx)^2$ (Eq. A.3.18) to a dimensionless equation

$$\left(\frac{d\eta}{d\xi} \right)^2 = e^{\eta} - 1 \pm \left(e^{\eta} \cdot \mathrm{erf}\sqrt{\eta} - \frac{2}{\sqrt{\pi}} \sqrt{\eta} \right) , \tag{A.3.23}$$

where the plus sign is for the region $[x_1, x_m]$ and the minus sign for $[x_m, x_2]$. The solution is then

$$\xi_{\pm}(\eta') = \int_0^{\eta'} \frac{\mathrm{d}\eta}{\sqrt{e^{\eta} - 1 \pm \left(e^{\eta} \cdot \mathrm{erf}\sqrt{\eta} - \frac{2}{\sqrt{\pi}} \sqrt{\eta} \right)}} . \tag{A.3.24}$$

This equation is identical to the characteristic dimensionless equation presented by Epstein (1919), Fry (1921), and Langmuir (1923) for an electron-emitting cathode. However, the difference here is the sign of $(V_m - V)$ and $(x_m - x)$ contained in η and ξ respectively due to the setup of the grid-collector system. Nevertheless, by solving (Eq. A.3.24) to obtain an appropriate η, the space charge current density for ions J_{sc} can be obtained.

Recalling from (Eq. A.3.1) that N_0 is a rate of emission, the space charge current density J_{sc} can also be defined as

$$J_{sc} = N_0 e \cdot \exp\left(-\frac{e(V_m - V_1)}{kT_i}\right) \ , \tag{A.3.25}$$

which is the fraction of incoming particles that have enough energy to overcome the potential hill. This then simplifies ξ so that it may be written as

$$\xi = 2L(x_m - x) \qquad \text{with} \qquad L = \left[\frac{J_{sc}e}{\varepsilon_0}\sqrt{\frac{2\pi m}{(kT_i)^3}}\right]^{1/2} \ . \tag{A.3.26}$$

A.3.5 Numerical Approximation

The integral in $\xi(\eta)$ does not have an analytic form and must be solved numerically. The typical approximation considers a large η (i.e. $\eta > 3$), which is achieved when T_i is small or when there is a large potential difference between the grid and the collector. First, consider the approximation for large x in the error function,

$$\lim_{x\to\infty} \operatorname{erf}(x) = e^{-x^2}\left(-\frac{1}{\sqrt{\pi}x} + \frac{1}{2\sqrt{\pi}x^3} - \frac{3}{4\sqrt{\pi}x^5} + O(x^{-7})\right) + 1 \ ,$$

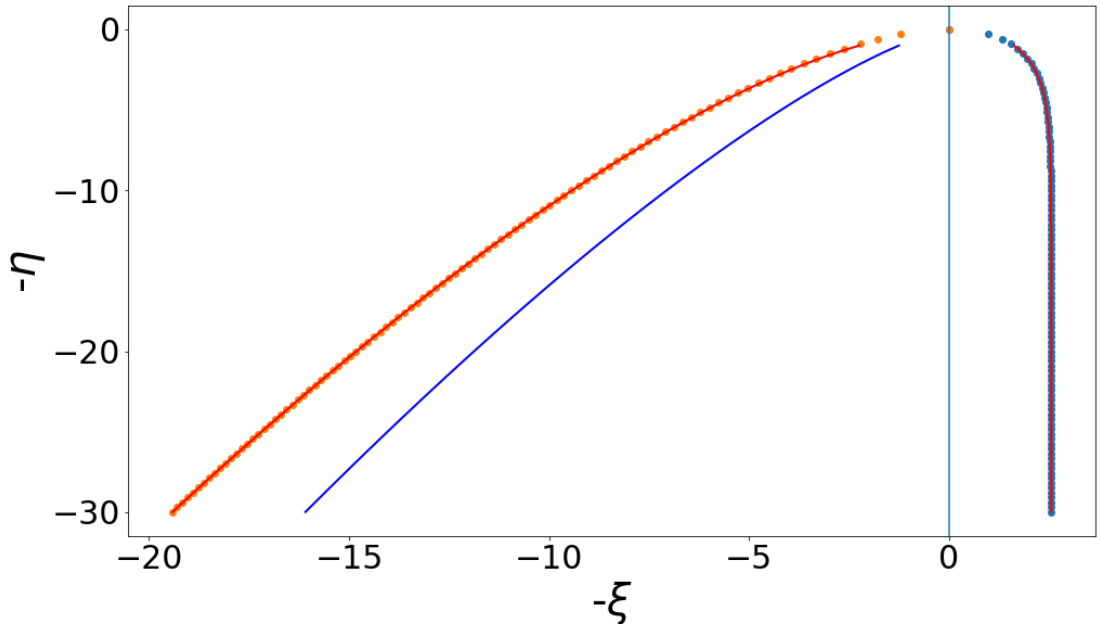

Figure A.5: The relationship between η and ξ is numerically solved and then plotted in a graph of $-\eta$ vs. $-\xi$. This is equivalent to plotting V vs. x. The red lines are from the approximated analytic expressions of $\xi(\eta)$ for large η (i.e. $\eta > 3$). The blue line is from the Child–Langmuir law.

where $O(x^{-7})$ represents terms of order x^{-7} or greater. Then, when $x = \sqrt{\eta}$ in the range $[x_m, x_2]$, we obtain

$$\xi_- = -2.55389 + \sqrt{2}e^{-\eta/2} - 0.0123e^{-\eta} + \frac{1}{3\sqrt{2}}\left(\sqrt{\frac{\eta}{\pi}} + 1\right)e^{-3\eta/2} + O(e^{-2\eta}) \ . \tag{A.3.27}$$

In this case, ξ_- asymptotically converges to -2.55389 when η is very large. Similarly, ξ_+ for the region $[x_1, x_m]$ (Langmuir 1923) is approximated as

$$\xi_+ = \underbrace{\frac{2\sqrt{2}\pi^{1/4}}{3}}_{1.25520}\eta^{3/4} + \underbrace{\frac{\pi^{3/4}}{\sqrt{2}}}_{=1.66858}\eta^{1/4} - 0.50880 - \underbrace{\frac{\pi^{1/4}(3\pi-8)}{8\sqrt{2}}}_{=0.16766}\eta^{-1/4} + \underbrace{\frac{\pi^{3/4}(5\pi-24)}{96\sqrt{2}}}_{=0.14412}\eta^{-3/4}$$
$$+ O\left(\eta^{-5/4}\right) \ . \tag{A.3.28}$$

Plot solution A plot of $-\eta$ as a function of $-\xi$ is shown in Fig. A.5. This is equivalent to plotting V vs. x as both V and x are inversely proportional to η and ξ. In this coordinate system, the grid is located to the left of the plot and the collector on the right. Two types of data are presented in the figure: points represent η and ξ values directly obtained by solving (Eq. A.3.24) using computational software (Wolfram Mathematica), while lines represent the analytic forms of the numerical approximations. The red lines are from ξ_- (Eq. A.3.27) and ξ_+ (Eq. A.3.28) for $3 \leq \eta \leq 30$. The blue line is from the Child–Langmuir law, which is recovered from the first term of ξ_+

$$J_{sc} \approx \frac{4\varepsilon_0}{9}\sqrt{\frac{2e}{m}}\frac{(V_m - V)^{3/2}}{(x_m - x)^2} \ . \tag{A.3.29}$$

ξ_- is undefined for the Child–Langmuir law. The divergence between the blue and red lines shows the effect of the correction terms from accounting the Maxwellian velocity distribution of the incoming ions.

Leading-order correction Langmuir and Compton (1931) reported the space charge limiting current with the leading-order correction term of up to $\sim O(\eta^{1/4})$ using (Eq. A.3.28). This gives

$$J_{sc} \approx \frac{4\varepsilon_0}{9}\sqrt{\frac{2e}{m}}\frac{(V_m - V)^{3/2}}{(x_m - x)^2}\left(1 + \frac{3\sqrt{\pi}}{2}\sqrt{\frac{kT_i}{e(V_m - V)}}\right) \ . \tag{A.3.30}$$

This equation was later cited by Molvik (1981) and various other publications involving ion retarding field energy analyzers (Pitts et al. 2003; Nedzelskiy et al. 2006; Dreval et al. 2009). However, there appears to be a discrepancy in Molvik's equation as T_i was assumed to be in eV when Langmuir and Compton had in fact numerically substituted coefficient values for T_i in Kelvin. As a result, the values of J_{sc} using Molvik's equation may have been reduced by at least a factor of 2. In any case, the limit of J_{sc} has not been tested in any of the aforementioned ion

energy analyzers as the collected currents were less than the order of the calculated space charge limited current.

A.3.6 Alternative Formulation of J_{sc}

The use of (Eq. A.3.30) to find J_{sc} requires knowing the values of V_m and x_m, which are difficult to estimate in practice. However, it is possible to reduce the guesswork by directly solving (Eq. A.3.24) and eliminating one of these variables (x_m).

Consider the grid (x_1, V_1) and the collector (x_2, V_2) which have η values of

$$\eta_1 = \frac{e(V_m - V_1)}{kT_i} \qquad \text{and} \qquad \eta_2 = \frac{e(V_m - V_2)}{kT_i} \ .$$

Their corresponding values of ξ are then given by substitution into (Eq. A.3.24), which are $\xi_+(\eta_1)$ and $\xi_-(\eta_2)$. Then, using (Eq. A.3.26) and taking the difference to eliminate x_m,

$$\xi_+(\eta_1) - \xi_-(\eta_2) = 2L(x_2 - x_1) \ ,$$

an expression with the separation between the biased grid and the collector $(x_2 - x_1)$ is obtained. Since J_{sc} is embedded within L, rearranging the equation gives

$$\boxed{J_{sc} = \left(\frac{\xi_+(\eta_1) - \xi_-(\eta_2)}{2(x_2 - x_1)} \right)^2 \frac{\varepsilon_0}{e} \sqrt{\frac{(kT_i)^3}{2\pi m}}} \ . \tag{A.3.31}$$

Thus, this expression of J_{sc} only has V_m which cannot be directly measured from experiment. This equation appears in (Eq. 4.4.5). Like the Child-Langmuir law, (Eq. A.3.31) is inversely proportional to the square of the distance between the two electrodes. The dependence on the voltage to three-halves power is embedded within ξ.

Bibliography

Aschwanden, M. J., Caspi, A., Cohen, C. M. S., Holman, G., Jing, J., Kretzschmar, M., Kontar, E. P., McTiernan, J. M., Mewaldt, R. A., O'Flannagain, A., et al. (2017). "Global energetics of solar flares. V. Energy closure in flares and coronal mass ejections". In: *Astrophys. J.* **836** (1), p. 17. DOI: 10.3847/1538-4357/836/1/17.

Babcock, H. W. (1961). "The Topology of the Sun's Magnetic Field and the 22-YEAR Cycle". In: *Astrophys. J.* **133**, p. 572. DOI: 10.1086/147060.

Behboodian, J. (1970). "On the modes of a mixture of two normal distributions". In: *Technometrics* **12** (1), pp. 131–139. DOI: 10.1080/00401706.1970.10488640.

Bellan, P. M. (2020). "Caltech lab experiments and the insights they provide into solar corona phenomena". In: *J. Geophys. Res. Space Phys.* **125** (8), e2020JA028139. DOI: 10.1029/2020ja028139.

Bellan, P. M. and Hansen, J. F. (1998). "Laboratory simulations of solar prominence eruptions". In: *Phys. Plasmas* **5** (5), pp. 1991–2000. DOI: 10.1063/1.872870.

Biskamp, D. (1986). "Magnetic reconnection via current sheets". In: *Phys. Fluids* **29** (5), pp. 1520–1531. DOI: 10.1063/1.865670.

Böhm, C. and Perrin, J. (1993). "Retarding-field analyzer for measurements of ion energy distributions and secondary electron emission coefficients in low-pressure radio frequency discharges". In: *Rev. Sci. Instrum.* **64** (1), pp. 31–44. DOI: 10.1063/1.1144398.

Borg, A. L., Taylor, M. G. G. T., and Eastwood, J. P. (2012). "Observations of magnetic flux ropes during magnetic reconnection in the Earth's magnetotail". In: *Annales Geophysicae*. Vol. 30. 5. Copernicus GmbH, pp. 761–773. DOI: 10.5194/angeo-30-761-2012.

Bostick, W. H. (1956). "Simulation of solar prominence in the laboratory". In: *Phys. Rev.* **104** (4), p. 1191. DOI: 10.1103/physrev.104.1191.2.

Brown, M. R. (1999). "Experimental studies of magnetic reconnection". In: *Phys. Plasmas* **6** (5), pp. 1717–1724. DOI: 10.1063/1.873430.

Brown, M. R., Cothran, C. D., and Fung, J. (2006). "Two fluid effects on three-dimensional reconnection in the Swarthmore Spheromak Experiment with comparisons to space data". In: *Phys. Plasmas* **13** (5), p. 056503. DOI: 10.1063/1.2180729.

Brown, M. R., Cothran, C. D., Landreman, M., Schlossberg, D., Matthaeus, W. H., Qin, G., Lukin, V. S., and Gray, T. (2002). "Energetic particles from three-dimensional magnetic reconnection events in the Swarthmore Spheromak Experiment". In: *Phys. Plasmas* **9** (5), pp. 2077–2084. DOI: 10.1063/1.1458589.

Brunner, D., LaBombard, B., Ochoukov, R., Sullivan, R., and Whyte, D. (2013a). "Space-charge limits of ion sensitive probes". In: *Plasma Phys. Control. Fusion* **55** (12), p. 125004. DOI: 10.1088/0741-3335/55/12/125004.

Brunner, D., LaBombard, B., Ochoukov, R., and Whyte, D. (2013b). "Scanning retarding field analyzer for plasma profile measurements in the boundary of the Alcator C-Mod tokamak". In: *Rev. Sci. Instrum.* **84** (3), p. 033502. DOI: 10.1063/1.4793785.

Buneman, O. (1959). "Dissipation of Currents in Ionized Media". In: *Phys. Rev.* **115** (3), pp. 503–517. DOI: 10.1103/PhysRev.115.503.

Burke, G. L. (1940). "The corrosion of metals in tissues; and an introduction to tantalum". In: *Can. Med. Assoc. J.* **43** (2), p. 125.

Cartwright, M. L. and Moldwin, M. B. (2010). "Heliospheric evolution of solar wind small-scale magnetic flux ropes". In: *J. Geophys. Res. Space Phys.* **115** (A8). DOI: 10.1029/2009ja014271.

Chen, F. F. (2001). "Langmuir probe analysis for high density plasmas". In: *Phys. Plasmas* **8** (6), pp. 3029–3041. DOI: 10.1063/1.1368874.

Chen, F. F. et al. (1984). *Introduction to Plasma Physics and Controlled Fusion*. Vol. 1. Springer. DOI: 10.1007/978-1-4757-5595-4.

Child, C. D. (1911). "Discharge from hot CaO". In: *Phys. Rev. (Series I)* **32** (5), p. 492. DOI: 10.1103/physrevseriesi.32.492.

Chung, K.-S., Hutchinson, I. H., LaBombard, B., and Conn, R. W. (1989). "Plasma flow measurements along the presheath of a magnetized plasma". In: *Phys. Fluids B* **1** (11), pp. 2229–2238. DOI: 10.1063/1.859039.

Chung, K.-S. (2006). "Why is the Mach probe formula expressed as $R = J_{up}/J_{dn} = \exp[KM_\infty]$?" In: *Jpn. J. Appl. Phys.* **45** (10R), p. 7914. DOI: 10.1143/jjap.45.7914.

Cloutier, P. A., Law, C. C., Crider, D. H., Walker, P. W., Chen, Y., Acuna, M. H., Connerney, J. E. P., Lin, R. P., Anderson, K. A., Mitchell, D. L., et al. (1999). "Venus-like interaction of the solar wind with Mars". In: *Geophys. Res. Lett.* **26** (17), pp. 2685–2688. DOI: 10.1029/1999gl900591.

Cooper, C. M., Gekelman, W., Pribyl, P., and Lucky, Z. (2010). "A new large area lanthanum hexaboride plasma source". In: *Rev. Sci. Instrum.* **81** (8), p. 083503. DOI: 10.1063/1.3471917.

Coroniti, F. V. and Eviatar, A. (1977). "Magnetic field reconnection in a collisionless plasma". In: *Astrophys. J. Suppl. Ser.* **33**, pp. 189–210. DOI: 10.1086/190423.

Daughton, W. (1999). "The unstable eigenmodes of a neutral sheet". In: *Phys. Plasmas* **6** (4), pp. 1329–1343. DOI: 10.1063/1.873374.

DeHaas, T. and Gekelman, W. (2017). "Helicity transformation under the collision and merging of two magnetic flux ropes". In: *Phys. Plasmas* **24** (7), p. 072108. DOI: 10.1063/1.4991413.

DeHaas, T., Gekelman, W., and Van Compernolle, B. (2015). "Experimental study of a linear/nonlinear flux rope". In: *Phys. Plasmas* **22** (8), p. 082118. DOI: 10.1063/1.4928888.

Drake, J. F., Shay, M. A., and Swisdak, M. (2008). "The Hall fields and fast magnetic reconnection". In: *Phys. Plasmas* **15** (4), p. 042306. DOI: 10.1063/1.2901194.

Drake, J. F., Swisdak, M., Cattell, C., Shay, M. A., Rogers, B. N., and Zeiler, A. (2003). "Formation of electron holes and particle energization during magnetic reconnection". In: *Science* **299** (5608), pp. 873–877. DOI: 10.1126/science.1080333.

Dreval, M., Rohraff, D., Xiao, C., and Hirose, A. (2009). "Retarding field energy analyzer for the Saskatchewan Torus–Modified plasma boundary". In: *Rev. Sci. Instrum.* **80** (10), p. 103505. DOI: 10.1063/1.3247902.

Elphic, R. C., Cattell, C. A., Takahashi, K., Bame, S. J., and Russell, C. T. (1986). "ISEE-1 and 2 observations of magnetic flux ropes in the magnetotail: FTE's in the plasma sheet?" In: *Geophys. Res. Lett.* **13** (7), pp. 648–651. DOI: 10.1029/gl013i007p00648.

Emslie, A. G. (1981). "An Interacting Loop Model of Solar Flare Bursts". In: *Astrophys. Lett.* **22** (2), pp. 171–177. ISSN: 0004-6388.

Epstein (1919). In: *Ber. d. Deut. phys. Ges.* **21**, p. 85.

Everson, E. T., Pribyl, P., Constantin, C. G., Zylstra, A., Schaeffer, D., Kugland, N. L., and Niemann, C. (2009). "Design, construction, and calibration of a three-axis, high-frequency magnetic probe (B-dot probe) as a diagnostic for exploding plasmas". In: *Rev. Sci. Instrum.* **80** (11), p. 113505. DOI: 10.1063/1.3246785.

Fiksel, G., Almagri, A. F., Chapman, B. E., Mirnov, V. V., Ren, Y., Sarff, J. S., and Terry, P. W. (2009). "Mass-dependent ion heating during magnetic reconnection in a laboratory plasma". In: *Phys. Rev. Lett.* **103** (14), p. 145002. DOI: 10.1103/physrevlett.103.145002.

Fiksel, G., Den Hartog, D. J., and Fontana, P. W. (1998). "An optical probe for local measurements of fast plasma ion dynamics". In: *Rev. Sci. Instrum.* **69** (5), pp. 2024–2026. DOI: 10.1063/1.1148892.

Fiske, M. D. (1942). "The temperature scale, thermionics, and thermatomics of Tantalum". In: *Phys. Rev.* **61** (7-8), p. 513. DOI: 10.1103/physrev.61.513.

Fitzpatrick, R. (2014). *Plasma Physics: An Introduction*. CRC Press. ISBN: 9780429169069. DOI: 10.1201/b17263.

Fry, T. C. (1921). "The Thermionic Current between Parallel Plane Electrodes; Velocities of Emission Distributed According to Maxwell's Law". In: *Phys. Rev.* **17** (4), pp. 441–452. DOI: 10.1103/PhysRev.17.441.

Furno, I., Intrator, T., Torbert, E., Carey, C., Cash, M. D., Campbell, J. K., Fienup, W. J., Werley, C. A., Wurden, G. A., and Fiksel, G. (2003). "Reconnection scaling experiment: A new device for three-dimensional magnetic reconnection studies". In: *Rev. Sci. Instrum.* **74** (4), pp. 2324–2331. DOI: 10.1063/1.1544051.

Gekelman, W., De Haas, T., Daughton, W., Van Compernolle, B., Intrator, T., and Vincena, S. (2016a). "Pulsating magnetic reconnection driven by three-dimensional flux-rope interactions". In: *Phys. Rev. Lett.* **116** (23), p. 235101. DOI: 10.1103/physrevlett.116.235101.

Gekelman, W., DeHaas, T., Pribyl, P., Vincena, S., Van Compernolle, B., Sydora, R., and Tripathi, S. K. P. (2018a). "Nonlocal Ohms Law, Plasma Resistivity, and Reconnection During Collisions of Magnetic Flux Ropes". In: *Astrophys. J.* **853** (1), p. 33. DOI: 10.3847/1538-4357/aa9fec.

Gekelman, W., Lawrence, E., Collette, A., Vincena, S., Van Compernolle, B., Pribyl, P., Berger, M., and Campbell, J. (2010). "Magnetic field line reconnection in the current systems of flux ropes and Alfvén waves". In: *Phys. Scr.* **2010** (T142), p. 014032. DOI: 10.1088/0031-8949/2010/t142/014032.

Gekelman, W., Lawrence, E., and Van Compernolle, B. (2012). "Three-dimensional reconnection involving magnetic flux ropes". In: *Astrophys. J.* **753** (2), p. 131. DOI: 10.1088/0004-637x/753/2/131.

Gekelman, W., Pfister, H., Lucky, Z., Bamber, J., Leneman, D., and Maggs, J. (1991). "Design, construction, and properties of the large plasma research device – The LAPD at UCLA". In: *Rev. Sci. Instrum.* **62** (12), pp. 2875–2883. DOI: 10.1063/1.1142175.

Gekelman, W., Pribyl, P., Lucky, Z., Drandell, M., Leneman, D., Maggs, J., Vincena, S., Van Compernolle, B., Tripathi, S. K. P., Morales, G., et al. (2016b). "The upgraded Large Plasma Device, a machine for studying frontier basic plasma physics". In: *Rev. Sci. Instrum.* **87** (2), p. 025105. DOI: 10.1063/1.4941079.

Gekelman, W., Stenzel, R. L., and Wild, N. (1982). "Magnetic field line reconnection experiments, 3. Ion acceleration, flows, and anomalous scattering". In: *J. Geophys. Res. Space Phys.* **87** (A1), pp. 101–110. DOI: 10.1029/ja087ia01p00101.

Gekelman, W., DeHaas, T., Prior, C., and Yeates, A. (2020a). "Using topology to locate the position where fully three-dimensional reconnection occurs". In: *SN Applied Sciences* **2** (12), pp. 1–15. DOI: 10.1007/s42452-020-03896-4.

Gekelman, W., Maggs, J. E., and Pfister, H. (1992). "Experiments on the interaction of current channels in a laboratory plasma: Relaxation to the force-free state". In**: 20** (6), pp. 614–621. DOI: 10.1109/27.199501.

Gekelman, W., Van Compernolle, B., DeHaas, T., and Vincena, S. (2014). "Chaos in magnetic flux ropes". In: *Plasma Phys. Control. Fusion* **56** (6), p. 064002. DOI: 10.1088/0741-3335/56/6/064002.

Gosling, J. T., Eriksson, S., Phan, T. D., Larson, D. E., Skoug, R. M., and McComas, D. J. (2007). "Direct evidence for prolonged magnetic reconnection at a continuous x-line within the heliospheric current sheet". In: *Geophys. Res. Lett.* **34** (6). DOI: 10.1029/2006gl029033.

Greiner, F., Block, D., and Piel, A. (2004). "Observation of Mode like Coherent Structures in Curved Magnetic Fields of a Simple Magnetized Torus". In: *Contrib. Plasm. Phys.* **44** (4), pp. 335–346. DOI: 10.1002/ctpp.200410050.

Griem, H. R. (1997). "Principles of Plasma Spectroscopy". In: ed. by M. G. Haines, K. I. Hopcraft, I. H. Hutchinson, C. M. Surko, and K. Schindler. Cambridge England New York: Cambridge University Press. Chap. 4. Spectral line broadening, pp. 54–131. ISBN: 0521455049. DOI: 10.1017/cbo9780511524578.

Helm, H. (1977). "The cross section for symmetric charge exchange of He^+ in He at energies between 0.3 and 8 eV". In: *J. Phys. B: At. Mol. Phys.* **10** (18), p. 3683. DOI: 10.1088/0022-3700/10/18/025.

Hershkowitz, N. (1989). "How Langmuir Probes Work". In: ed. by O. Auciello and D. L. Flamm. Vol. 1. Academic Press. Chap. 3, pp. 113–183. DOI: 10.1016/b978-0-12-067635-4.50008-9.

Hobbs, G. D. and Wesson, J. A. (1967). "Heat flow through a Langmuir sheath in the presence of electron emission". In: *Plasma Phys.* **9** (1), p. 85. DOI: 10.1088/0032-1028/9/1/410.

Hoshino, M., Mukai, T., Yamamoto, T., and Kokubun, S. (1998). "Ion dynamics in magnetic reconnection: Comparison between numerical simulation and Geotail observations". In: *J. Geophys. Res. Space Phys.* **103** (A3), pp. 4509–4530. DOI: 10.1029/97ja01785.

Hsu, S. C., Carter, T. A., Fiksel, G., Ji, H., Kulsrud, R. M., and Yamada, M. (2001). "Experimental study of ion heating and acceleration during magnetic reconnection". In: *Phys. Plasmas* **8** (5), pp. 1916–1928. DOI: 10.1063/1.1356737.

Huba, J. D. (2005). "Hall magnetic reconnection: Guide field dependence". In: *Phys. Plasmas* **12** (1), p. 012322. DOI: 10.1063/1.1834592.

Hudis, M. and Lidsky, L. M. (1970). "Directional Langmuir Probe". In: *J. Appl. Phys.* **41** (12), pp. 5011–5017. DOI: 10.1063/1.1658578.

Hutchinson, I. H. (2002). "The invalidity of a Mach probe model". In: *Phys. Plasmas* **9** (5), pp. 1832–1833. DOI: 10.1063/1.1464886.

— (2008). "Oblique ion collection in the drift approximation: How magnetized Mach probes really work". In: *Phys. Plasmas* **15** (12), p. 123503. DOI: 10.1063/1.3028314.

Ingram, S. G. and Braithwaite, N. S. J. (1988). "Ion and electron energy analysis at a surface in an RF discharge". In: *J. Phys. D: Appl. Phys.* **21** (10), p. 1496. DOI: 10.1088/0022-3727/21/10/005.

Intrator, T. P., Sun, X., Lapenta, G., Dorf, L., and Furno, I. (2009). "Experimental onset threshold and magnetic pressure pile-up for 3D reconnection". In: *Nat. Phys.* **5** (7), pp. 521–526. DOI: 10.1038/nphys1300.

Janvier, M. (2017). "Three-dimensional magnetic reconnection and its application to solar flares". In: *J. Plasma Phys.* **83** (1). DOI: 10.1017/s0022377817000034.

Jasinski, J. M., Slavin, J. A., Arridge, C. S., Poh, G., Jia, X., Sergis, N., Coates, A. J., Jones, G. H., and Waite Jr., J. H. (2016). "Flux transfer event observation at Saturn's dayside magnetopause by the Cassini spacecraft". In: *Geophys. Res. Lett.* **43** (13), pp. 6713–6723. DOI: 10.1002/2016gl069260.

Ji, H., Yamada, M., Hsu, S., and Kulsrud, R. (1998). "Experimental Test of the Sweet-Parker Model of Magnetic Reconnection". In: *Phys. Rev. Lett.* **80** (15), p. 3256. DOI: 10.1103/physrevlett.80.3256.

Kemp, R. F. and Sellen Jr., J. M. (1966). "Plasma Potential Measurements by Electron Emissive Probes". In: *Rev. Sci. Instrum.* **37** (4), pp. 455–461. DOI: 10.1063/1.1720213.

Khabarova, O., Malandraki, O., Malova, H., Kislov, R., Greco, A., Bruno, R., Pezzi, O., Servidio, S., Li, G., Matthaeus, W., et al. (2021). "Current Sheets, Plasmoids and Flux Ropes in the Heliosphere". In: *Space Sci. Rev.* **217** (3), pp. 1–97. DOI: 10.1007/s11214-021-00814-x.

Kivelson, M. G. and Russell, C. T. (1983). "The interaction of flowing plasmas with planetary ionospheres: A Titan-Venus comparison". In: *J. Geophys. Res. Space Phys.* **88** (A1), pp. 49–57. DOI: 10.1029/ja088ia01p00049.

Kramida, A. and Ralchenko, Y. (1999). *NIST Atomic Spectra Database, NIST Standard Reference Database 78*. en. DOI: 10.18434/T4W30F.

Kruskal, M. and Tuck, J. L. (1958). "The instability of a pinched fluid with a longitudinal magnetic field". In: *Proc. R. Soc. Lond. A* **245** (1241), pp. 222–237. DOI: 10.1098/rspa.1958.0079.

Kubo, R. (1966). "The fluctuation-dissipation theorem". In: *Rep. Prog. Phys.* **29** (1), p. 255. DOI: 10.1088/0034-4885/29/1/306.

Kulsrud, R. M. (2001). "Magnetic reconnection: Sweet–Parker versus Petschek". In: *Earth Planets Space* **53** (6), pp. 417–422. DOI: 10.1186/bf03353251.

Kumar, S. T. A., Almagri, A. F., Craig, D., Den Hartog, D. J., Nornberg, M. D., Sarff, J. S., and Terry, P. W. (2013). "Charge-to-mass-ratio-dependent ion heating during magnetic reconnection in the MST RFP". In: *Phys. Plasmas* **20** (5), p. 056501. DOI: 10.1063/1.4804958.

Langmuir, I. (1913). "The Effect of Space Charge and Residual Gases on Thermionic Currents in High Vacuum". In: *Phys. Rev.* **2** (6), pp. 450–486. DOI: 10.1103/PhysRev.2.450.

Langmuir, I. (1923). "The Effect of Space Charge and Initial Velocities on the Potential Distribution and Thermionic Current between Parallel Plane Electrodes". In: *Phys. Rev.* **21** (4), p. 419. DOI: 10.1103/physrev.21.419.

Langmuir, I. and Compton, K. T. (1931). "Electrical Discharges in Gases Part II. Fundamental Phenomena in Electrical Discharges". In: *Rev. Mod. Phys.* **3** (2), pp. 191–257. DOI: 10.1103/RevModPhys.3.191.

Lawrence, E. E. and Gekelman, W. (2009). "Identification of a Quasiseparatrix Layer in a Reconnecting Laboratory Magnetoplasma". In: *Phys. Rev. Lett.* **103** (10), p. 105002. DOI: 10.1103/physrevlett.103.105002.

Leneman, D. and Gekelman, W. (2001). "A novel angular motion vacuum feedthrough". In: *Rev. Sci. Instrum.* **72** (8), pp. 3473–3474. DOI: 10.1063/1.1374588.

Leneman, D., Gekelman, W., and Maggs, J. (2006). "The plasma source of the Large Plasma Device at University of California, Los Angeles". In: *Rev. Sci. Instrum.* **77** (1), p. 015108. DOI: 10.1063/1.2150829.

Lepping, R. P., Fairfield, D. H., Jones, J., Frank, L. A., Paterson, W. R., Kokubun, S., and Yamamoto, T. (1995). "Cross-tail magnetic flux ropes as observed by the GEOTAIL spacecraft". In: *Geophys. Res. Lett.* **22** (10), pp. 1193–1196. DOI: 10.1029/94gl01114.

Li, T., Priest, E., and Guo, R. (2021). "Three-dimensional magnetic reconnection in astrophysical plasmas". In: *Proc. R. Soc. A* **477** (2249), p. 20200949. DOI: 10.1098/rspa.2020.0949.

Lide, D. R. (1993). *CRC Handbook of Chemistry and Physics: A Ready-reference Book of Chemical and Physical Data*. Boca Raton, Fla. London: CRC Press. ISBN: 9780849305955.

Liu, Y.-H., Drake, J. F., and Swisdak, M. (2012). "The structure of the magnetic reconnection exhaust boundary". In: *Phys. Plasmas* **19** (2), p. 022110. DOI: 10.1063/1.3685755.

Lovberg, R. H. (1965). "Plasma Diagnostic Techniques". In: ed. by R. H. Huddlestone and S. L. Leonard. 65. Academic Press Inc. Chap. 3. Magnetic Probes.

Maggs, J. E. and Morales, G. J. (2011). "Generality of Deterministic Chaos, Exponential Spectra, and Lorentzian Pulses in Magnetically Confined Plasmas". In: *Phys. Rev. Lett.* **107** (18), p. 185003. DOI: 10.1103/physrevlett.107.185003.

Magnus, F. and Gudmundsson, J. T. (2008). "Digital smoothing of the Langmuir probe I-V characteristic". In: *Rev. Sci. Instrum.* **79** (7), p. 073503. DOI: 10.1063/1.2956970.

Mandrini, C. H., Pohjolainen, S., Dasso, S., Green, L. M., Démoulin, P., Driel-Gesztelyi, L. van, Copperwheat, C., and Foley, C. (2005). "Interplanetary flux rope ejected from an X-ray bright point: The smallest magnetic cloud source-region ever observed". In: *Astron. Astrophys.* **434** (2), pp. 725–740. DOI: 10.1051/0004-6361:20041079.

Marubashi, K., Akiyama, S., Yashiro, S., Gopalswamy, N., Cho, K.-S., and Park, Y.-D. (2015). "Geometrical Relationship Between Interplanetary Flux Ropes and Their Solar Sources". In: *Sol. Phys.* **290** (5), pp. 1371–1397. DOI: 10.1007/s11207-015-0681-4.

Matthaeus, W. H., Ambrosiano, J. J., and Goldstein, M. L. (1984). "Particle Acceleration by Turbulent Magnetohydrodynamic Reconnection". In: *Phys. Rev. Lett.* **53** (15), p. 1449. DOI: 10.1103/physrevlett.53.1449.

Meija, J., Coplen, T. B., Berglund, M., Brand, W. A., De Bièvre, P., Gröning, M., Holden, N. E., Irrgeher, J., Loss, R. D., Walczyk, T., et al. (2016). "Atomic weights of the elements 2013 (IUPAC Technical Report)". In: *Pure Appl. Chem.* **88** (3), pp. 265–291. DOI: 10.1515/pac-2015-0305.

Merlino, R. L. (2007). "Understanding Langmuir probe current-voltage characteristics". In: *Am. J. Phys* **75** (12), pp. 1078–1085. DOI: 10.1119/1.2772282.

Moldwin, M. B., Phillips, J. L., Gosling, J. T., Scime, E. E., McComas, D. J., Bame, S. J., Balogh, A., and Forsyth, R. J. (1995). "Ulysses observation of a noncoronal mass ejection flux rope: Evidence of interplanetary magnetic reconnection". In: *J. Geophys. Res. Space Phys.* **100** (A10), pp. 19903–19910. DOI: 10.1029/95ja01123.

Molvik, A. W. (1981). "Large acceptance angle retarding-potential analyzers". In: *Rev. Sci. Instrum.* **52** (5), pp. 704–711. DOI: 10.1063/1.1136655.

Mozer, F. S., Agapitov, O. V., Artemyev, A., Drake, J. F., Krasnoselskikh, V., Lejosne, S., and Vasko, I. (2015). "Time domain structures: What and where they are, what they do, and how they are made". In: *Geophys. Res. Lett.* **42** (10), pp. 3627–3638. DOI: 10.1002/2015gl063946.

Myers, C. E., Yamada, M., Ji, H., Yoo, J., Jara-Almonte, J., and Fox, W. (2016). "Laboratory study of low-β forces in arched, line-tied magnetic flux ropes". In: *Phys. Plasmas* **23** (11), p. 112102. DOI: 10.1063/1.4966691.

Nedzelskiy, I. S., Silva, C., Figueiredo, H., Fernandes, H., and Varandas, C. A. F. (2006). "Compact retarding field energy analyzer for the tokamak ISTTOK boundary plasma". In: *Rev. Sci. Instrum.* **77** (10), 10E729. DOI: 10.1063/1.2336463.

Øieroset, M., Phan, T. D., Eastwood, J. P., Fujimoto, M., Daughton, W., Shay, M. A., Angelopoulos, V., Mozer, F. S., McFadden, J. P., Larson, D. E., et al. (2011). "Direct Evidence for a Three-Dimensional Magnetic Flux Rope Flanked by Two Active Magnetic Reconnection X Lines at Earth's Magnetopause". In: *Phys. Rev. Lett.* **107** (16), p. 165007. DOI: 10.1103/physrevlett.107.165007.

Okazaki, K. and Andō, K. (1968). "Doppler Broadening of Helium Ion Lines in a Low Pressure Helium Arc". In: *Jpn. J. Appl. Phys.* **7** (8), p. 910. DOI: 10.1143/jjap.7.910.

Oksuz, L. and Hershkowitz, N. (2004). "Understanding Mach probes and Langmuir probes in a drifting, unmagnetized, non-uniform plasma". In: *Plasma Sources Sci. Technol.* **13** (2), p. 263. DOI: 10.1088/0963-0252/13/2/010.

Ono, Y., Yamada, M., Akao, T., Tajima, T., and Matsumoto, R. (1996). "Ion acceleration and direct ion heating in three-component magnetic reconnection". In: *Phys. Rev. Lett.* **76** (18), p. 3328. DOI: 10.2172/226405.

Parker, E. N. (1957). "Acceleration of Cosmic Rays in Solar Flares". In: *Phys. Rev.* **107** (3), p. 830. DOI: 10.1103/physrev.107.830.

— (1975). "X-ray bright spots on the Sun and the nonequilibrium of a twisted flux rope in a stratified atmosphere". In: *Astrophys. J.* **201**, pp. 494–501. DOI: 10.1086/153911.

Paschmann, G., Papamastorakis, I., Baumjohann, W., Sckopke, N., Carlson, C. W., Sonnerup, B. U. Ö, and Lühr, H. (1986). "The magnetopause for large magnetic shear: AMPTE/IRM observations". In: *J. Geophys. Res. Space Phys.* **91** (A10), pp. 11099–11115. DOI: 10.1029/ja091ia10p11099.

Patacchini, L. and Hutchinson, I. H. (2009). "Kinetic solution to the Mach probe problem in transversely flowing strongly magnetized plasmas". In: *Phys. Rev. E* **80** (3), p. 036403. DOI: 10.1103/physreve.80.036403.

Paz-Soldan, C., Brookhart, M. I., Clinch, A. J., Hannum, D. A., and Forest, C. B. (2011). "Two-dimensional axisymmetric and three-dimensional helical equilibrium in the line-tied screw pinch". In: *Phys. Plasmas* **18** (5), p. 052114. DOI: 10.1063/1.3592998.

Petschek, H. E. (1964). "50. Magnetic Field Annihilation". In: *AAS-NASA Symposium on the Physics of Solar Flares: Proceedings of a Symposium Held at the Goddard Space Flight Center, Greenbelt, Maryland, October 28-30, 1963*. Vol. 50. Scientific, Technical Information Division, National Aeronautics, and Space Administration, p. 425.

Pezzi, O., Pecora, F., Roux, J. le, Engelbrecht, N. E., Greco, A., Servidio, S., Malova, H. V., Khabarova, O. V., Malandraki, O., Bruno, R., et al. (2021). "Current Sheets, Plasmoids and Flux Ropes in the Heliosphere". In: *Space Sci. Rev.* **217** (3), pp. 1–70. DOI: 10.1007/s11214-021-00799-7.

Pfister, H. (1991). "Dynamics and Interaction of Plasma Currents with Large Self-Magnetic Fields and Their Relaxation Toward a Force-Free Configuration". PhD thesis.

Pitts, R. A. (1996). "Retarding field energy analysis for ion temperature measurement in the tokamak edge". In: *Contrib. Plasma Phys.* **36** (S1), pp. 87–93. DOI: 10.1002/ctpp.19960360114.

Pitts, R. A., Chavan, R., Davies, S. J., Erents, S. K., Kaveney, G., Matthews, G. F., Neill, G., Vince, J. E., JET-EFDA workprogramme contributors, and Duran, I. (2003). "Retarding field energy analyzer for the JET plasma boundary". In: *Rev. Sci. Instrum.* **74** (11), pp. 4644–4657. DOI: 10.1063/1.1619554.

Pontin, D. I. (2011). "Three-dimensional magnetic reconnection regimes: A review". In: *Adv. Space Res.* **47** (9), pp. 1508–1522. DOI: 10.1016/j.asr.2010.12.022.

Priest, E. R. and Démoulin, P. (1995). "Three-dimensional magnetic reconnection without null points: 1. Basic theory of magnetic flipping". In: *J. Geophys. Res. Space Phys.* **100** (A12), pp. 23443–23463. DOI: 10.1029/95ja02740.

Priest, E. R., Hornig, G., and Pontin, D. I. (2003). "On the nature of three-dimensional magnetic reconnection". In: *J. Geophys. Res. Space Phys.* **108** (A7). DOI: 10.1029/2002ja009812.

Priest, E. R., Parnell, C. E., and Martin, S. F. (1994). "A converging flux model of an X-ray bright point and an associated canceling magnetic feature". In: *Astrophys. J.* **427**, pp. 459–474. DOI: 10.1086/174157.

Priest, E. and Forbes, T. (2007). *Magnetic reconnection*. Cambridge New York: Cambridge University Press. ISBN: 0521481791.

Pritchett, P. L. and Coroniti, F. V. (2004). "Three-dimensional collisionless magnetic reconnection in the presence of a guide field". In: *J. Geophys. Res. Space Phys.* **109** (A1). DOI: 10.1029/2003ja009999.

Ricci, P., Brackbill, J. U., Daughton, W., and Lapenta, G. (2004). "Collisionless magnetic reconnection in the presence of a guide field". In: *Phys. Plasmas* **11** (8), pp. 4102–4114. DOI: 10.1063/1.1768552.

Robertson, C. A. and Fryer, J. G. (1969). "Some descriptive properties of normal mixtures". In: *Scand. Actuar. J.* **1969** (3-4), pp. 137–146. DOI: 10.1080/03461238.1969.10404590.

Russell, C. T., E. R. Priest, and L. C. Lee, eds. (1990). *Physics of Magnetic Flux Ropes*. American Geophysical Union. DOI: 10.1029/GM058.

Russell, C. T. and Elphic, R. C. (1979). "Observation of magnetic flux ropes in the Venus ionosphere". In: *Nature* **279** (5714), pp. 616–618. DOI: 10.1038/279616a0.

Ryutov, D. D., Drake, R. P., and Remington, B. A. (2000). "Criteria for Scaled Laboratory Simulations of Astrophysical MHD Phenomena". In: *Astrophys. J. Suppl. Ser.* **127** (2), p. 465. DOI: 10.1086/313320.

Ryutov, D. D., Furno, I., Intrator, T. P., Abbate, S., and Madziwa-Nussinov, T. (2006). "Phenomenological theory of the kink instability in a slender plasma column". In: *Phys. Plasmas* **13** (3), p. 032105. DOI: 10.1063/1.2180667.

Sakai, Y. and Katsumata, I. (1985). "An Energy Resolution Formula of a Three Plane Grids Retarding Field Energy Analyzer". In: *Jpn. J. Appl. Phys.* **24** (3R), p. 337. DOI: 10.1143/jjap.24.337.

Salewski, M., Geiger, B., Jacobsen, A. S., Abramovic, I., Korsholm, S. B., Leipold, F., Madsen, B., Madsen, J., McDermott, R. M., Moseev, D., et al. (2018). "Deuterium temperature, drift velocity, and density measurements in non-Maxwellian plasmas at ASDEX Upgrade". In: *Nucl. Fusion* **58** (3), p. 036017. DOI: 10.1088/1741-4326/aaa6e1.

Sarkango, Y., Slavin, J. A., Jia, X., DiBraccio, G. A., Gershman, D. J., Connerney, J. E. P., Kurth, W. S., and Hospodarsky, G. B. (2021). "Juno Observations of Ion-Inertial Scale Flux Ropes in the Jovian Magnetotail". In: *Geophys. Res. Lett.* **48** (2), e2020GL089721. DOI: 10.1029/2020gl089721.

Shafranov, V. D. (1956). "The stability of a cylindrical gaseous conductor in a magnetic field". In: *Sov. At. Energy* **1** (5), pp. 709–713. DOI: 10.1007/bf01480907.

Shikama, T., Kado, S., Okamoto, A., Kajita, S., and Tanaka, S. (2005). "Practical formula for Mach number probe diagnostics in weakly magnetized plasmas". In: *Phys. Plasmas* **12** (4), p. 044504. DOI: 10.1063/1.1872895.

Sibeck, D. G., Siscoe, G. L., Slavin, J. A., Smith, E. J., Bame, S. J., and Scarf, F. L. (1984). "Magnetotail flux ropes". In: *Geophys. Res. Lett.* **11** (10), pp. 1090–1093. DOI: 10.1029/gl011i010p01090.

Slavin, J. A., Lepping, R. P., Gjerloev, J., Fairfield, D. H., Hesse, M., Owen, C. J., Moldwin, M. B., Nagai, T., Ieda, A., and Mukai, T. (2003). "Geotail observations of magnetic flux ropes in the plasma sheet". In: *J. Geophys. Res. Space Phys.* **108** (A1), SMP–10. DOI: 10.1029/2002ja009557.

Slavin, J. A., Acuña, M. H., Anderson, B. J., Baker, D. N., Benna, M., Boardsen, S. A., Gloeckler, G., Gold, R. E., Ho, G. C., Korth, H., et al. (2009). "MESSENGER Observations of Magnetic Reconnection in Mercury's Magnetosphere". In: *Science* **324** (5927), pp. 606–610. DOI: 10.1126/science.1172011.

Slavin, J. A., Lepping, R. P., Wu, C.-C., Anderson, B. J., Baker, D. N., Benna, M., Boardsen, S. A., Killen, R. M., Korth, H., Krimigis, S. M., et al. (2010). "MESSENGER observations of large flux transfer events at Mercury". In: *Geophys. Res. Lett.* **37** (2). DOI: 10.1029/2009gl041485.

Spitzer, L. (1967). *Physics of Fully Ionized Gases*. Ed. by R. E. Marshak. 3. Interscience Publishers.

Spitzer Jr., L. and Härm, R. (1953). "Transport Phenomena in a Completely Ionized Gas". In: *Phys. Rev.* **89** (5), p. 977. DOI: 10.1103/physrev.89.977.

Stangeby, P. C. (1984). "Measuring plasma drift velocities in tokamak edge plasmas using probes". In: *Phys. Fluids* **27** (11), pp. 2699–2704. DOI: 10.1063/1.864573.

Stenzel, R. L., Gekelman, W., and Wild, N. (1982). "Magnetic field line reconnection experiments, 4. Resistivity, heating, and energy flow". In: *J. Geophys. Res. Space Phys.* **87** (A1), pp. 111–117. DOI: 10.1029/ja087ia01p00111.

Stenzel, R. L., Gekelman, W., Wild, N., Urrutia, J. M., and Whelan, D. (1983). "Directional velocity analyzer for measuring electron distribution functions in plasmas". In: *Rev. Sci. Instrum.* **54** (10), pp. 1302–1310. DOI: 10.1063/1.1137263.

Stenzel, R. L. and Urrutia, J. M. (2000). "Electron magnetohydrodynamic turbulence in a high-beta plasma. III. Conditionally averaged multipoint fluctuation measurements". In: *Phys. Plasmas* **7** (11), pp. 4466–4476. DOI: 10.1063/1.1314345.

Sun, X., Intrator, T. P., Dorf, L., Sears, J., Furno, I., and Lapenta, G. (2010). "Flux Rope Dynamics: Experimental Study of Bouncing and Merging". In: *Phys. Rev. Lett.* **105** (25), p. 255001. DOI: 10.1103/physrevlett.105.255001.

Sweet, P. A. (1958). "14. The neutral point theory of solar flares". In: *Symposium-International Astronomical Union*. Vol. 6. Cambridge University Press, pp. 123–134. DOI: 10.1017/s0074180900237704.

Taylor, J. B. (1974). "Relaxation of Toroidal Plasma and Generation of Reverse Magnetic Fields". In: *Phys. Rev. Lett.* **33** (19), p. 1139. DOI: 10.1103/physrevlett.33.1139.

Teliban, I., Block, D., Piel, A., and Greiner, F. (2007). "Improved conditional averaging technique for plasma fluctuation diagnostics". In: *Plasma Phys. Control. Fusion* **49** (4), p. 485. DOI: 10.1088/0741-3335/49/4/011.

Treumann, R. A. and Baumjohann, W. (2013). "Collisionless magnetic reconnection in space plasmas". In: *Front. Phys.* **1**, p. 31. DOI: 10.3389/fphy.2013.00031.

Tripathi, S. K. P. and Gekelman, W. (2010). "Laboratory Simulation of Arched Magnetic Flux Rope Eruptions in the Solar Atmosphere". In: *Phys. Rev. Lett.* **105** (7), p. 075005. DOI: 10.1103/physrevlett.105.075005.

Tripathi, S. K. P. and Gekelman, W. (2013). "Dynamics of an Erupting Arched Magnetic Flux Rope in a Laboratory Plasma Experiment". In: *Sol. Phys.* **286** (2), pp. 479–492. DOI: 10.1007/s11207-013-0257-0.

Ugai, M. (1984). "Self-consistent development of fast magnetic reconnection with anomalous plasma resistivity". In: *Plasma Phys. Control. Fusion* **26** (12B), p. 1549. DOI: 10.1088/0741-3335/26/12b/010.

Umstattd, R. J., Carr, C. G., Frenzen, C. L., Luginsland, J. W., and Lau, Y. Y. (2005). "A simple physical derivation of Child–Langmuir space-charge-limited emission using vacuum capacitance". In: *Am. J. Phys* **73** (2), pp. 160–163. DOI: 10.1119/1.1781664.

Valsaque, F., Manfredi, G., Gunn, J. P., and Gauthier, E. (2002). "Kinetic simulations of ion temperature measurements from retarding field analyzers". In: *Phys. Plasmas* **9** (5), pp. 1806–1814. DOI: 10.1063/1.1463416.

Van Compernolle, B. and Gekelman, W. (2012). "Morphology and dynamics of three interacting kink-unstable flux ropes in a laboratory magnetoplasma". In: *Phys. Plasmas* **19** (10), p. 102102. DOI: 10.1063/1.4755949.

Van De Ven, T. H. M., De Meijere, C. A., Van Der Horst, R. M., Van Kampen, M., Banine, V. Y., and Beckers, J. (2018). "Analysis of retarding field energy analyzer transmission by simulation of ion trajectories". In: *Rev. Sci. Instrum.* **89** (4), p. 043501. DOI: 10.1063/1.5018269.

Vignes, D, Acuña, M. H., Connerney, J. E. P., Crider, D. H., Rème, H., and Mazelle, C. (2004). "Magnetic Flux Ropes in the Martian Atmosphere: Global Characteristics". In: *Space Science Reviews* **111**, pp. 223–231. DOI: 10.1023/b:spac.0000032716.21619.f2.

Wang, Y., Shen, C., Liu, R., Liu, J., Guo, J., Li, X., Xu, M., Hu, Q., and Zhang, T. (2018). "Understanding the Twist Distribution Inside Magnetic Flux Ropes by Anatomizing an Interplanetary Magnetic Cloud". In: *J. Geophys. Res. Space Phys.* **123** (5), pp. 3238–3261. DOI: 10.1002/2017ja024971.

Williamson, D. L. and Rasch, P. J. (1989). "Two-dimensional semi-Lagrangian transport with shape-preserving interpolation". In: *Mon. Wea. Rev.* **117** (1), pp. 102–129. DOI: 10.1175/1520-0493(1989)117<0102:TDSLTW>2.0.CO;2.

Yamada, M., Ji, H., Hsu, S., Carter, T., Kulsrud, R., Bretz, N., Jobes, F., Ono, Y., and Perkins, F. (1997). "Study of driven magnetic reconnection in a laboratory plasma". In: *Phys. Plasmas* **4** (5), pp. 1936–1944. DOI: 10.1063/1.872336.

Yamada, M., Kulsrud, R., and Ji, H. (2010). "Magnetic reconnection". In: *Rev. Mod. Phys.* **82** (1), p. 603. DOI: 10.1103/revmodphys.82.603.

Yamada, M., Yoo, J., Jara-Almonte, J., Ji, H., Kulsrud, R. M., and Myers, C. E. (2014). "Conversion of magnetic energy in the magnetic reconnection layer of a laboratory plasma". In: *Nat. Commun.* **5** (1), pp. 1–8. DOI: 10.1038/ncomms5774.

Zhu, Z. and Winglee, R. M. (1996). "Tearing instability, flux ropes, and the kinetic current sheet kink instability in the Earth's magnetotail: A three-dimensional perspective from particle simulations". In: *J. Geophys. Res. Space Phys.* **101** (A3), pp. 4885–4897. DOI: 10.1029/95ja03144.

Zweibel, E. G. and Yamada, M. (2009). "Magnetic Reconnection in Astrophysical and Laboratory Plasmas". In: *Annu. Rev. Astron. Astrophys.* **47**, pp. 291–332. DOI: 10.1146/annurev-astro-082708-101726.